RICE UNIVERSITY

Optical biopsy systems using ultra-slim objectives for the diagnosis of breast cancer
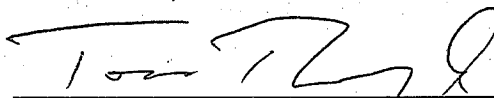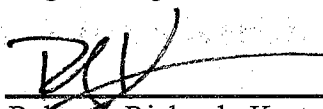
by

Matthew Ryan Kyrish

A THESIS SUBMITTED
IN PARTIAL FULFILLMENT OF THE
REQUIREMENTS FOR THE DEGREE
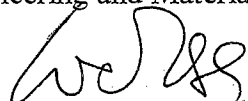
Doctor of Philosophy

APPROVED, THESIS COMMITTEE

Tomasz S. Tkaczyk, Chair, Assistant Professor
Bioengineering, Electrical and Computer
Engineering

Rebecca Richards-Kortum, Stanley C. Moore
Professor Bioengineering

Andrew J. Dick, Assistant Professor Mechanical
Engineering and Materials Science

Wei Yang, Professor Diagnostic Radiology,
Division of Diagnostic Imaging, The University of
Texas MD Anderson Cancer Center

HOUSTON, TEXAS
April 2013

ABSTRACT

Optical biopsy systems using ultra-slim objectives for the diagnosis of breast cancer

by

Matthew Ryan Kyrish

One in eight women in America will develop breast cancer at some point in their lives. Breast cancer is the second deadliest form of cancer for women in the United States. When a suspicious region of the breast is detected, the tissue is diagnosed by removing a sample, preparing an H&E section, and performing histopathology. This procedure is expensive, invasive, and can take days to return a diagnosis. An alternative to excision biopsies is to instead perform an optical biopsy. This work details endomicroscopes intended to perform optical biopsies in breast tissue. The work address two issues limiting current optical biopsy systems: insufficient resolution and inability to reject out of focus light. To improve the resolution of current endomicroscopes, ultra-slim objectives are developed using optical plastics and zero alignment fabrication techniques. These objectives can outperform current alternative endomicroscope objectives in terms of performance across the field of view and chromatic aberration correction, while remaining as narrow as a biopsy needle. Next, an endomicroscope which utilizes structured illumination to perform optical section is designed, tested, and evaluated on *ex vivo* breast biopsies. The new endomicroscope provides high contrast images by reducing out of focus background light. Finally, an achromatic, ultra-slim objective

and the structured illumination endomicroscope are integrated to form an optical biopsy system with improved lateral resolution and axial response. This integrated system is a step forward for *in vivo* microscopy and cancer diagnoses.

Acknowledgments

I would like to begin by thanking my advisor, Dr. Tomasz Tkaczyk, for his support and mentorship during my time at Rice. His dedication to research and his ingenuity in the field of optics have been a constant inspiration to me.

I would also like to thank my other committee members, Dr. Rebecca Richards-Kortum, Dr. Andrew Dick, and Dr. Wei Yang, for their advice and encouragement over the years. I am grateful to have such a talented committee.

During my graduate education, I have been incredibly fortunate to work with members and alumni of the Tkaczyk and Kortum labs, particularly Dr. Noah Bedard, Dr. Brian McCall, Jessica Dobbs, Dr. Robert Kester, Dr. Liang Gao, Dr. Michal Pawlowski, Dr. Nathan Hagan, Thuc-Uyen Nguyen, Adam Shadfan, Alessandra Forcucci, Jason Dwight, Anne Hellebust, Tim Quang, Jennifer Burnett, Gabriel Ochoa, and Vivian Mack. My thanks go to Dwight Dear for his help in the machine shop and to Dr. Jan Hewitt for her help improving my writing. I'd also like to thank my friends and colleagues, both those within the Rice community and throughout the world, for their camaraderie and guidance.

Finally, I want to especially thank my family for their unwavering love and support. My father, Michael, inspired me to be an engineer. My mother, Kathy, has been a constant source of encouragement. My sisters, Angela and Kristin, always know just what to say. I could not have done it without you.

Contents

List of Figures

List of Tables

List of Equations

Nomenclature

DXRLE	Direct x-ray lithography and electroplating
FOV	Field of view
GDD	Group delay dispersion
GRIN	Gradient index
GVD	Group velocity dispersion
HRME	High resolution microendoscope
LCTF	Liquid crystal tunable filter
MTF	Modulation transfer function
NA	Numerical aperture
NOA	Norland optical adhesive
OD	Outer diameter
PBS	Phosphate buffered saline
PC	Polycarbonate
PMMA	Poly(methyl methacrylate)
PMT	Photomultiplier tube
PSF	Point spread function
PS	Polystyrene
SHG	Second harmonic generation
SI-HRME	Structured illumination HRME
SPDT	Single point diamond turning
SR	Strehl ratio

TPM   Two photon microscopy

TPE   Two photon excitation

Chapter 1

Introduction

1.1. Objective and Specific Aims

The goal of this research is to develop ultra-slim endomicroscope objectives which can be integrated into optical biopsy systems intended to aid in the diagnosis of cancer. The custom objectives provide the integrated systems with higher resolution compared to previous generations of endomicroscopes, allowing smaller cellular features to be resolved. The new endomicroscopes also utilizes optical sectioning to create thin sections of tissue and reject background light, allowing the devices to be used in breast tissue. These developments allow for images which are closer to histopathology, the gold standard for cancer diagnostics.

The specific aims are:

Specific Aim 1: Design and fabricate endomicroscope objectives, including an achromatized objective, evaluate their performance using quantitative and qualitative analyses, and test the objectives on biological samples.

Specific Aim 2: Build and characterize an endomicroscope which can perform optical sectioning to improve the contrast of images of thick breast tissue.

Specific Aim 3: Integrate a custom objective into the endomicroscope and assess the improvement of the system's lateral resolution and axial response.

The motivation for this work is to develop a system which can perform diagnostically relevant optical biopsies, thereby reducing the number of invasive, time consuming, and expensive excisional biopsies performed.

1.2. Overview

This dissertation describes the development of (1) ultra-slim endomicroscope objectives (Chapter 3 and Chapter 4), (2) a fiber bundle endomicroscope with optical sectioning (Chapter 5), and (3) an optical biopsy system which integrates the custom objective to the endomicroscope (Chapter 6). In more detail, the dissertation is organized as follows:

Chapter 1 provides an overview of the work discussed in this thesis and lists the specific aims.

Chapter 2 begins with an overview of breast cancer and discusses current techniques for its diagnosis. It then summarizes current technologies for imaging breast cancer and compares this with the proposed optical biopsy system.

Chapter 3 covers the design, fabrication, and testing of the first generation of ultra-slim NA0.4 objectives. The custom objective is composed of plastic lenses, utilizes a zero alignment fabrication technique, and is contained within a hypodermic steel tube with a 1.27 mm outer diameter. The objective's performance is evaluated with standard quantitative measurements and in biological samples using two-photon fluorescence and second harmonic generation microscopy.

Chapter 4 discusses the design and validation of achromatic endomicroscope objectives. To prove the concept, the lens design is built by fabricating 0.9 mm clear aperture lenses in 22 mm plastic disks. This chapter presents the design performing well across a broad wavelength range. In addition, high contrast, optically sectioned images via structured illumination are shown.

Chapter 5 describes a fiber bundle fluorescence endomicroscope with optical sectioning via structured illumination. It is shown that optical sectioning significantly improves the contrast of images of breast tissue compared to a wide-field fluorescence endomicroscope. Compared to wide-field images, optically sectioned images provide results closer to a commercial confocal microscope and histology sections.

Chapter 6 presents a fully integrated optical needle biopsy system. The endomicroscope projects structured illumination onto the sample through an

achromatic objective which has been attached to the distal tip of a coherent fiber bundle. The system's performance is characterized and its optical sectioning capability is demonstrated.

Chapter 7 summarizes the work, discusses its impact, and explores avenues for future work.

Chapter 2

Background

2.1. Motivation and significance

Cancer is the second leading cause of death in the United States. For American women, breast cancer is the second leading cause of death from cancer [1]. Early detection and diagnosis is crucial to improving prognosis and decreasing treatment-associated morbidity. In order to diagnose breast cancer, one must understand how breast cancer forms and how cancerous cells and tissue differ from their healthy counterparts. This chapter explains the morphological changes breast cells undergo as they become cancerous and describes the standard pathological diagnosis. *In vivo* imaging techniques currently available for cancer diagnosis other than optical biopsy are discussed. This leads to the justification for the endomicroscope objectives and optical biopsy systems described in this dissertation.

2.2. The development and diagnosis of breast cancer

Invasive breast cancer generally develops via ductal carcinoma *in situ* [2], which occurs in the tubes (ducts) which allow milk to flow from the milk-producing lobules to the nipple. Figure 1 illustrates the progression of cancer via ductal carcinoma *in situ*. Normal tissue has well-defined boundaries between epithelial cells (red), basal cells (green), and the basement membrane (thick black line). During the transition to ductal carcinoma *in situ*, the epithelial cells undergo hyperplasia and experience a loss of organization. As the cells become invasive cancer, the epithelial cells completely overgrow the boundary of normal tissue, crowding out the basal cells and expanding beyond the basement membrane. Once the breast cancer cells leave their original location and invade distal organs, the cancer is termed metastatic.
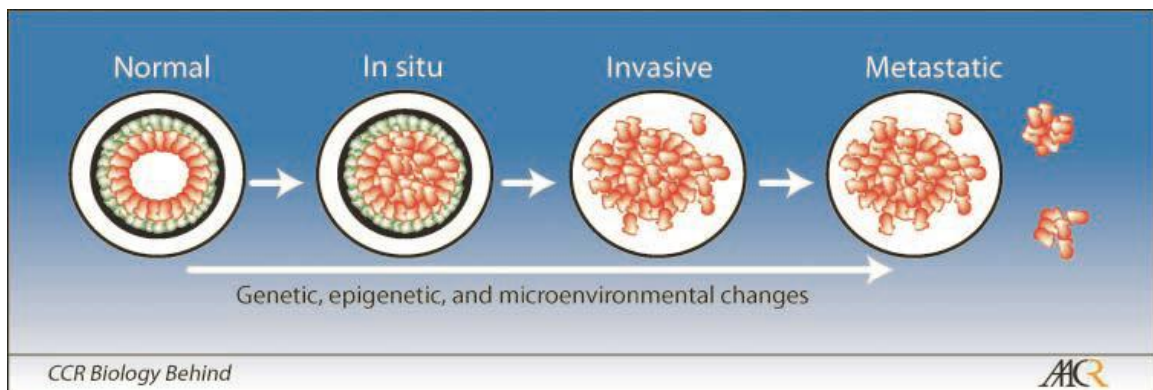
Figure 2.1. Progress of breast tissue from healthy to metastatic cancer following the ductal carcinoma *in situ* pathway. At each stage, the cells appear morphologically different from cells in the other stages, allowing identification via anatomic pathology. Epithelial cells are red, myoepithelial or basal cells are green, the basement membrane is represented by the thick black line, the breast boundary is represented by the thin black line. From Polyak [3].

Lobular carcinoma *in situ*, which begins in the milk-forming lobules, is not an actual breast carcinoma, despite the name [4]. However, it is an indicator for an increased risk of invasive breast cancer in the future. In either case, the cells experience morphological changes; they become poorly differentiated, disorganized, and begin to rapidly divide.

If not detected and treated early, cancer cells will multiply to the point that the diseased tissue can be detected macroscopically. When an abnormality is found in breast tissue during a routine examination like manual palpation or screening mammography, the region must be classified as benign or malignant. For nearly 100% of such abnormalities, the diagnosis is performed via one of three types of biopsies: open biopsy, core needle biopsy, or fine needle aspiration biopsy (FNAB) [5,6]. The outer diameter (OD) of hypodermic needles used to perform biopsies range in size from 0.64 mm outer (23-gage) for the narrowest FNAB needles to 2.11 mm (14-gage) for the widest core biopsy needles [7].

Approximately 1.6 million breast biopsies are performed each year in the US alone [8]. In every case, cells or tissue must be extracted so that a histopathological analysis can be completed. The cells are stained, typically with hematoxylin and eosin (H&E stain), fixed to a microscope slide, and examined beneath a microscope. Cellular organization and nuclear size and shape are used to identify benign tissue, carcinoma *in situ*, invasive cancer, and other types of tissue, including inflammation and atypical hyperplasia [9,10].

Pathologists assign a histologic grade to the tissue extracted via biopsy, which quantifies how different cancer cells look from normal cells (Figure 2.2); a higher grade corresponds to more difference from regular tissue. Pathologists look for abnormal nuclei, which are enlarged and take up a greater fraction of the cytoplasm than normal nuclei. They also look at the cellular organization to determine histologic grade. Normal tissue is highly organized while higher grades of cancer are increasingly disordered. Examining suspicious tissue *in vivo* would allow a diagnosis to be made immediately without causing morbidity associated with tissue biopsy, and would allow a comparison to be made to surrounding normal tissue. Because as many as 75% of breast biopsies return a diagnosis of benign [5], it would ease the patient's state of mind if the results of their diagnosis were returned before they even left the hospital, rather than waiting days or even weeks. Alternatively, if the diagnosis is positive, it would be possible for treatment planning to begin immediately.
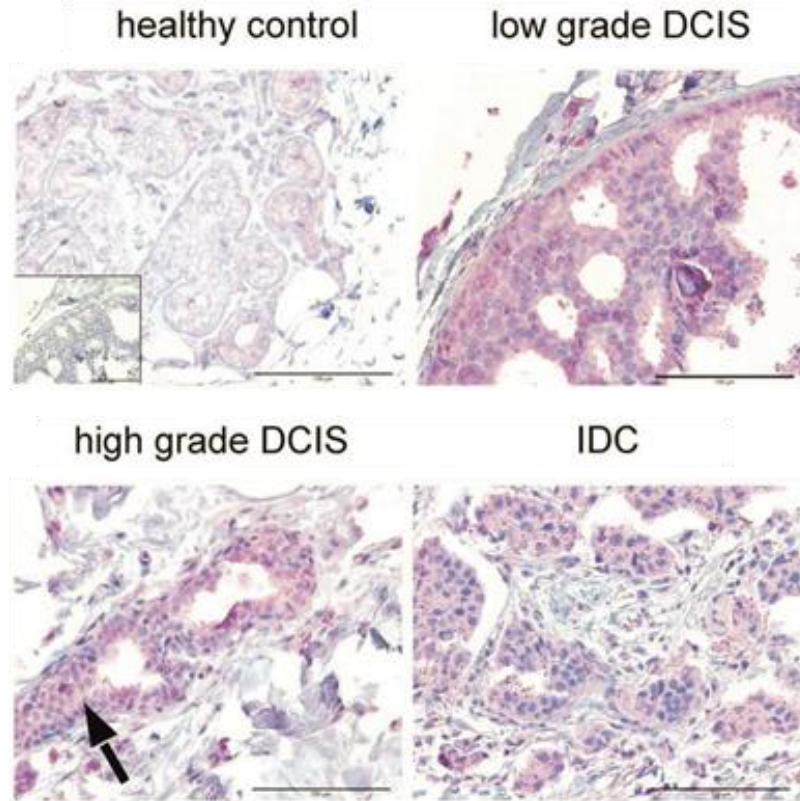
Figure 2.2. Histology of breast tissue ranging from healthy cells through invasive carcinoma. The cells have undergone H&E staining, as well as an immunohistochemical stain. Scale bar is 100 μm. Images from Kretschmer et al. [11].

Using multiple fluorescent dyes to target different subcellular features, such as the nuclei and cytoplasm, can allow *in vivo* images to be captured which are similar to H&E staining. The method has already been demonstrated for benchtop confocal systems which combines fluorescence and reflectance images and performs "digital staining" to create images which closely mimic histology [12,13] (Figure 2.3). Göbel et al. also presented an optical biopsy system utilizing a fiber bundle without a distal objective which is capable of capturing *in vivo* fluorescence images of endogenous and exogenous sources [14]. This method can make the optical biopsy images similar to what is seen on a traditional histology microscope slide.
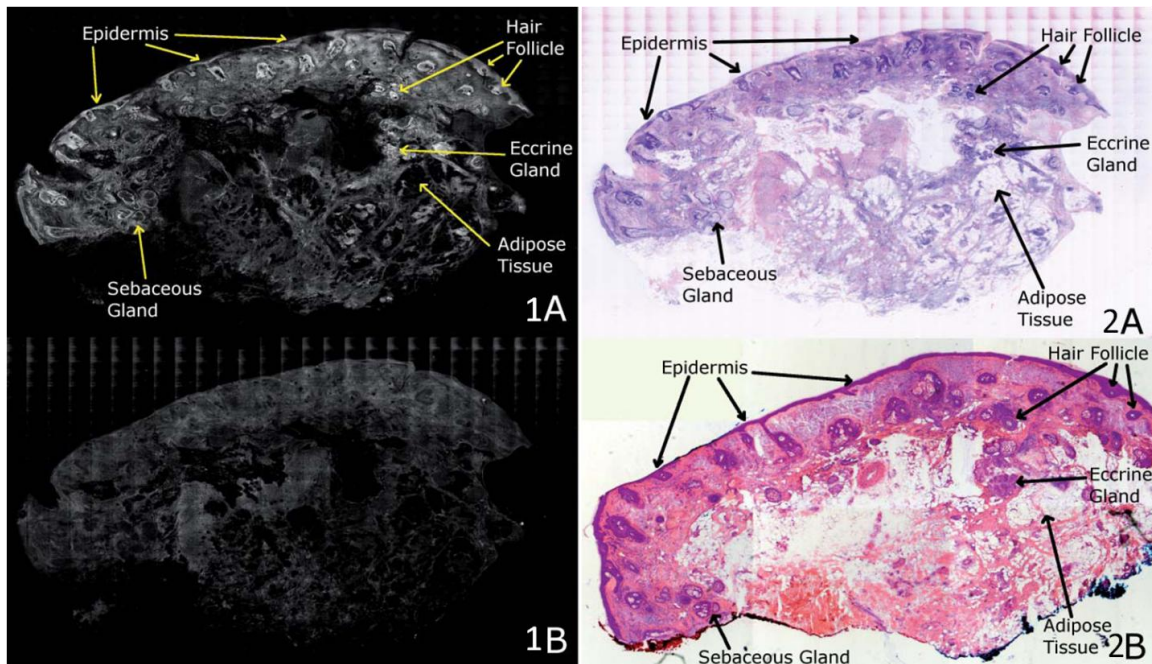
Figure 2.3. Mohs surgical excision of normal skin after mosaic imaging. (1A) Confocal fluorescence. (1B) Confocal reflectance. (2A) Pseudocolor image created by performing a digital stain of the confocal images and then overlaying them. (2B) Conventional histology. From Bini et al. [12].

Using two fluorescent dyes to create a pseudocolor image will provide color images which are more similar to H&E section images than the monochrome images of most current high-resolution imaging systems. Two dyes which can be used to perform digital staining are proflavine and cresyl violet. Proflavine inherently stains the nucleus, like hematoxylin, while cresyl violet is much more likely to be found in the cytoplasm, like eosin, though it also moves to the nucleoli. Figure 2.4 shows three images of the same set of breast carcinoma cells from the 435S cell line which have been seeded on a microscope slide and imaged with a custom achromatic objective described in Chapter 6. The cells were stained with proflavine and cresyl violet, which were imaged separately by exciting with a GFP filter set and a Texas Red filter set, respectively (Figure 2.4(a) and Figure 2.4(b)). Figure 2.4(c) is a

pseudocolor image created by combining the proflavine and cresyl violet images using an algorithm developed by Bini et al. [12]. The digitally stained image much more closely mimics histopathology images (like those in Figure 2.2) than either single dye image.
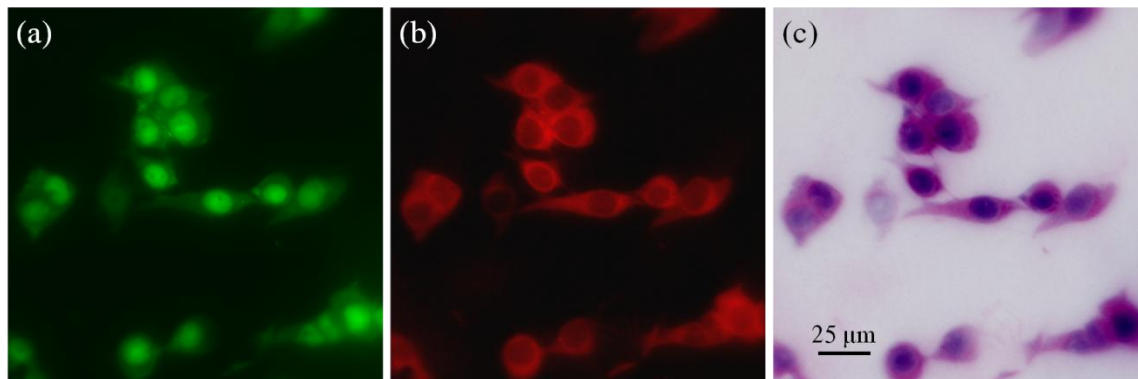
Figure 2.4. Breast carcinoma cells from the 435S line stained with (a) proflavine and (b) cresyl violet. Note that the proflavine stays mostly in the nucleus while the cresyl violet is largely confined to the cytoplasm. (c) A pseudocolor image which mimics H&E staining obtained by combining the images in (a) and (b) using an algorithm developed by Bini et al. [12]. The images were captured with a custom, achromatic objective described in Chapter 6.

2.3. Current *in vivo* techniques for imaging breast cancer

There are two types of *in vivo* imaging: breast imaging, which allows all or most of the breast to be seen simultaneously at low resolution, and microscopic imaging, which allows subcellular resolution for a small field of view (FOV). The most common breast imaging techniques and their spatial resolutions are listed in Table 2.1 (compiled from [15–19]). Although such techniques do not have the ability to resolve cellular or sub-cellular features, they allow large regions of tissue or even

entire organs to be measured at once, allowing suspicious regions to be imaged on a macroscopic scale. They can also penetrate through the entire breast.

Table 2.1 Breast imaging modalities

Technique	Resolution Limit
Positron Emission Tomography (PET)	2 mm
Magnetic Resonance Imaging (MRI)	0.1 mm
X-ray mammography	0.08 to 0.14 mm
Ultrasound imaging	1 mm
Diffuse imaging	6 mm

Small FOV, high resolution microscopic imaging techniques generally use endomicroscopes to capture images via single-photon fluorescence [20,21], reflectance or fluorescence confocal microscopy [22,23], two-photon fluorescence [23–25], structured illumination [26], or optical coherence tomography (OCT) [27]. Examples of single- and two-photon fluorescence in *ex vivo* breast tissue via endomicroscopy are shown in Figure 2.5.

By utilizing an objective that is the size of a biopsy needle, the optical biopsy system can pierce the skin, be guided to the suspicious lesion, and then image the tissue. Other imaging systems are generally too large to safely pierce tissue and instead must be placed no closer than the surface of the organ. The *in vivo* imaging depth is thus limited by scattering and out of focus light. The maximum depths of *in vivo* imaging for various modalities are listed in Table 2.2 (compiled from [22,23,28]. However, it is important to note that these are approximate values which vary based

on the specific tissue. Nonetheless, the microscopic imaging techniques are unable

to reach the vast majority of abnormal breast lesions without piercing the tissue like

a conventional biopsy.
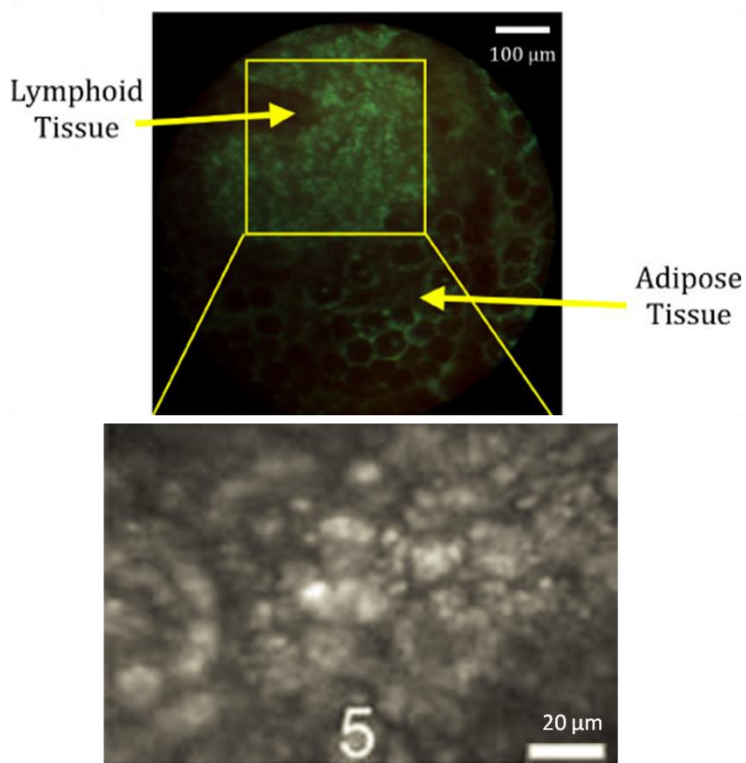
Figure 2.5. Breast tissue imaged via endomicroscopy. The top image, from Rosbach et al. [21], shows lymphoid and adipose tissues from a surgically removed lymph node imaged with via fluorescence through a coherent fiber bundle. The bottom image, from Fu et al. [24], is human u-87 MG glioblastoma tissue (from a breast cancer cell line) which has been xenografted to a mouse, then removed and imaged via two-photon fluorescence with an endomicroscope.

Table 2.2. Maximum depth of *in vivo* microscopic imaging

Technique	Maximum Depth
Single Photon Epifluorescence	50 μm
Two-Photon Fluorescence	300 μm
Reflectance Confocal	500 μm
Fluorescence Confocal	50 μm
Optical Coherence Tomography (OCT)	3 mm
Structured Illumination	**100 μm**

Structured illumination is somewhat different from the other modalities, its maximum depth being limited by the depth at which the grid pattern can be resolved; larger grid periods lead to deeper penetration. In one study, fluorescent rods approximately 1 mm in size have been successfully resolved 4 mm beneath a thick tissue phantom [29], while in another, the image contrast was reduced such that signal to background ratio was approaching 1 after fewer than 60 μm [30]. For microscopic imaging via structured illumination, a maximum imaging depth between 50 and 100 μm is generally assumed.

When there is a palpable mass in the breast which needs to be diagnosed, the standard of care is often still to perform a biopsy guided only by touch [7]. For nonpalpable lesions, stereotactic (or mammography-guided) biopsy and especially ultrasound-guided biopsy are used to direct the biopsy needle to the region of interest. However, stereotactic and ultrasound guided biopsies are increasingly being used to guide biopsy needles to the suspicious region even for palpable masses [31], which enhances the surgeons ability to guide the needle and allows an image to be made of the placement of the biopsy needle relative to the region of interest (Figure 2.6). While ultrasound is generally the preferred method for biopsy

localization, as it is safe, simple, and fast, mammography or even MRI are used when the lesion cannot be visualized with ultrasound.
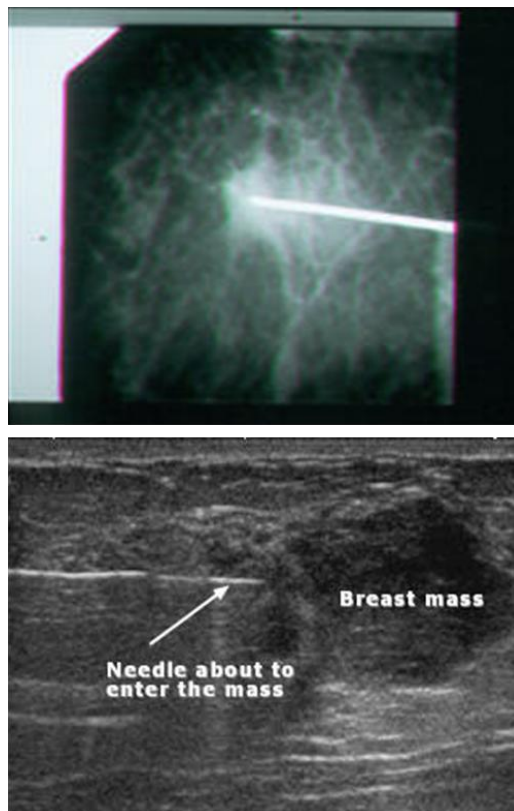
Figure 2.6. Guided breast biopsies. The top image shows a stereotactic biopsy [32], where the bright rod is the needle and the white mass is the suspicious region. The bottom image shows an ultrasound-guided biopsy [33].

In vivo fluorescent imaging has already been accomplished using organic dyes, such as acriflavine, acridine orange, and fluorescein, in conjunction with confocal endoscopy [34–36]. Certain dyes, including fluorescein, can be administered intravenously and will rapidly migrate to the extracellular matrix of epithelial cells and the lamina propria layer [34]. In addition, it may be possible to inject dye directly to the region of interest using a separate needle which is also guided by mammography or ultrasound imaging.

2.4. Comparison of existing technologies for optical biopsy systems

Endomicroscopes currently available are often constructed with gradient index (GRIN) lenses, which typically have an outer diameter of approximately 1 mm [37–41]; this makes GRIN lenses as small as or smaller than most biopsy needles, which range in size from 0.64 to 2.11 mm OD (Section 2.2). GRIN lenses are glass cylinders which have a quadratically varying index of refraction along their radius. This change in index through the material causes the cylinders to bend light, performing the same function as the curved surfaces of a conventional lens (Figure 2.7). When combined with a refractive glass lens, GRIN lenses can form objectives with limited aberration correction [42]. However, this aberration correction is monochromatic, so chromatic aberration can still cause a loss of performance [38,39,43,44]. Also, even combination GRIN lens/ refractive lens objectives intended for endoscopic imaging suffer significant performance degradation across the FOV. For instance, GRINTECH's [42] high numerical aperture (NA) endomicroscopic imaging objectives have a nominal NA0.8 for monochromatic light. However, at the edge of a 100 μm FOV, the diffraction-limited NA is only 0.4, and it continues to drop as the FOV increases.
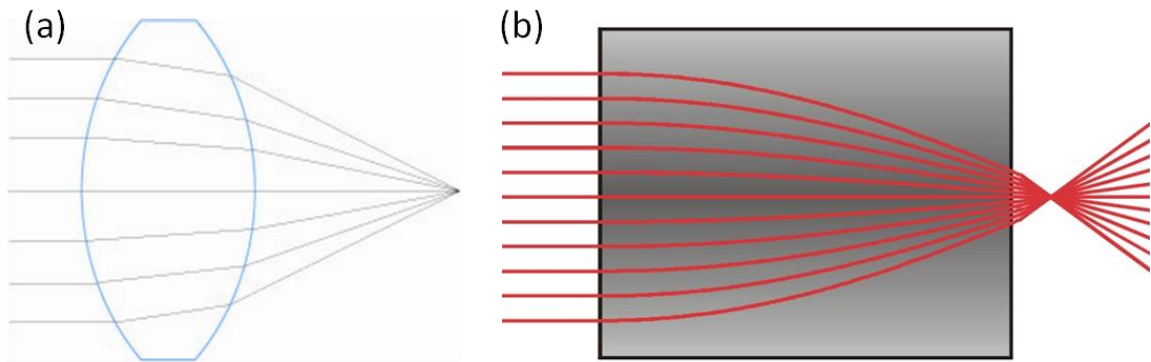
Figure 2.7. (a) Conventional lens, with a constant index of refraction. (b) GRIN lens, with an index of refraction which varies quadratically across the radius. From GRINTECH [42].

Chromatic aberration, due to dispersion through the GRIN lenses, makes it impossible to match the focal planes of excitation light and emission light and to image multiple wavelengths without aberration correction elsewhere in the imaging system. Multiple dyes cannot be used simultaneously with a GRIN objective because chromatic aberration causes them to have different focal planes, meaning at least one will be out of focus. Using a custom achromatized objective allows chromatic aberration to be corrected, can provide constant performance across the FOV, and allows multiple dyes to be used, permitting psuedocoloring via digital staining.

An alternative to GRIN lenses which maintains a probe tip narrow enough for optical biopsy is to use a coherent fiber bundle (also called an image guide) without any distal optics. A fiber bundle fluorescence endomicroscope (described in the literature as the high-resolution microendoscope or HRME) has successfully imaged subcellular features and tissue organization in the oral cavity using a probe approximately 1 mm wide [20,45,46]. The narrow OD of the fiber bundle means the HRME is narrow enough to perform an optical biopsy.

After staining the tissue with proflavine, a fluorescent dye, the HRME displays the nuclei in the oral cavity as bright ovals. However, although the nuclei can be seen with the HRME, they cannot be sufficiently resolved, particularly in breast tissue. The nuclear diameter is approximately 5-10 μm, while the current resolution of the HRME is 8 μm, due to the fibers' core-to-core spacing of 4 μm. Landau et al. [47] added a 3.2X objective to the tip of the same coherent fiber bundle, providing a resolution of 2.5 μm. A system with higher resolution would improve clinicians' ability to indentify cellular atypia, the absence of a myoepithelial cell layer, and invasion of cancer cells into normal tissue, all of which indicate malignancy [48]. Pathologists usually begin examining tissue with low magnification microscope objectives (between 4X and 10X) with corresponding low NA (NA0.1 to NA0.15, typically). This provides 2 to 3 μm resolution, a range which the objective added to the fiber bundle is able to match.

Other miniature objectives utilizing conventional refractive lenses have also been designed and tested [27,35,49–54]. In all cases, the OD of the objective was significantly larger than the OD of even the largest core biopsy needle (their diameters were between 2.6 mm and 7 mm) or the objective was designed for a single wavelength. Although others have recognized the advantages offered by plastic lenses and proposed achromatized systems [55,56], no one has yet constructed such devices, to the best of our knowledge. An optical biopsy objective should be achromatic and provide an improvement in resolution, while remaining no wider than 2.1 mm, the OD of a core biopsy needle.

The HRME also suffers from high levels of background light in thick, dense tissue like the breast. To improve contrast by reducing out of focus light, the optical biopsy system uses structured illumination to obtain optically sectioned images [57,58]. Structured illumination is performed by projecting a rectangular grid pattern of known frequency onto the sample and translating the pattern laterally in discrete steps. Each step is 1/3 of the period of the grid. Typically, three shifted images are recombined using Equation 2.1

$$I = \sqrt{(I_1 - I_2)^2 + (I_1 - I_3)^2 + (I_2 - I_3)^2}$$,

Equation 2.1. Structured illumination image creation

where I represents the intensity of the final image and I_x is one of the precursor images which are shifted from each other by a phase of 0, $2\pi/3$, and $4\pi/3$ [57]. Figure 2.8 provides two examples of structured illumination.

Structured illumination is a simple alternative to confocal microscopy to perform optical sectioning [26,59]; it can provide optical sectioning which is equivalent to that of a confocal system [58]. Structured illumination also has a higher frame rate [60], which is an important factor for *in vivo* imaging. Using optical sectioning, it is possible to image a thin slice of thick tissue, such as the breast, which provides an image closer to what pathologists are familiar with. Others have already demonstrated the ability to perform structured illumination with an endomicroscope [26,61]. However, once again the ability to perform an optical biopsy with those systems is limited either by the resolution of the system or the width of the probe tip. Utilizing structured illumination with a custom, ultra-slim

objective will allow optical sectioning to be performed as part of an optical biopsy

for the detection of breast cancer.
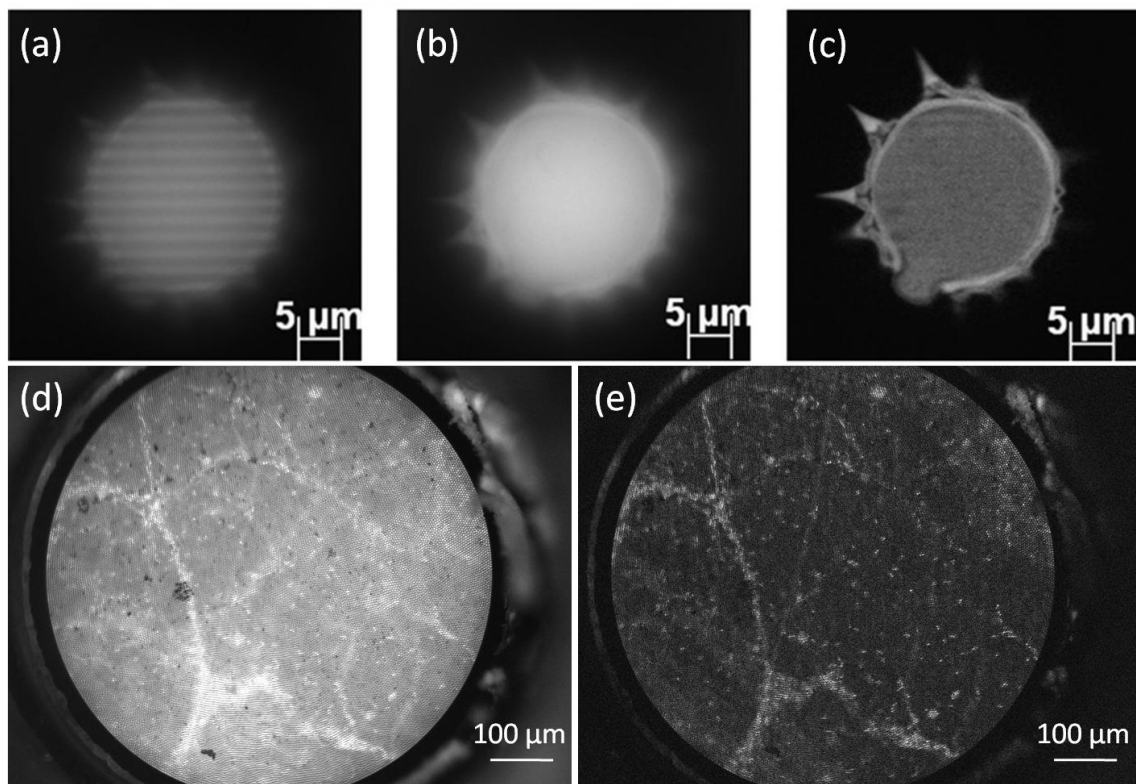
Figure 2.8. (a-c) Imaging a grain of pollen via structured illumination on a benchtop microscope, from Karadaglic and Wilson [58]. The raw image (a) shows the modulated grid pattern, while image (b) illustrates what the sample looks like via conventional fluorescence. Image (c) is the smaple optically sectioned via structured illumination. The images in (d) and (e) are images of porcine oral tissue stained with proflavine captured through an endomicroscope with a bare fiber bundle. Image (d) is without structured illumination and image (e) is with structured illumination.

<div align="right">

Chapter 3

</div>

Ultra-slim plastic endomicroscope objective for optical biopsy systems

*The contents of this chapter were published in the following journal article: M. Kyrish, U. Utzinger, M. Descour, B. Baggett, and T. Tkaczyk, "Ultra-slim plastic endomicroscope objective for non-linear microscopy," Opt. Express 19, 7603-7615 (2011).

As discussed in Section 2.4, endomicroscopes which utilize fiber bundles can use objectives at their distal tip to improve their lateral resolution. For these systems to be used to perform an optical biopsy, the objective must be no wider than a biopsy needle. While developing sufficiently narrow endomicroscope objectives, a number of ultra-slim objectives using plastic as the optical material were designed and built for different spectral ranges and working distances. One implementation was a multiphoton design for 800 nm excitation light and with a 200 μm working distance. This implementation is presented below.

The selection of optical materials for the objective was carefully analyzed using several criteria including optical transmission, autofluorescence, injection molding induced birefringence, and pulse broadening due to group velocity dispersion. The resulting system is an NA0.4 all-plastic, refractive endomicroscope objective with FOV = 250 μm, 1.27 mm OD, and 0.8 mm clear aperture with diffraction limited performance. Examples of second-harmonic generation (illumination at 780 nm) in collagen fibers and two-photon excited fluorescence (illumination at 920 nm) of *Convallaria* rhizomes are reported.

3.1. Introduction

Multiphoton microscopy imaging modalities, such as two-photon excited fluorescence microscopy (TPM) and second harmonic generation (SHG) imaging, have the potential to provide clinically useful information to advance disease diagnosis [62]. During multiphoton imaging, high temporal energy densities are used to induce non-linear effects in tissue, such as simultaneous absorption of two red photons to excite a molecular UV transition or non-linear scattering.

Two-photon excitation (TPE) occurs when two photons combine to induce an electronic transition equivalent to the sum of the energy of both photons, causing the fluorophore to emit at a wavelength shorter than the excitation wavelength [63,64]. SHG is produced when non-centrosymmetric structures of tissue, such as collagen fibrils, bone matrix, or microtubules [65,66] allow optical field oscillation at twice the frequency of the incident field, thus creating photons at

exactly half the wavelength of the incident optical field [65]. The longer excitation wavelengths used by TPM and SHG allow for greater tissue penetration, up to three times deeper than confocal microscopy [67]. Other advantages of multiphoton imaging modalities compared to single photon excitation include the inherent sectioning capability of multiphoton imaging, ease of filtering emission light from excitation light compared to single photon fluorescence, and negligible out of focus phototoxicity [67].

The development of miniature two-photon imaging probes began in 2001 with a publication by Helmchen *et al.* [68]. Since that publication, which focused on a "wearable" system for imaging of the brain in freely moving rats, the range of envisioned applications and miniature optical designs has broadened. Miniature multiphoton microscopes are now being developed for use to perform *in vivo* imaging for early cancer detection and cancer research [69–71]. The motivation for miniaturization is to deploy multiphoton imaging deep within intact living tissues or to access organ sites where a conventional microscope cannot reach. This can lead to real-time diagnosis and increased accessibility of research targets, therefore diminishing the need for invasive surgical biopsy or destructive sample preparation. Some applications of miniature multiphoton microscopes include detection of skin cancer [72,73], bladder cancer [62], imaging of gastrointestinal mucosa at the cellular level [74], brain imaging in live animals [25,38,75], imaging within the pancreatic duct [76], and imaging of the kidney and esophagus in live animals [70].

Most of the miniature microscope designs employ radial GRIN optics to focus light in tissue [25,40,70,72,77]. However, GRIN lenses were originally developed for coupling light into an optical fiber and not for imaging [78]. Thus, while GRIN lenses can be fabricated in a small size at a low cost, the design degrees of freedom are limited to the diameter, length, and doping profile of the GRIN material and are not enough to fully correct for aberrations which limit image quality and image size. Adding an additional non-GRIN lens on the distal end of the GRIN objective can help to increase the FOV and the NA and to compensate for aberrations introduced by the GRIN lens. However, this is still not enough to provide good image quality across a reasonable FOV for medical imaging.

An alternative to using GRIN lenses as the focusing optics for endomicroscopes is the following ultra-slim objective composed of plastic lenses. The design has a comparable OD to, and larger FOV than, current GRIN objectives [43]. The plastic objective can also maintain consistent performance across the entire FOV, as opposed to commercial GRIN objectives [42].

3.2. Plastic optics for endomicroscope design

3.2.1. Ensuring high quality, low cost objectives

Plastic optical systems are inherently mass-producible at low unit cost. As such, they have the potential to become a consumable element of a clinical exam, following the favored "razor/razor-blade" product model. Plastic optics can be fabricated through injection molding or single point diamond turning (SPDT). From

a fabrication standpoint, there is no difference between spherical or aspheric surfaces. As a consequence, spherical aberration and other monochromatic aberrations may be corrected with simpler design forms than when only spherical surfaces are available. High-precision element and assembly tolerances can be achieved, in part because optical and mechanical features can be fabricated as part of the same process [47,79]. Miniature objectives utilizing plastic lenses have been constructed with DXRLE springs and spacers which reduce assembly time while maintaining high performance [49,80]. DXRLE stands for direct x-ray lithography and electroplating, and is a process which allows for the creation of incredibly precise metallic parts, with tolerances on the order of microns. Custom DXRLE parts were designed and fabricated to act as the alignment components of the ultra-slim objective; their parameters and use are described further in Section 3.4.

3.2.2. Properties of optical plastics with regards to non-linear imaging

Below, the properties of several optical plastics are analyzed to optimize the performance of a non-linear imaging endomicroscope objective. Where applicable, these properties are compared to common optical glasses to provide a reference. When selecting the optical plastic to be used for the creation of the two-photon ultra-slim objective, several material property criteria were considered, including light transmission rate, excitation-induced autofluorescence, induced birefringence due to injection molding, water absorption, heat resistance, and pulse broadening due to group velocity dispersion.

A drawback of using plastic optics is that the available materials offer only a small range of Abbe numbers and indices of refraction compared to the glass catalog. As a result, it is difficult to correct for chromatic aberrations by achromatizing the objective design. Fortunately, a common feature of SHG and TPM is that the excitation light only causes emission from a small voxel of tissue. As a result, the resolution of the endomicroscope objective depends only on the excitation point spread function, so the objective needs to be well corrected only for the excitation wavelength.

Four common optical plastics were considered. Candidate plastics were Zeonex E48R, which is a cyclo olefin polymer (Zeon Chemicals L.P.), poly(methyl methacrylate) (PMMA, commonly known as acrylic), polystyrene (PS), and polycarbonate (PC) [81]. Their refractive properties (as well as those for the optical glasses BK7 and BaSF10 [82]) are listed in Table 3.1. E48R and PMMA behave similarly to crown glasses such as BK7. PS and PC, on the other hand, are more like flint glasses, such as BaSF10. With SPDT, the fabrication method selected to create the lenses in the prototype ultra-slim objective, a high-quality diamond tool is used to directly shape the optical surface of the lenses. Because PC quickly degrades the diamond tools when it is used as a substrate for SPDT, it was not prepared for examination.

Table 3.1. Refractive Properties of Four Optical Polymers and Two Common Glasses

Property	E48R	PMMA	PS	PC	BK7	BaSF10
Index of Refraction	1.53	1.49	1.57	1.57	1.51	1.65
Abbe Number	56	57	29	28	64	39

3.2.3. Transmission properties of select optical plastics

The transmission profiles of E48R, PMMA, and PS were measured with a Cary5 spectrophotometer (Agilent Technologies). As shown in Figure 3.1, E48R and PMMA have similar transmission profiles, passing light from 350 nm through 1100 nm; this range is crucial because the samples will be excited at 780 nm during SHG and at 920 nm during TPM and emit at 390 nm during SHG and between 460 nm and 550 nm during TPM for the selected sample (see Section 3.5.2).
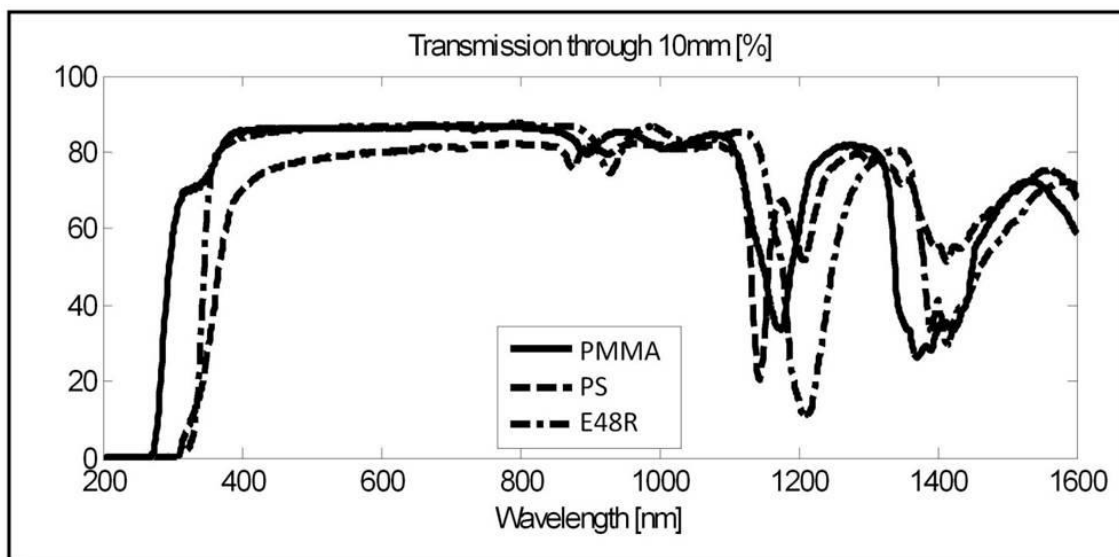
Figure 3.1. Wavelength dependent transmission through optical plastics.

3.2.4. Autofluorescence properties of optical plastics compared to fluorescent solution

A FluoroLog®-3 spectrofluorometer (HORIBA Scientific, Edison,) measured the fluorescence spectra of the plastics, as well as a 0.1 microgram per milliliter (μg/mL) solution of fluorescein, a common fluorophore. The results in Figure 3.2a show fluorescein has a peak in emission intensity at 490 nm excitation; this excitation wavelength is important because the Argon Ion laser commonly used for fluorescence imaging emits at 488 nm. In the excitation bandwidth from 450 nm to 510 nm, the fluorescein solution has an emission intensity that is significantly stronger than the autofluorescence of E48R, PS, and PMMA. Over the specified range, the signal from fluorescein is 10 to 90 times stronger than the signal from E48R, 15 to 100 times stronger than the signal from PS, and 100 to 935 times stronger than the signal from PMMA. As the excitation wavelength increases, the autofluorescence signal generated in E48R, PS, and PMMA decreases. Even at 650 nm, the longest excitation wavelength generated for Figure 3.2, E48R, PS, and PMMA had signals that were only 2.9, 3.7, and 1.3 times stronger than the background produced by a water standard, respectively. Other studies have demonstrated the trend of decreasing autofluorescence with increasing wavelength in optical plastics, including PMMA and PC. At 780 nm, both PMMA and PC have low autofluorescence levels which are comparable to glass [83]. Additionally, because the beam never focuses within the lens material, it can be safely assumed that there is no TPE fluorescence to generate an autofluorescence signal.
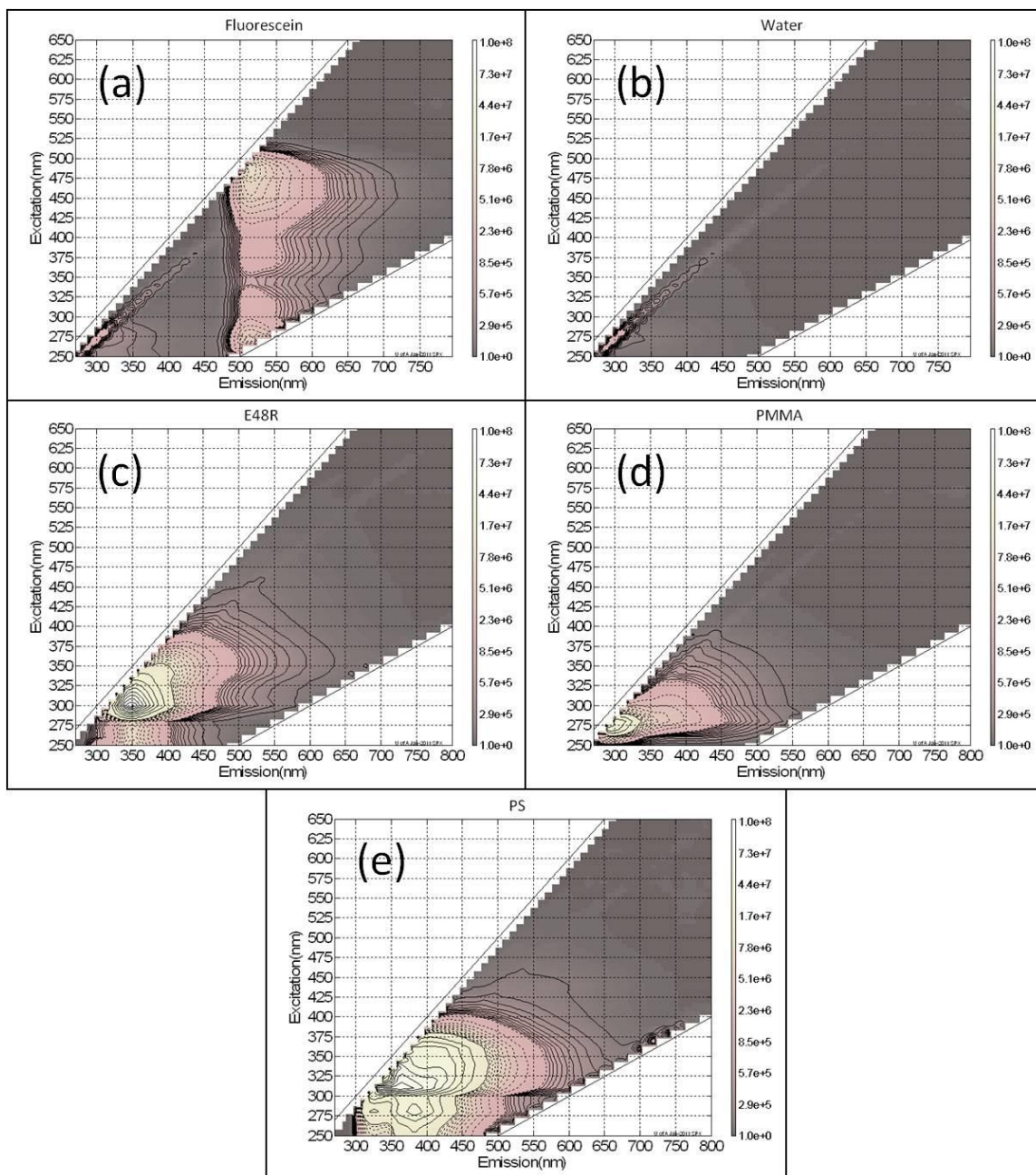
Figure 3.2. Autofluorescence data for (a) a 1 μm/mL solution of fluorescein, (b) water, (c) E48R, (d) PMMA, and (e) PS. The X-axis plots the emission wavelength in nanometers, the Y-axis displays the excitation wavelength in nanometers, and color indicates autofluorescence intensity in arbitrary units. Note that the excitation, emission, and intensity scales are the same for all five graphs.

3.2.5. Physical comparison of optical plastics

Both E48R and PMMA have low injection-molding-induced birefringence, while PS and PC are much more susceptible to induced birefringence [84]. It is critical that unintended birefringence be minimized because it has been shown to significantly lower the Strehl ratio of miniature, plastic optical systems [50]. E48R has significantly lower water absorption than PMMA, PS, and PC: <0.01% compared to approximately 0.3%, 0.03-0.1%, and 0.2%, respectively [81,85]. This is particularly important for the first lens in the system, which is in an aqueous environment during imaging. Less water absorption reduces the amount of deformation undergone by the lens' surface, which in turn reduces the degradation of the optical performance. Water absorption also causes a change in the index of refraction of the optical material, which can further reduce performance of the objective. E48R also has higher heat resistance compared to PMMA, which further increases its ability to maintain high quality optical performance [84].

Because the lenses are intended to be used *in vivo*, it is important to determine the potential toxicity of the plastics. PMMA, cyclo oelfin polymers, and PC have been shown to be biocompatible as bone cement, which requires them to be implanted for far longer than they would be used for imaging [86–88]. PS has actually been used to prevent cytotoxicity *in vivo* [89]. Clearly, any of the optical plastics have sufficient biocompatibility to form the lenses of an *in vivo* optical system.

3.2.6. Pulse broadening due to group velocity dispersion in select optical plastics and glasses

As with conventional TPM using glass optics, pulse broadening due to group velocity dispersion (GVD) is a concern [90]. However, the literature regarding group velocity dispersion in plastic is very sparse [91]. As the pulse width of the excitation light increases, a higher intensity pulse is necessary to maintain the generation of the signal, which risks damage to both the tissue and the plastic lenses (see the optical design in Section 3.4). The group delay dispersion (GDD) for the material was calculated from the GVD,

$$\text{GDD} = \text{GVD} \times L,$$

Equation 3.2. Group delay dispersion

where L is the length of material the light propagates through. GDD represents the amount of dispersion, and thus pulse broadening, through a particular system. GVD can be calculated using the equation from [90]

$$\text{GVD} = \frac{\lambda^3}{2\pi c^2} \frac{d^2 n}{d\lambda^2},$$

Equation 3.3. Group velocity dispersion

where λ is the wavelength of light at the source, n is the index of refraction, and c is the speed of light. Equation 3.3 requires the second derivative of the index of refraction to be calculated in terms of wavelength. The second derivative is found by starting with the equation for n using the modified Cauchy equation and the accompanying dispersion coefficients provided in [92]

$$n = \left(A_1 + A_2\lambda^2 + \frac{A_3}{\lambda^2} + \frac{A_4}{\lambda^4} + \frac{A_5}{\lambda^6} + \frac{A_6}{\lambda^8} \right)^{\frac{1}{2}}.$$

Equation 3.4. Modified Cauchy equation

Taking the second derivative with respect to λ leads to

$$\frac{d^2n}{d\lambda^2} = \frac{1}{2}\left\{ \begin{array}{l} \frac{-1}{2}\left[\left(A_1 + A_2\lambda^2 + \frac{A_3}{\lambda^2} + \frac{A_4}{\lambda^4} + \frac{A_5}{\lambda^6} + \frac{A_6}{\lambda^8} \right)^{-\frac{3}{2}} \left(2A_2\lambda - 2\frac{A_3}{\lambda^3} - 4\frac{A_4}{\lambda^5} - 6\frac{A_5}{\lambda^7} - 8\frac{A_6}{\lambda^9} \right)^2 \right] \\ + \left(A_1 + A_2\lambda^2 + \frac{A_3}{\lambda^2} + \frac{A_4}{\lambda^4} + \frac{A_5}{\lambda^6} + \frac{A_6}{\lambda^8} \right)^{-\frac{1}{2}} \left(2A_2 + 6\frac{A_3}{\lambda^4} + 20\frac{A_4}{\lambda^6} + 42\frac{A_5}{\lambda^8} + 72\frac{A_6}{\lambda^{10}} \right) \end{array} \right\}.$$

Equation 3.5. Second derivative of the modified Cauchy equation

which can be used to solve for GVD and, in turn, GDD.

Table 3.2 contains the GDD and GVD data for E48R, PMMA, PS, PC, BK7, and BaSF10. At 780 nm, BK7 has the lowest GVD (and thus creates the smallest amount of pulse broadening). PMMA, E48R, and BaSF10 all have similar dispersions, which are lower than those for PS and PC. All the materials have lower dispersion at 920 nm than at 780 nm. Note that for PMMA and E48R, the GVD is negative at 920 nm; this will create pulse broadening of the same magnitude but in the opposite direction of the pulse as would occur if the GVD was positive [90]. It also means that PMMA or E48R could be combined with PC or PS to achieve near zero net GDD at this wavelength.

The GDD data can be used to calculate the change in pulse width caused by propagation through the material with the equation [90]

$$\Delta t_{out} = \frac{\sqrt{\Delta t^4 + 16(\ln 2)^2 (GDD)^2}}{\Delta t},$$

Equation 3.6. Change in pulse width due to group delay dispersion

where Δt is the pulse width of light entering the objective and Δt_{out} is the pulse width upon exiting the material. Table 3.2 shows that, for a 130 fs pulse traveling through 7 mm of material (an amount approximately equal to the length of the ultra-slim objective), the pulse width has broadened by 2.9 fs or less, depending on the material. The pulse width of 130 fs is the duration of the pulses used to perform the initial SHG and TPM imaging described in Section 0. The wavelengths of 780 nm and 920 nm are used for SHG and TPM in the imaging experiments described in Section 3.5.1 and Section 3.5.2, respectively. This demonstrates that the objective does not significantly contribute to pulse broadening for the given experimental setup. However, for shorter pulses, GVD becomes a significant factor with regards to pulse broadening. Table 3.2 shows that when the initial pulse width is reduced to 10 fs, the change in pulse width due to GVD increases by anywhere from a factor of two to more than an order of magnitude. Note that glass suffers from similar pulse broadening at this pulse width and wavelength.

Table 3.2. Group Velocity Dispersion Data for Six Optical Materials

Property	Δt	PMMA	E48R	PS	PC	BK7	BaSF10
GVD_{780nm} (fs^2mm^{-1})		104.1	104.9	173.8	183.8	55.5	106.7
GDD_{780nm} (fs^2)[a]		0.73	0.73	1.22	1.29	0.39	0.75
GVD_{920nm} (fs^2mm^{-1})		-31.4	-11.5	57.3	39.7	42.2	83.1
GDD_{920nm} (fs^2)[a]		-0.22	-0.08	0.40	0.28	0.30	0.58
$\Delta t_{out, 780nm}$ (fs)	130	130.9	130.9	132.6	132.9	130.6	131.0
$\Delta t_{out, 780nm}$ (fs)	10	202.4	203.8	337.5	356.9	108.3	207.2
$\Delta t_{out, 920nm}$ (fs)	130	130.1	130.0	130.3	130.1	130.2	130.6
$\Delta t_{out, 920nm}$ (fs)	10	61.7	24.5	111.7	77.7	82.6	161.7

[a]GDD is calculated for the pulse travelling through 7 mm of material.

3.2.7. Justification of the selected optical plastic

Zeonex E48R was selected as the optical material for the ultra-slim, non-linear endomicroscope objective. It has similar properties to PMMA in terms of index of refraction, Abbe number, light transmission, induced birefringence, and pulse broadening. E48R has superior heat resistance and reduced water absorption. PMMA has better autofluorescence characteristics at single-photon excitation wavelengths compared to E48R; however, our objective is designed for use in the near-IR, where autofluorescence of plastics is negligible. More important is the ability to resist water absorption, as the objective is designed for *in vivo* use and thus will experience water immersion in object space.

3.3. Overview of the ultra-slim endomicroscope objective

To demonstrate that plastic optics can be used for non-linear imaging an ultra-slim endomicroscope objective has been designed, constructed, and tested. Compared to a previous ultra-slim objective design [47], this objective has been modified for use with multiphoton imaging and to improve tolerancing of the design based on the assembly procedures. The design has been incorporated into a 1.27 mm OD hypodermic tube. A summary of the design specifications is given in Table 3.3.

Table 3.3. Design specifications of the Non-Linear Ultra-Slim Objective

Object Space NA[a]	0.4
Image Space NA	0.125
Field of View	250 μm
Clear Aperture	0.8 mm
Magnification	-3.2
Working Distance[a]	200 μm
Wavelength	900 nm
Telecentricity	Object Space

[a]Object space is designed for water immersion.

The object space NA of 0.4 provides a nominal lateral resolution of 1.19 μm for an illumination wavelength of 780 nm and a resolution of 1.40 μm for an illumination wavelength of 920 nm. The theoretical depth of field is 6.48 μm at 780 nm and 7.65 μm at 920 nm in tissue. During SHG and TMP, however, the lateral resolution and depth of field may be significantly smaller due to non-linear effects [93].

The FOV of 250 μm was selected to ensure that a sufficient number of epithelial cells will be seen within a single image. The ability to image a large number of epithelial cells is important because early diagnosis of cancer typically takes place by examining the tissue for suspicious lesions; in order to detect these lesions and differentiate them from healthy tissue, clinicians desire a large FOV with subcellular resolution [94]. Object space telecentricity ensures that the image magnification is independent of the object's position in, or distance from, the focal plane.

3.4. Optical design of the ultra-slim objective

ZEMAX (Radiant Zemax, LLC.) was used to design a lens system which meets the specified criteria. It utilizes three custom plastic lenses which incorporate aspheric surfaces to aid in the correction of aberrations. The design is illustrated in Figure 3.3. The object surface has a curvature (radius of 0.8 mm across the 250 μm FOV), which helps to correct for aberrations in the system. This is allowable because the objective is intended to image three-dimensional tissues and the sag introduced by the curved image plane is less than 10 μm, which is the approximate thickness of a single layer of epithelial cells. The prescription data for the design is listed in Table 3.4. Zeonex E48R, the selected optical plastic, can be shaped through SPDT and injection molding to produce high quality optical components. For prototyping, SPDT was used to create the lenses, as it allows a small numbers of parts to be made and can easily accommodate changes in design. Ultimately, injection molding will be used to fabricate larger quantities of lenses.
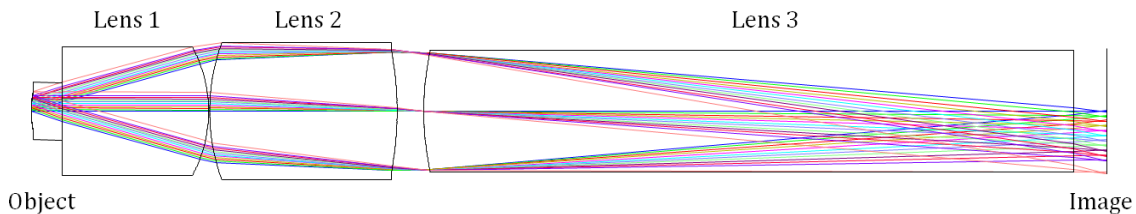
Figure 3.3. Schematic of the ultra-slim objective optimized for two-photon imaging. Total length: 6.98 mm.

Table 3.4. Lens Prescription Data

Surface	Comment	Radius (mm)	Thickness (mm)	Material	Conic
Object	Tissue	0.8000	0.200	SEAWATER	0.0000
1	Lens 1	Infinity	0.950	E48R	0.0000
2		-0.8613	0.007		0.0000
3	Lens 2	1.2744	1.217	E48R	0.0000
4		-1.9356	0.173		-12.1922
STOP	Lens 3	1.7992	4.219	E48R	-0.4300
5		Infinity	0.217		0.0000
Image		Infinity	0.000		0.0000

The objective is assembled within an 18 gauge hypodermic tube (Small Parts, Inc), which has an 1.27 mm OD and an inner diameter of 1.072 mm. This is the same gauge as the narrowest core biopsy needles. The lenses are assembled with a single type of DXRLE part; each identical part acts as both a spring and a spacer to aid in alignment of the lenses within the hypodermic tube (Figure 3.4). The OD of the first lens is precisely controlled so that it can be press-fit into the hypodermic tubing. The lens is pushed into place using a 1.072 mm precision gage pin (Deltronic) so

that 100-200 μm of lens material extends beyond the edge of the tube. Two 85 μm thick springs, each having an OD of 1.122 mm when the arms are fully extended, are inserted between the first and second lenses, then pressed into place using the gage pin. The springs serve several purposes. They precisely define the spacing between lenses to within 10 μm in order to create an air gap with the designed thickness [49]. They force the lenses to center within the tube to a tolerance of less than 10 μm, with less than 3 mrad of tilt [49]. These values are within the tolerances budgeted for the design. The springs also limit the clear aperture of the lenses to 0.8 mm. Three more springs are placed between lens two and lens three. A final spring is placed after the third lens to hold the components in place. Norland optical adhesive (NOA) 61 (Norland Products, Inc.) is used to seal the object side of the ultra-slim objective for water immersion.

The imaging performance of the ultra-slim objective was evaluated using a 1951 USAF resolution target (NT36-275, Edmund Optics Inc.) by estimating the Strehl ratio (SR). The SR, which is the ratio of peak irradiance in the Airy disk from the experimental system to the peak irradiance in the Airy disk of a diffraction-limited system, can be estimated by finding the ratio of the area under the modulation transfer function (MTF) of the measured system to the that of the theoretical diffraction-limited system. For the ultra-slim objective, the SR was estimated by imaging a black and white edge on the resolution target with 800 nm trans-illumination and performing the slanted edge MTF technique [95,96] near the center of the FOV. This technique estimates the MTF of the system by measuring the contrast between the black and white regions at the detector. This data can be used

to find the MTF of the experimental system, and from that to estimate the SR. The objective used to perform the study in Section 3.5 had a SR of 0.85; a value above 0.8 is generally considered diffraction-limited performance. The measured magnification at the image plane was 3.19.
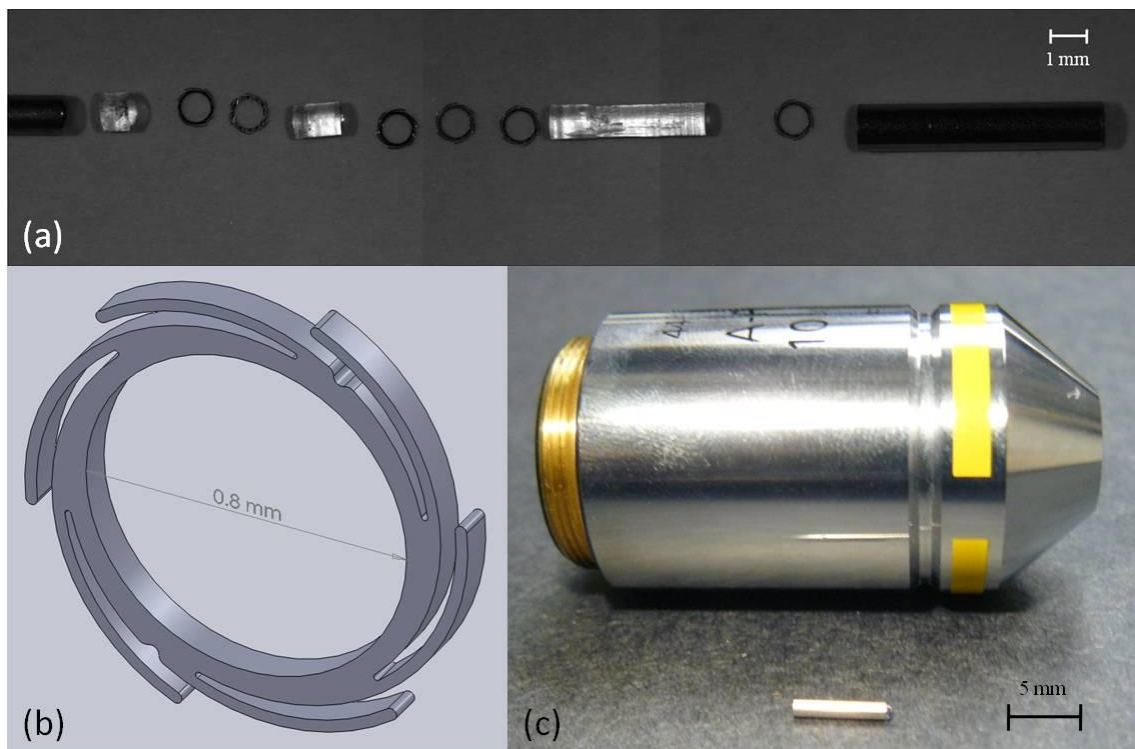
Figure 3.4. (a) Exploded view of an ultra-slim objective. The left rod is a precision gage pin used to insert the parts into the hypodermic tubing. The clear plastic pieces are the custom lenses. The circular rings are DXRLE springs which act as alignment devices and apertures. On the right is the hypodermic tubing used to house the objective. (b) SolidWorks model of the DXRLE springs. (c) The ultra-slim objective next to a conventional microscope objective for size comparison.

3.5. Multiphoton microscopy imaging results through the all-plastic objective

A benchtop microscope system (TrimScope, LaVision BioTec) was used to perform SHG and TPM through the ultra-slim objective. The samples were excited using a Chameleon Ultra 2 Ti:Sapphire laser (Coherent Inc). The pulse width at the source is 130 fs and has a repetition rate of 80 MHz. The average power at the input of the ultra-slim objective was 5 mW for both SHG and TPE. Each image was recorded through non-descanning reverse detection. The ultra-slim objective imaged the sample and a commercial objective (UPlanFL 4×/0.13, Olympus Corp) on the benchtop system relayed the intermediate image plane to a photomultiplier tube (PMT) detector in non-descanned configuration. A diagram of the experimental setup is illustrated in Figure 3.5. Two samples, rat-tail collagen fibers and *Convallaria*, commonly known as lily of the valley, were imaged to test the capabilities of the plastic objective to image via SHG and TPM, respectively.
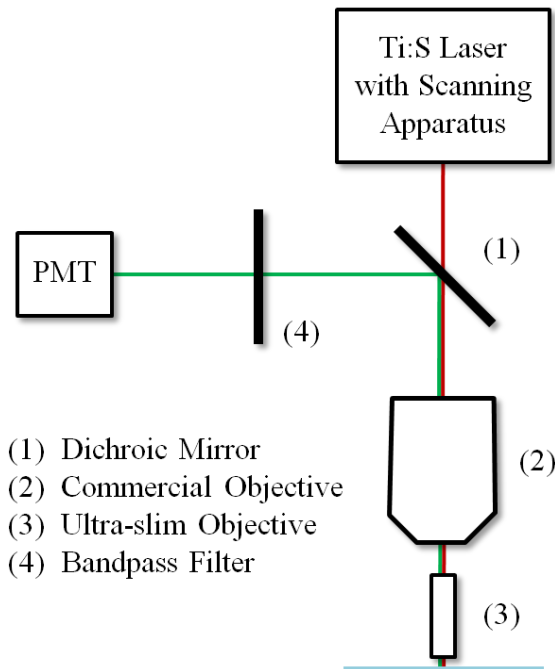
Figure 3.5. Schematic of the non-linear imaging setup used to test the ultra-slim objective. The light was generated by a laser and scanned through a dichroic mirror (1) and into a commercial, NA 0.13 objective (2). The excitation light was focused by the commercial objective onto the back image plane of the ultra-slim objective (3), which transferred the light onto the sample. The emission light was collected by the ultra-slim objective, relayed by the commercial objective, and reflected by the dichroic mirror before passing through an emission filter (4) and being detected by a PMT.

3.5.1. Imaging SHG in rat-tail collagen fibers

The rat-tail collagen fiber sample was extracted from the rat-tail, fixed, and attached to a glass slide. The specimen was illuminated at 780 nm and observed through a bandpass filter centered at 377 nm with a 50 nm bandwidth (FF01-377/50, Semrock Inc) after reflecting off a 405 nm dichroic mirror (Di01-R405-25x36, Chroma Technology Corp). Figure 3.6a shows an image of a single slice of rat-tail collagen obtained with SHG. Notice the striation of the collagen fibers.
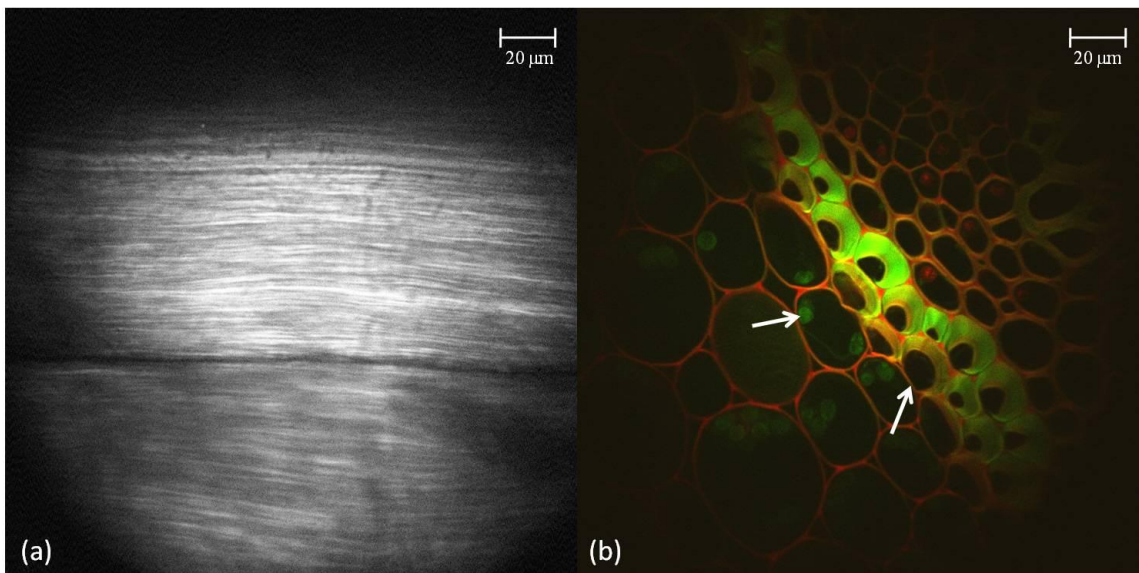
Figure 3.6. (a) An enlarged view of a rat tail tendon optical section taken via SHG with the ultra-slim objective in series with the benchtop system. (b) A false-color image shows *Convallaria* cells imaged via TPM at two different wavelengths, also with the ultra-slim objective. The left arrow points to a green nucleus and the right arrow points to a red cell membrane.

3.5.2. Imaging TPE fluorescence in *Convallaria*

A *Convallaria* rhizome cross-section specimen was used to test the capability of the plastic objective to image TPE signal. The *Convallaria* specimen was stained with acridine orange, mounted beneath a glass coverslip, and imaged through a layer of water between the glass and the ultra-slim objective. The specimen was illuminated at 920 nm and observed through a 680 nm shortpass filter in series with a standard GFP emitter bandpass filter.

Figure 3.6b shows a false-color image of the *Convallaria* sample via the ultra-slim endomicroscope objective. Green light corresponds to a signal which has been filtered through a bandpass filter centered at 460 nm with a bandwidth of 80 nm (FF02-460/80, Semrock) and detected by a Galium Arsenide PMT (H7422A-40,

Hamamatsu), while red light corresponds to a signal which has passed through a 505 nm dichroic mirror (505DCXR, Chroma) before being filtered by a bandpass filter centered at 550 nm with a bandwidth of 88 nm (FF01-550/88, Semrock) and detected by a Bialkali PMT (H6780-01, Hamamatsu). Notice the ability of the objective to resolve subcellular features such as nuclei and cell membranes.

3.6. Discussion

The ability to perform TPM and SHG imaging has been demonstrated using a 1.27 mm OD, NA0.4, FOV = 250 μm objective utilizing all-plastic lenses. To the best of our knowledge, this is the smallest integrated microscope objective of this type ever made. The ultra-slim objective demonstrates diffraction-limited performance and was designed as a prototype to be used for non-linear endoscopic imaging. It can be used to acquire high resolution, high contrast *in vivo* images with no need for exogenous contrast agents to provide morphological information for diagnostic applications, such as early cancer detection. The ultra-slim objective is envisioned as being used to probe tissue that has already been deemed abnormal by large FOV, low resolution imaging such as traditional endoscopy; the ultra-slim objective is narrow enough to fit through a standard port on an endoscope. Ultrasound imaging [97], MRI [98], and positron emission mammography [99] are other large FOV, low resolution imaging techniques which have been used to guide conventional biopsy needles to suspicious tissue; it is feasible to also perform a similar procedure with the ultra-slim objective.

3.7. Acknowledgments

<div align="right">

Chapter 4

</div>

Achromatized endomicroscope objective for optical biopsy

*The contents of this chapter were published in the following journal article: M. Kyrish and T. Tkaczyk, "Achromatized endomicroscope objective for optical biopsy," Biomed. Opt. Express 4, 287-297 (2013)

In Chapter 3, an ultra-slim, endomicroscope objective was demonstrated which is approximately same size as a biopsy needle. However, the objective is monochromatic, which means it can only bring a single wavelength of light into focus at one time and cannot be used to image multiple fluorophores simultaneously. In order to bring more than one fluorophore into focus at once and thus perform digital staining, an achromatic objective is needed. Achromatizing can also improve the collection efficiency when there is a Stokes shift [100], allowing the contrast of optically sectioned images to be improved by co-localizing excitation and emission planes.

The following chapter presents a proof-of-concept prototype that validates the optical design of an achromatic NA0.4 objective. The objective, built with plastic lenses, has a 0.9 mm clear aperture and is achromatized from 452 nm to 623 nm. The objective's measured Strehl ratio is 0.74 ± 0.05 across a 250 μm FOV. Optical sectioning was performed via structured illumination through the objective while capturing fluorescence images of breast carcinoma cells stained with proflavine and cresyl violet. This technology has the potential to improve optical biopsies and provide the next step forward in cancer diagnostics.

4.1. Introduction

Breast cancer diagnoses typically require removing tissue samples or cells via invasive biopsy before a pathologist examines them with a bench top microscope. A potential alternative to conventional biopsies is an "optical biopsy," which uses a ultra-slim endomicroscope to provide real-time, *in vivo* microscopy images without tissue removal. Optical biopsies should provide similar results to the current gold standard for diagnosis: conventional biopsy followed by H&E histology staining. Therefore, endomicroscopes should have sub-cellular resolution, optical sectioning capability, and the ability to image multiple dyes simultaneously.

In this chapter, a prototype system is presented which validates the optical design of an achromatized objective. The proof-of-concept demonstrates the ability to create an achromatized objective composed only of plastic lenses having clear aperture of 0.9 mm and NA = 0.4. The prototype is the precursor to a higher NA

achromatic objective the approximate width of a biopsy needle which is integrated into an endomicroscope that achieves optical sectioning via structured illumination (Chapter 6).

4.2. Design of the ultra-slim achromatic objective

4.2.1. Optomechanical design specifications of the achromatic objective

The ultra-slim, all-plastic objective has been designed to achieve diffraction-limited performance across a 171 nm wavelength range within the visible spectrum following the specifications listed in Table 4.1. The objective is intended to work with two fluorescent dyes, proflavine and cresyl violet, which stain the nucleus and cytoplasm, respectively. Proflavine has excitation and emission peaks at 452 nm and 515 nm. Cresyl violet has excitation and emission peaks at 575 nm and 623 nm.

Table 4.1. Achromatic ultra-slim objective design specifications

Object Space NA[a]	0.4
Image Space NA	0.14
Field of View	250 μm
Clear Aperture	0.9 mm
Magnification	-2.88
Working Distance[a]	15 μm
Wavelength Range	452-623 nm
Telecentricity	Object Space

[a]Object space is intended for water immersion.

At the center wavelength of 538 nm, an NA0.4 objective provides a diffraction-limited resolution of 0.82 μm. A 0.9 mm clear aperture will allow the objective to be integrated with an endomicroscope to perform optical biopsies. The magnification matches the 250 μm FOV to the 720 μm imaging area of the endomicroscope's fiber bundle. The short, 15 μm working distance allows the objective to image tissue while in direct contact. Telecentricity is maintained in object space. A separate publication reported that achieving image space telecentricity would mean compromising transverse magnification and performance at the edge of the image [47]. To counteract this effect, the principal ray angle was allowed to deviate from 0°. The analysis shows that, while this created some vignetting, the image quality is higher than if the design were strictly image space telecentric.

The justification for using plastic as a lens material, particularly during fluorescence imaging, is thorough detailed in Section 3.2. To summarize, the first and last lenses are composed of Zeonex E48R due to its crown-like optical properties and very low water absorption. Both doublets are made of PMMA, NOA61, and polystyrene. PMMA is a crown-like plastic while polystyrene behaves like a flint, allowing achromatization. The plastics have high transmission and negligible autofluorescence across the design wavelength range. The process for creating aspheres in plastic lenses is identical to creating spheric surfaces, allowing simpler, cheaper designs using fewer components than glass.

4.2.2. Achromatic objective lens prescription and expected performance

A lens prescription meeting the design requirements was developed in ZEMAX (Radiant Zemax, LLC.) and is listed in Table 4.2. The objective design layout is illustrated in Figure 4.1 and the nominal performance is shown in Figure 4.2. Figure 4.2(a) plots the polychromatic MTF of the achromatic objective; it has diffraction-limited performance except for the sagittal ray at edge of the FOV for polychromatic light. Figure 4.2(b) shows the image space chromatic focal shift; the maximum shift, 3.2 μm, is much shorter than the diffraction-limited range of 22.0 μm. For this particular lens system, the expected transmission efficiency based on the Fresnel equations and the transmission rates measured in Kyrish et al. [101] and Section 3.2.3 is 58%; however, Tkaczyk et al. [102] created a significant improvement in their microscope's throughput by adding AR coatings to the plastic lenses. This procedure can be used in the future to improve the transmission efficiency of the achromatic objective.
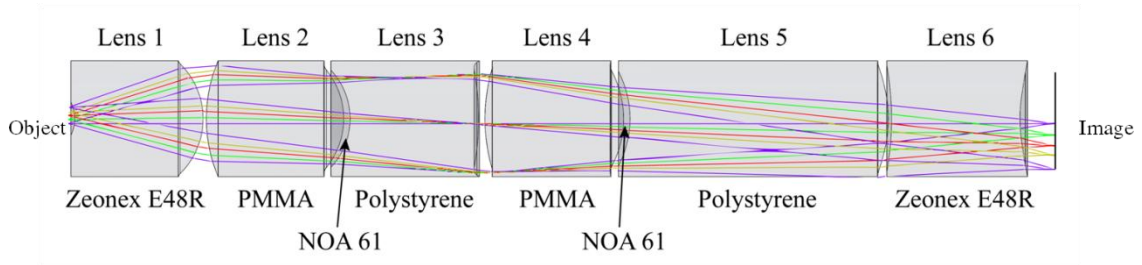
Figure 4.1. Schematic representation of the achromatic objective. The diameter of the lenses is 0.9 mm.

Table 4.2. Lens prescription of the achromatic objective

Notes	Radius (mm)	Thickness (mm)	Glass	4th Order Aspheric Term	6th Order Aspheric Term	8th Order Aspheric Term
Object	1.50000	0.046	Seawater			
Lens 1	-0.29789	1.000	E48R			
	-0.62850	0.025				
Lens 2	1.13232	1.070	PMMA	-0.095743	0.579417	-1.044467
	-0.59716	0.050	NOA61			
Lens 3	-0.54874	1.000	Polystyrene			
	-2.26094	0.000		-0.093718	0.831976	-3.102985
Stop	Infinity	0.050				
Lens 4	1.35360	1.080	PMMA	-0.048849	-0.026626	
	-0.78475	0.050	NOA61			
Lens 5	-0.79370	2.012	Polystyrene			
	-1.00743	0.025		0.392702	-0.165720	0.183568
Lens 6	-2.31762	1.000	E48R			
	1.16361	0.286		-0.860845		
Image	Infinity					

A thorough tolerancing of the design was also performed in ZEMAX. The tolerances listed in Table 4.3 are based on in-house fabrication capabilities. The lenses were formed via SPDT using an ultra-precision lathe. Injection molding can be used to mass produce the lenses; for injection molding, the tolerances are considered commercial or state-of-the-art [81].

(a) **Polychromatic MTF Plot**　　(b) **Chromatic Focal Shift**
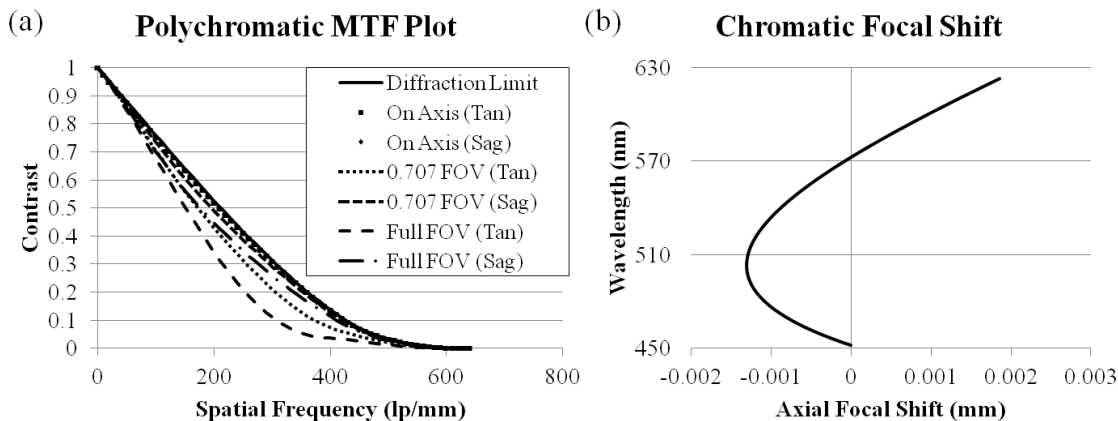
Figure 4.2. Nominal performance of the achromatic objective. (a) Diffraction-limited polychromatic MTF. (b) Diffraction-limited image space chromatic focal shift.

Table 4.3. Tolerancing of the achromatic objective

Tolerand	Value
Radius of curvature (%)	±1
Thickness (μm)	±20
Element decenter (μm)	±10
Element tilt (°)	±0.15
Doublet decenter (μm)	±15
Doublet tilt (°)	±0.2
Surface irregularity (fringes)	±1
Index (%)	±1
Abbe Number (%)	±1

4.3. Fabrication and assembly

A design proof-of-principle prototype of the ultra-slim achromatic objective was built in 22 mm diameter plastic disks; while too large to be used in an endomicroscope, this allows the optical design to be validated. The fabrication process is similar to that described by McCall et al. [79]; using SPDT, the optical

surfaces and the optomechanics were cut into the disks, creating positive and negative alignment features in the same material as the lenses. Using SPDT to simultaneously create the optics and the mechanics maintains tight tolerances for radius, thickness, decenter, tilt, and surface irregularity.

The objective was modeled in SolidWorks (Dassault Systèmes SolidWorks Corp.); a cutaway view is shown in Figure 4.3(a). The positive annular features on the bottom of each lens are designed to be concentric with the negative triangular features of the following lens at two points. Blue permanent marker is added 5 mm away from the optical axis up to the edge of the clear aperture of each optical surface, creating baffles within the objective. These baffles reduce stray light, maintaining high image contrast. Cemented doublets are held together by applying NOA61 directly to the concave optical surface. The lenses are stacked two at a time while mating the positive and negative alignment features. This procedure centers the lenses and ensures the designed spacing is maintained through the optical system. The adhesive is then cured with ultraviolet light. For the non-doublet lens pairs, a small amount of glue is added to the grooves and the edge of the discs before stacking the components. Figure 4.3(b) shows lenses 2 and 3 from Figure 4.1 next to a US quarter. Figure 4.3(c) presents a fully assembled achromatic objective.
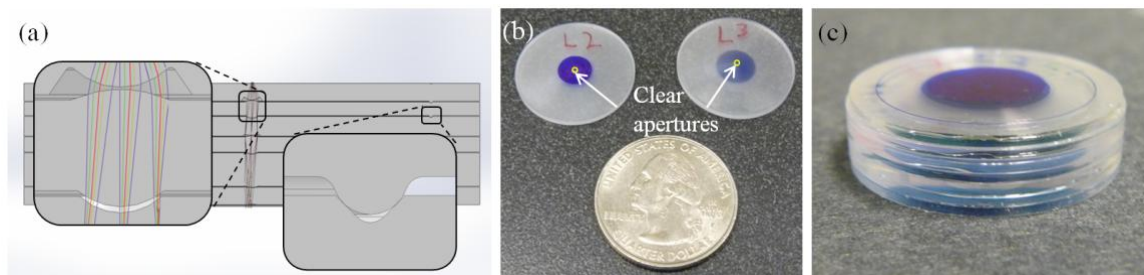
Figure 4.3. (a) SolidWorks cutaway of the assembled achromatic objective with built-in alignment features. The insets show optical surfaces (left) and alignment features (right). (b) Example of two singlet lenses next to a US quarter with the clear apertures of the lenses circled. (c) Fully assembled prototype achromatic objective.

4.4. Characterizing and testing the achromatic objective

The functionality and performance of the achromatic objective were thoroughly characterized. First, doublet lenses were cut and assembled in order to measure their tilt and decenter. Next, the lateral performance and chromatic focal shift of a fully assembled objective were measured. Finally, the objective was used to image breast carcinoma cells which were stained with multiple fluorescent dyes. In order to demonstrate the limitations of a monochromatic objective and the need for achromatization, the chromatic focal shift measurement and fluorescence imaging were also performed on a monochromatic objective prototype previously described by Landau et al. [47].

4.4.1. Measuring the tilt and decenter of doublet lenses

Copies of lens 2 and lens 3 (Figure 4.3(b)) were fabricated and assembled to measure the tilt and decenter of the doublets. The doublet's tilt was measured with a NewView 5020 white light interferometer (Zygo Corp.). The doublet was placed on

a microscope slide with its tilt reduced to less than 0.007° by adjusting the tilt of the interferometer's stage (Figure 4.4(a)). Then the doublet's tilt was measured 5 times on each side. The average tilt was 0.093° with a standard deviation of 0.055°, indicating that the tilt is within tolerance. The decenter was measured using the integrated gage amplifier of an Optimum 2400 ultra-precision lathe (Precitech). One lens of the doublet was centered on the spindle of the machine within 2 μm using the integrated gage amplifier (Figure 4.4(b)). Then the runout of the second lens was measured. Any increase in runout corresponds to a decenter of half that value. This measurement was performed 5 times for each singlet. The average element decenter of the doublet was 6.1 μm with a standard deviation of 0.7 μm, again indicating that doublets can be built with acceptable deviations from nominal.
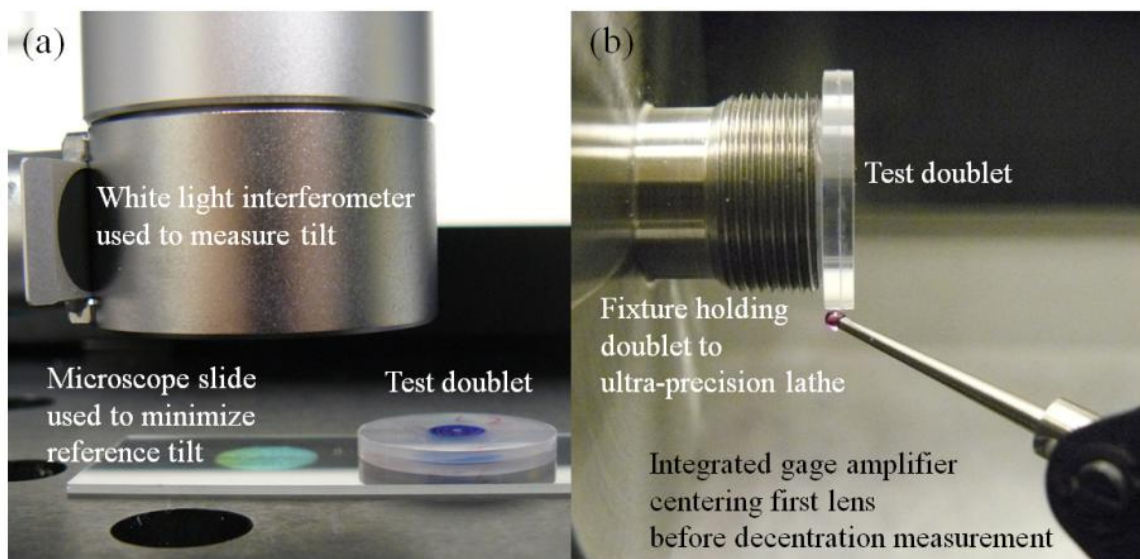

Figure 4.4. (a) Measuring tilt with a white light interferometer. The doublet's average tilt was 0.093° with a standard deviation of 0.055°. (b) Measuring decenter with an integrated gage amplifier. The doublet's average decenter was 6.1 μm with a standard deviation of 0.7 μm.

4.4.2. Measuring the performance of the achromatic objective

To measure the lateral, polychromatic resolution of the achromatic objective, an image of a 1951 USAF hi-resolution target (58-198, Edmund Optics Inc.) was relayed in reverse (placing the target in the image space of the achromatic objective). This setup causes the resolution to be limited by the achromatic objective's image space NA = 0.14. For NA0.14, the Rayleigh resolution limit in white light is 2.40 μm, or 417 lp/mm, assuming a central wavelength of 550 nm. The hi-resolution target has features up to 645 lp/mm, so the target can be used to assess the smallest features the objective can resolve. The custom objective was set up to relay an image through an Axio Observer. A1 inverted microscope (Carl Zeiss) under white light trans-illumination. The object is placed in image space and a 40X, NA0.75 water immersion commercial objective (Carl Zeiss) relays an image through the microscope to a CCD camera (Figure 4.5(a)). The results are seen in Figure 4.6(a) and Figure 4.6(b). Because the custom objective is designed for a curved object (acceptable for imaging thick tissue), there is some field curvature and loss of performance at the edge of the FOV while imaging flat objects. The qualitative performance of the system was determined by locating the smallest resolvable feature, in this case group 8, element 5, which is 406 lp/mm. This is close to the theoretical diffraction limit, 417 lp/mm and is similar to the monochromatic performance of the objective described by Landau et al. [47].
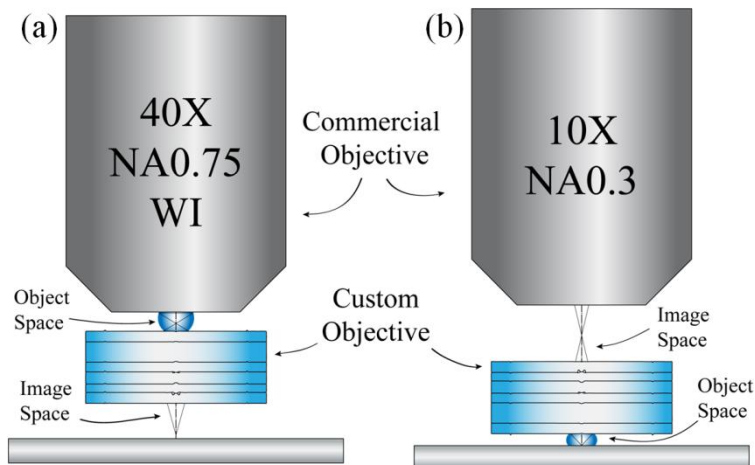
Figure 4.5. Custom achromatic objective and commercial objectives relaying images (a) in reverse and (b) as designed.

The achromatic objective's performance was further analyzed by measuring the SR via the slanted-edge method of calculating the MTF [50]. An edge object was placed in front of the system in water immersion and the image was relayed with a 10X, NA0.3 Plan-Neofluar objective (Carl Zeiss) (Figure 4.5(b)). A VariSpec liquid crystal tunable filter (LCTF) (Cambridge Research & Instrumentation, Inc.) filtered the light to match the four design wavelengths (452 nm, 515 nm, 575 nm, and 623 nm) with approximately 10 nm bandwidths. For each waveband, sixteen edges were inspected, eight near the center and eight near 50% of the FOV. Figure 4.6(c) shows a set of four measured edges from one corner of a square on the resolution target; the remaining twelve edges were obtained from the square's three other corners. An MTF curve was generated from each edge using the ISO 12233 standard [96]. The polychromatic MTF curve was created by averaging all 64 narrowband curves and is displayed in Figure 4.7(a). The Strehl ratio is 0.74 ± 0.05.
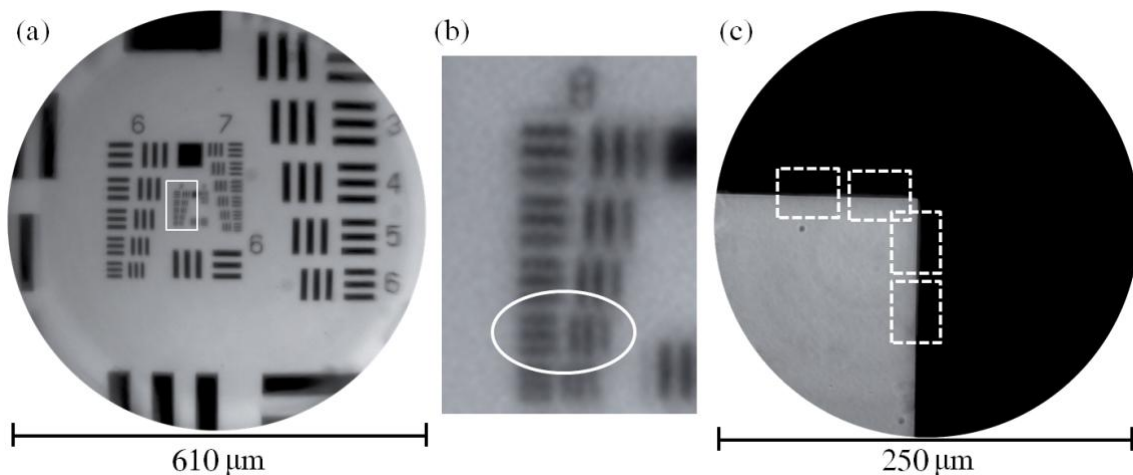
Figure 4.6. (a) The center of a hi-resolution 1951 USAF target illuminated with white light in transmission. The achromatic objective is operating in reverse, which means the resolution is limited by the image space NA=0.14. (b) The region of interest outlined in (a). The smallest resolvable feature is group 8, element 5, which has a spatial frequency of 406 lp/mm. The theoretical diffraction limit is 417 lp/mm. (c) Set of four edges measured with the slanted edge method to determine the achromatic objective's MTF and Strehl ratio.
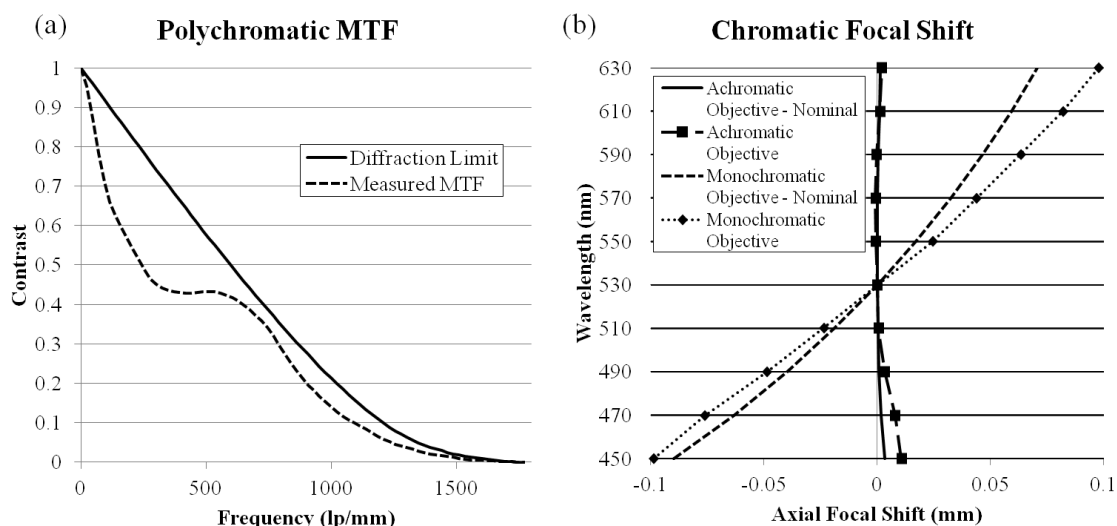
Figure 4.7. (a) Polychromatic MTF of the achromatic objective. (b) Chromatic focal shifts of the achromatic objective and the monochromatic objective.

The chromatic focal shifts of both the achromatic objective and the monochromatic objective described by Landau et al. [47] were measured using an MT25 precision length gauge (Heidenhain) to record the axial position of the stage.

The LCTF was set to 450 nm and the best focal plane was found. The LCTF's wavelength was increased by 20 nm and the new best focal plane was measured. This process was repeated until the wavelength reached 630 nm. The procedure was performed five times for each prototype objective, and the relative shifts were averaged to find the chromatic focal shifts of the objectives, which are plotted in Figure 4.7(b) alongside the nominal shifts. The achromatic objective successfully brings two wavelengths of light into focus simultaneously while the monochromatic objective does not. Also, although the measured shifts were larger than expected, the achromatic objective's 11.4 μm maximum focal shift is smaller than the diffraction-limited focal range of 22.0 μm. In contrast, the monochromatic objective's 196.4 μm shift is almost an order of magnitude greater than the diffraction-limited focal range. To the best of our knowledge, this is the first all plastic, achromatic microscope objective.

4.5. Imaging breast carcinoma cells with the achromatic objective

In vitro breast carcinoma cells from the 435S cell line were used for biological imaging with both prototype objectives. The cells were seeded on an 8-well microscope slide and stained with proflavine and cresyl violet. The proflavine, or 3,6-diaminoacridine hydrochloride (Sigma-Aldrich Co.), was prepared as a 0.025% weight volume solution in 1X phosphate buffered saline (PBS) (Sigma-Aldrich Co.), while the cresyl violet (Sigma-Aldrich Co.) was prepared as a 0.05%

weight volume solution in 1X PBS. Two hundred μL of each fluorescent dye solution were added to each well. The cells were stained for 5 minutes before the dye was removed. Each chamber was then washed with 500 μL of 1X PBS to remove excess dye.

The breast carcinoma cells were imaged with the monochromatic and achromatic objectives separately through the Imager.Z1 upright microscope (Carl Zeiss), as well as with an NA0.45 commercial objective (Carl Zeiss). Using a GFP filter set, proflavine was excited without exciting cresyl violet. The cells were brought into focus and an image was captured with the microscope's monochrome camera. Without adjusting the position of the stage, cresyl violet was imaged through a Texas Red filter set. The separate proflavine and cresyl violet images were recombined into single, pseudocolor images (Figure 4.8). The Zeiss objective (Figure 4.8, top row) demonstrates that proflavine preferentially stains nuclei while cresyl violet is concentrated in the cytoplasm. Both the monochromatic and achromatic objectives clearly showed proflavine staining the nucleus (Figure 4.8, left column). However, the cytoplasm is blurry at the red wavelength when the cells are imaged with the monochromatic objective (Figure 4.8, center).
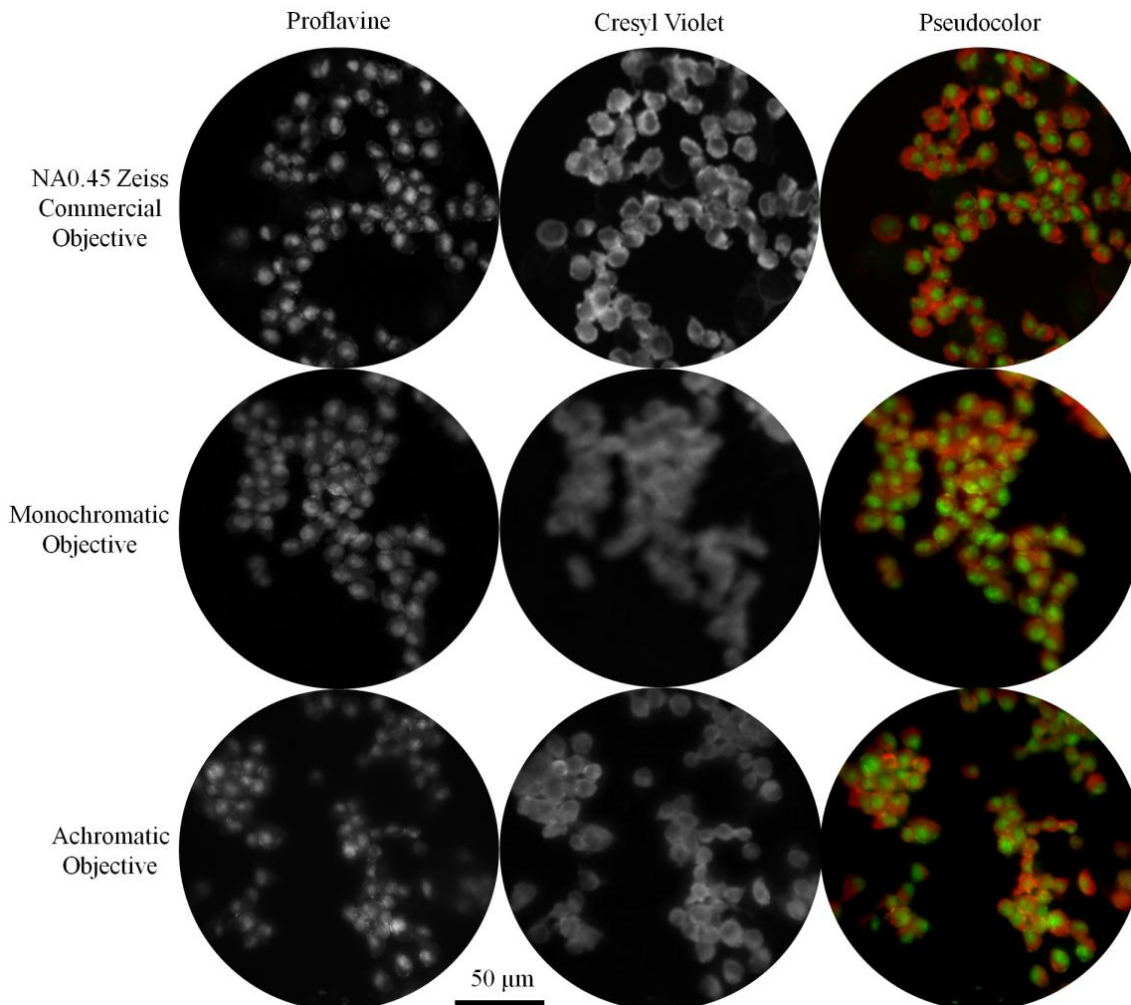
Figure 4.8. Images of cells from the 435S breast carcinoma cell line stained with proflavine and cresyl violet. The commercial objective and the prototype achromatic objective provide high resolution images for proflavine and cresyl violet simultaneously. In contrast, cresyl violet is out of focus with the monochromatic objective.

The cells were also imaged using structured illumination via the ApoTome attachment to the Imager.Z1 microscope using the procedure described above. Because the cells were already a monolayer, there was only a modest contrast improvement; when optically sectioning thick tissue, the reduction in background fluorescence will create a greater increase in contrast. The commercial objective and achromatic objective again provided high quality images for both fluorescent dyes,

while the monochromatic objective lost performance when imaging cresyl violet (Figure 4.9). There is also a loss of intensity due to the structured illumination grid pattern being focused at a different depth. These effects are due to chromatic aberration; the focal planes for the excitation and emission wavelengths, which are conjugate for the commercial and achromatic objectives, are separated with the monochromatic objective.
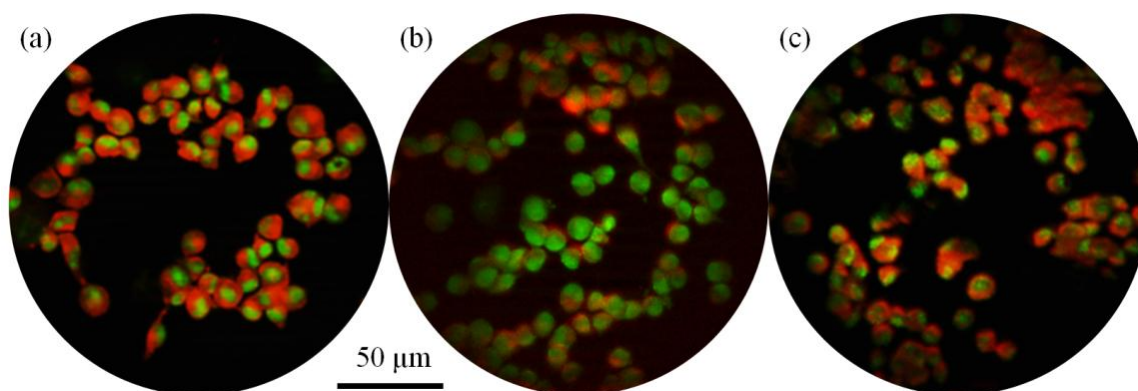
Figure 4.9. Structured illumination images of cells from the 435S breast carcinoma cell line stained with proflavine and cresyl violet. Structured illumination was created with the ApoTome and the cells were imaged with (a) the NA0.45 commercial objective, (b) the monochromatic objective, and (c) the achromatic objective.

4.6. Discussion

The first all-plastic, achromatic microscope objective has been designed, toleranced, fabricated, and tested. The NA0.4 objective is an alternative to GRIN lenses, which suffer from significant chromatic aberration as well as performance loss across the FOV. The objective is achromatized and maintains its performance across the designed 250 μm FOV, achieving a Strehl ratio of 0.74 ± 0.05 while holding the optical surfaces' clear apertures to 0.9 mm. Wide-field fluorescence

imaging and optical sectioning via structured illumination are performed through the achromatic objective. Background reduction, via optical sectioning or another method, is critical when fluorescently imaging dense samples like breast tissue; without such methods, high levels of background create low contrast images. The achromatic objective permits using multiple dyes simultaneously.

4.7. Acknowledgements

<div align="right">

Chapter 5

</div>

Fiber bundle endomicroscope with structured illumination

Chapter 3 and Chapter 4 showed the development of endomicroscope objectives which can be used to improve the lateral resolution of optical biopsy systems. However, as explained in Section 2.4, the HRME itself must be redesigned in order to improve the axial response of the optical biopsy system. This chapter demonstrates the improvement in image contrast for thick breast tissue provided by optical sectioning compared to conventional fluorescence imaging. A structured illumination HRME (SI-HRME) reduces background light from out of focus fluorescent signal, improving contrast compared to the conventional HRME. Excised breast tissue was imaged with both the HRME and SI-HRME and compared to images obtained with a commercial, benchtop confocal microscope and via histopathology, the gold standard for breast cancer diagnosis.

5.1. Background

The HRME has successfully imaged tissue from the oral cavity [103], the esophagus [104], and the cervix [105] using a coherent fiber bundle approximately 1 mm wide. However, the thick, dense tissue of the breast generates significant amounts of out of focus background light during fluorescence microscopy, reducing system performance. Presented below is an HRME that utilizes structured illumination to perform optical sectioning, which improves the contrast of images by reducing out of focus light.

Structured illumination is achieved by projecting a translatable grid pattern onto the proximal face of the fiber bundle, similar to Bozinovic et al. [26]. By shifting the grid using a motorized stage, three intensity modulated images are captured, each with the grid pattern 1/3 out of phase from the other two. The modulated images are recombined to form a single, optically sectioned image. The SI-HRME can be a tool for clinicians to improve the detection of breast cancer and provides a step forward for *in vivo* microscopy.

5.2. Building and testing the SI-HRME

The SI-HRME is illustrated in Figure 5.1. The excitation light is generated by a blue LED (M455L2, Thorlabs) at 455 nm and passes through a 10 lp/mm grid (59-545, Edmund Optics Inc.) on a motorized stage (T-LS28E, Zaber Technologies Inc.). An image of the grid is focused onto the proximal face of the fiber bundle (FTIFHR800S, F & T Fibers and Technology GmbH) with an NA0.3 commercial

objective (RMS10X-PF, Thorlabs). The grid's image is relayed through the fiber bundle and onto the sample. The modulated emission light returns through the system and is imaged onto a CCD camera (GRAS-14S5M, Point Grey Research, Inc.) where it is reconstructed into an optically sectioned image. The system is intended to image proflavine, a fluorescent dye with peak excitation and emission wavelengths of 452 nm and 515 nm, respectively. Proflavine preferentially stains cell nuclei, allowing visualization of the size and shape of each nucleus.
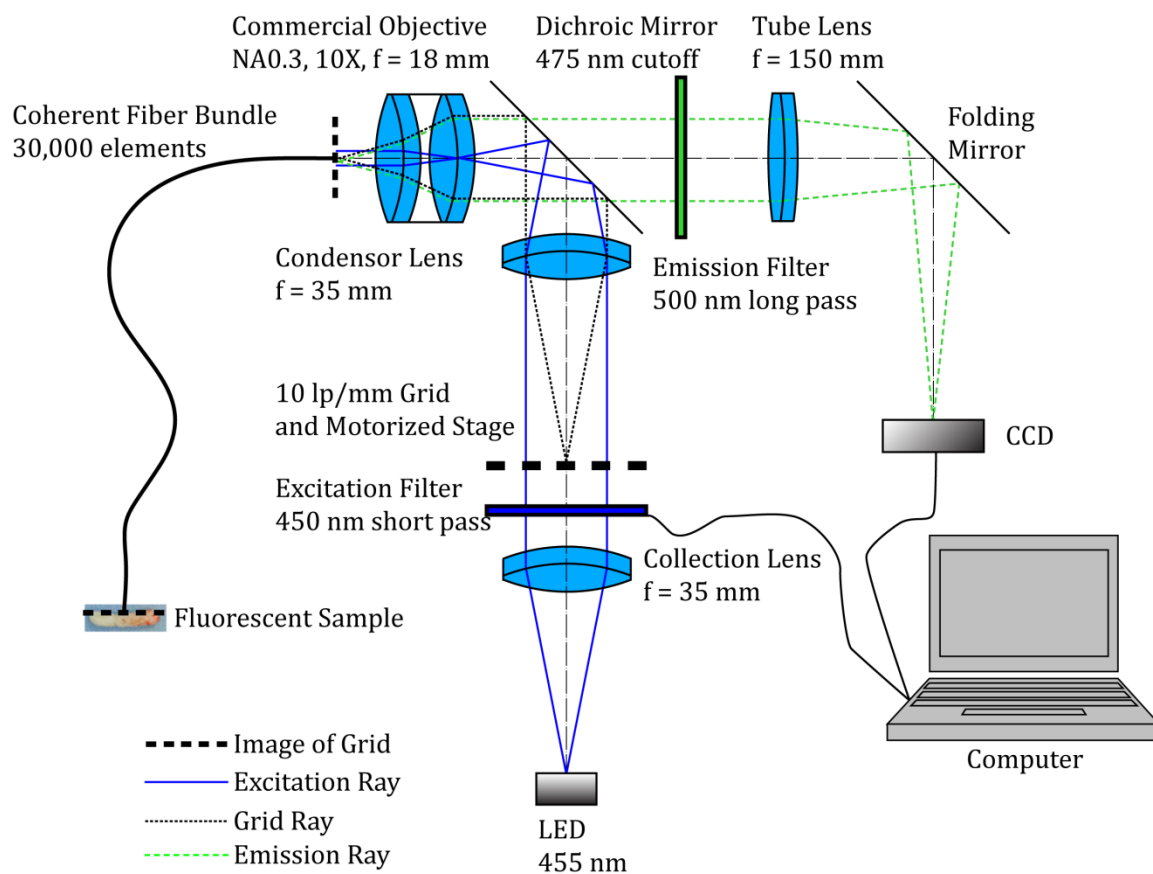
Figure 5.1. SI-HRME design layout.

When the grid is outside the path of the excitation light, the system is functionally identical to a conventional HRME. The SI-HRME can take advantage of

this by using the motorized stage to translate the grid out of the light path; this allows conventional HRME images to be compared to SI-HRME images with identical FOVs without the need for a separate imaging system.

Before imaging breast tissue, the SI-HRME was tested on non-biological targets. The resolution of the system was measured by imaging a 1951 USAF resolution target (38-256, Edmund Optics Inc.) with a fluorescent background. The smallest features the system could resolve were those of group 7, element 1, corresponding to a frequency of 128 lp/mm, or 7.8 μm resolution (Figure 5.2(a)). This result is expected because the core to core spacing of the individual fibers is approximately 4 μm, limiting the resolution to twice that value by the Nyquist sampling theorem. Note that, for Figure 5.2(a), the grid was translated out of the excitation light's path, allowing conventional fluorescence to occur.
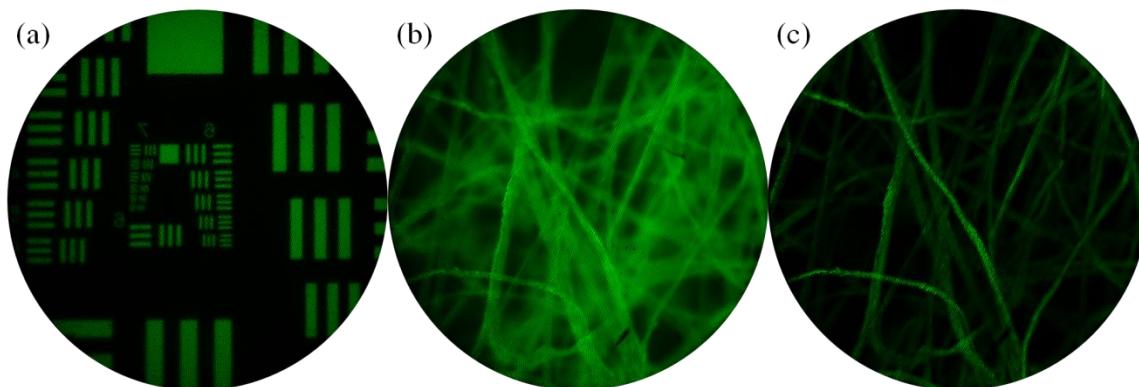
Figure 5.2. Images through the SI-HRME: (a) Resolution target, (b) fluorescent lens paper via conventional fluorescence, and (c) fluorescent lens paper via optical sectioning.

The ability of the system to perform optical sectioning was demonstrated on fluorescent lens paper. Figure 5.2(b) shows the lens paper which was imaged

without structured illumination while Figure 5.2(c) shows the same FOV which has been optically sectioned via structured illumination. Note the improvement in contrast due to the reduced signal from out of focus fibers.

5.3. Images of *ex vivo* breast biopsies captured with the SI-HRME and other techniques

5.3.1. Breast biopsy imaging procedure

Surgical breast resections were obtained through collaborators at MD Anderson Cancer Center. The tissue samples were obtained following the Rice protocol "A Pilot Study for the Optical Imaging of Breast Cancer in Breast Tissue and Lymph Nodes," Protocol Number 08-95E. At MD Anderson, the Protocol Number is LAB07-0700. The breast tissue was obtained via excisional biopsy and later used for histological diagnosis. Each sample was stained for several minutes with 0.01% proflavine solution before being rinsed with PBS (Sigma-Adrich Co.) and imaged with the Vivascope 2500 (Caliber Imaging and Diagnostics Inc.), a confocal microscope which scans the sample across the objective's field of view and creates a mosaic image. Once imaging with the confocal microscope was complete, regions of interest from the *ex vivo* sample were imaged with the SI-HRME, both with and without optical sectioning (Figure 5.3).
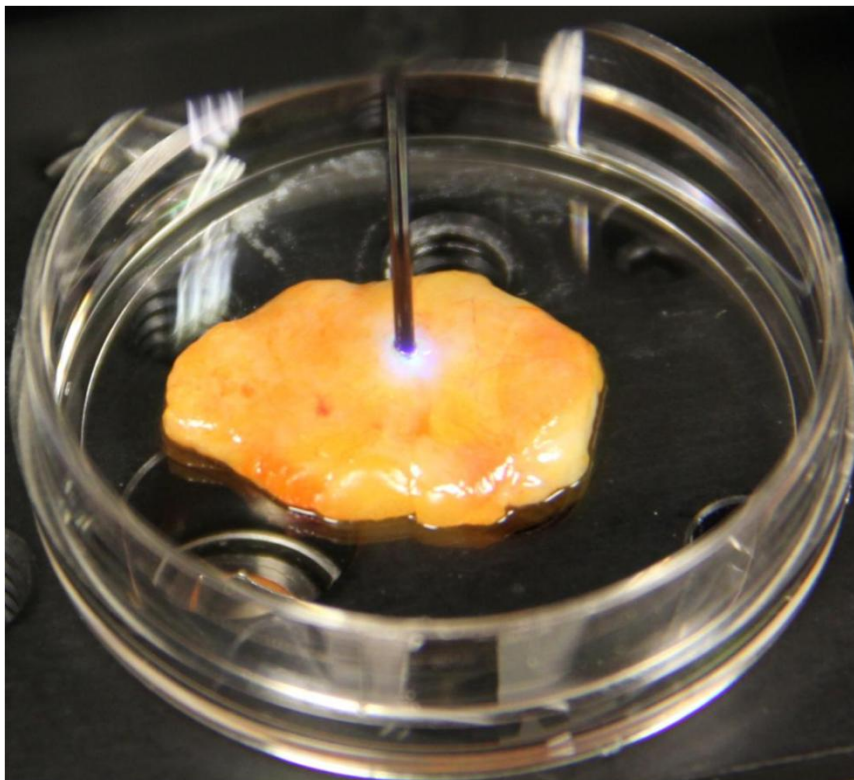
Figure 5.3. Fiber bundle from the SI-HRME imaging an excised breast tissue sample which has been stained with proflavine.

To demonstrate the ability of the SI-HRME to improve contrast and provide images which are closer in quality to images from both the commercial confocal microscope and conventional H&E staining, multiple tissue types were imaged. Each figure below contains four images via different imaging modalities: conventional HRME, SI-HRME, benchtop confocal microscope, and conventional light microscope. Each figure shows images which were obtained from the same tissue sample and attempt to match the FOV for all four imaging modalities. The same region of interest is guaranteed for the conventional HRME and the SI-HRME because the fiber bundle is held in place at a given region of interest while the grid is translated into or out of the path of the excitation light. However, minor morphological changes due to tissue compression and sample preparation lead to some uncertainty with

regards to the FOV for images from the confocal and conventional microscopes. Even when the FOV is not precisely matched, the selected features provide a viable comparison between the various methods.

5.3.2. Comparison of microscopic breast tissue images

Figure 5.4 shows a lobule imaged via the four modalities. Lobules are important features to characterize because they are the site of lobular carcinoma *in situ* [2], an abnormality which indicates an increased risk of breast cancer later in life. Figure 5.4(a) shows a normal (non-diseased) breast lobule imaged via the conventional HRME. The image has low contrast due to high levels of background light. The contribution from the background is significantly reduced in Figure 5.4(b) and Figure 5.4(c) due to the optical sectioning provided by structured illumination and confocal microscopy, respectively. Figure 5.4(d) shows the corresponding histopathology created by staining the tissue with H&E and imaging a thin tissue slice under a conventional light microscope. Notice the architectural similarities between the fluorescence images and the histological sample, despite the differences in both staining agents and imaging methods. This supports fluorescence imaging in general and optical biopsy in particular as viable methods of diagnosing cancer.
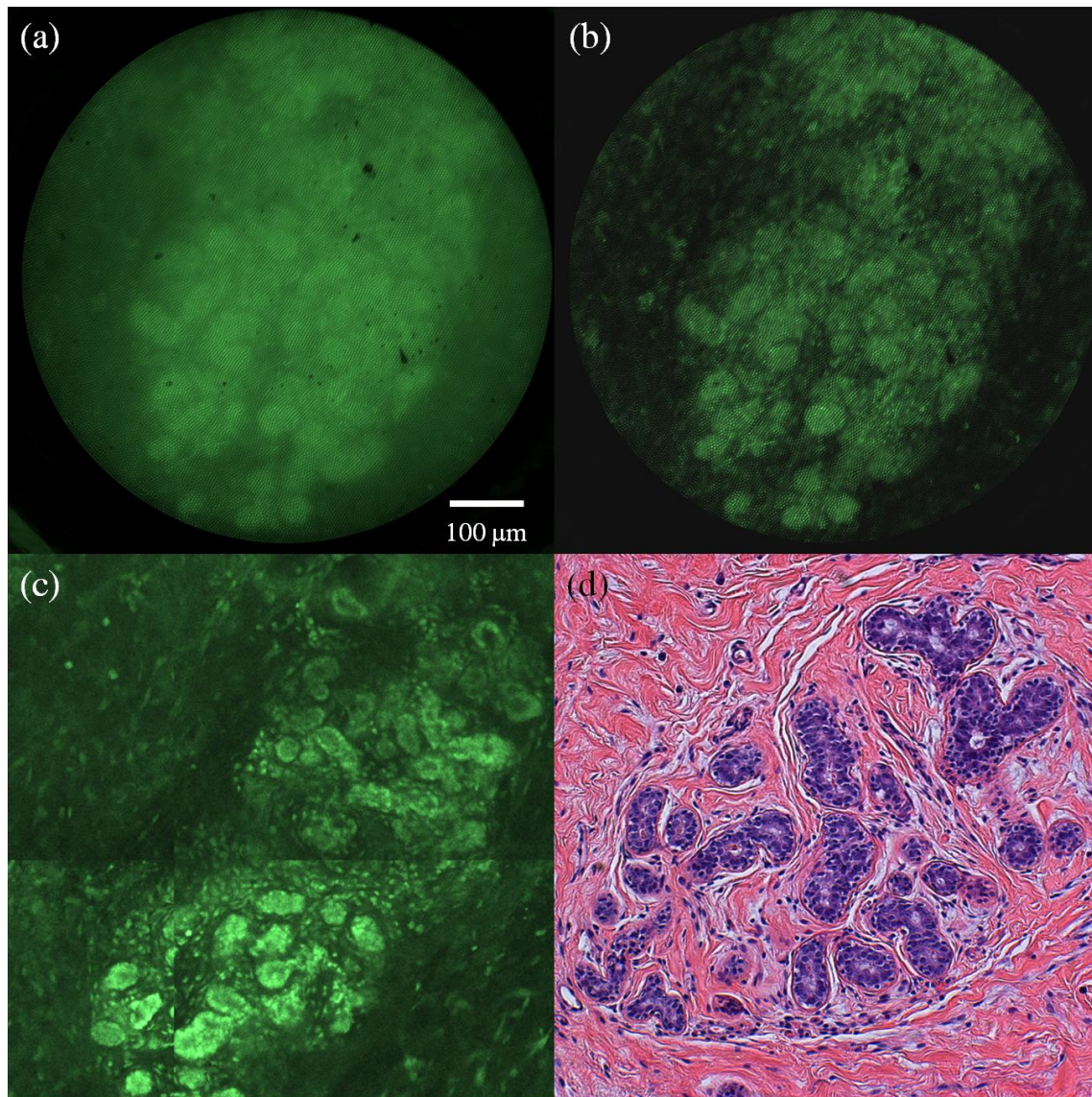
Figure 5.4. Normal breast lobule from a sample containing tumor via (a) the conventional HRME, (b) the SI-HRME, (c) the Vivascope 2500, and (d) conventional histology. Confocal and histology images courtesy of Jessica Dobbs.

The more common route for breast cancer to develop is via ductal carcinoma *in situ* [2], making ducts a crucial feature to image. Figure 5.5 shows a duct from a normal tissue sample imaged with the four modalities. Note how much more difficult the duct (the vertical feature on the right side of each image) is to see via the conventional HRME.

Figure 5.5. Duct from a normal breast tissue sample via (a) the conventional HRME, (b) the SI-HRME, (c) the Vivascope 2500, and (d) conventional histology. Confocal and histology images courtesy of Jessica Dobbs.

It is also important to be able to distinguish blood vessels from ducts, which have a similar appearance. Figure 5.6 illustrates a blood vessel located in normal, fatty tissue.

Figure 5.6. Blood vessel from a normal breast tissue sample via (a) the conventional HRME, (b) the SI-HRME, (c) the Vivascope 2500, and (d) conventional histology. Confocal and histology images courtesy of Jessica Dobbs.

The optical biopsy system must be able to distinguish healthy tissue from tissue which is cancerous or otherwise unhealthy. Figure 5.7 illustrates normal, fatty tissue with regularly sized and spaced nuclei. There are two important points to note for this figure. First, the conventional HRME performance is comparable to the other imaging modalities in this type of breast tissue because adipocytes take up

very little proflavine except for what stains the nuclei. This means there is little need for optical sectioning with this tissue type. Second, the fat cells in the histology image (Figure 5.7(d)) have been damaged, possibly during tissue slicing, causing many to undergo cell lysis and appear different from the fluorescence images.
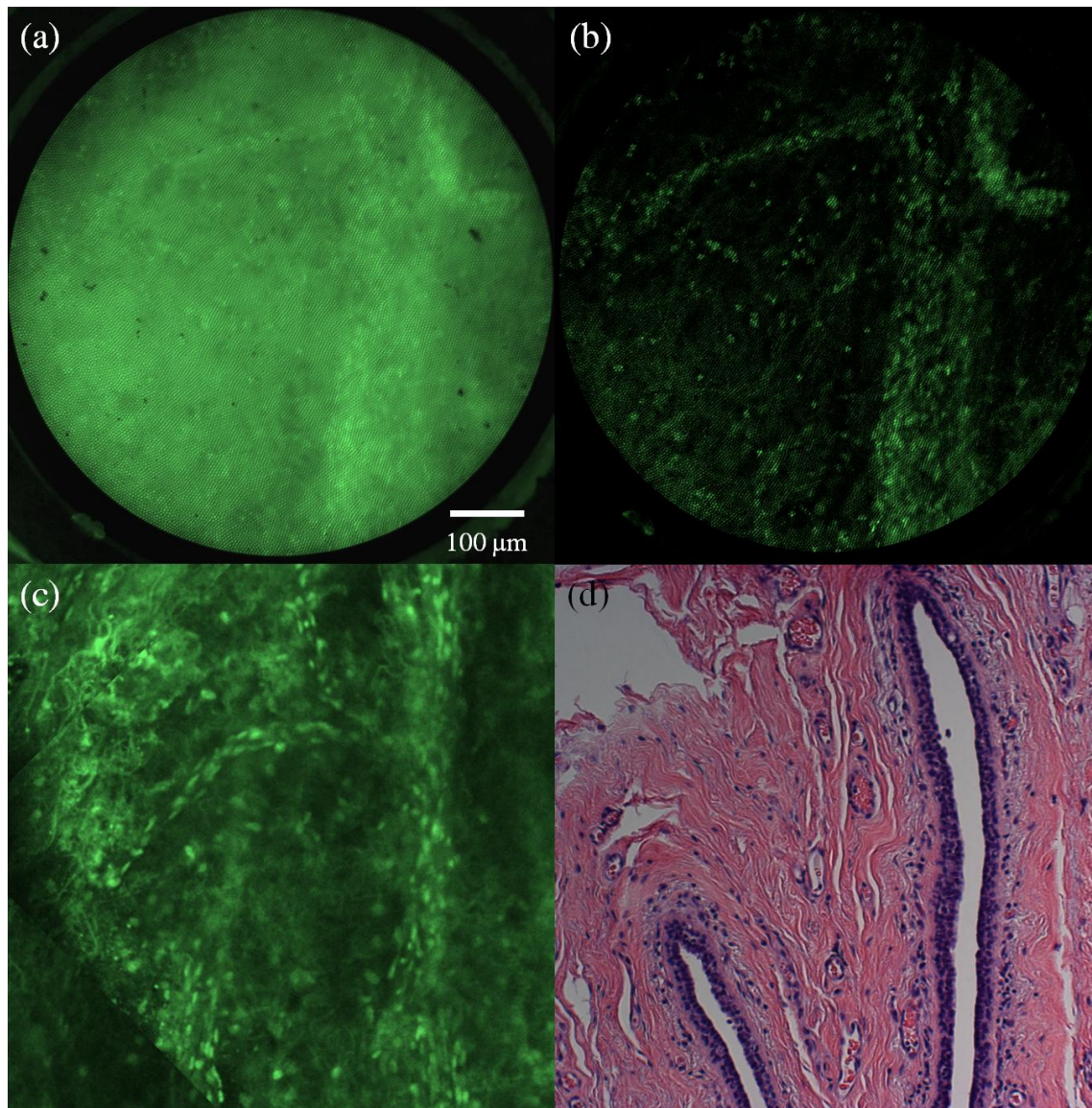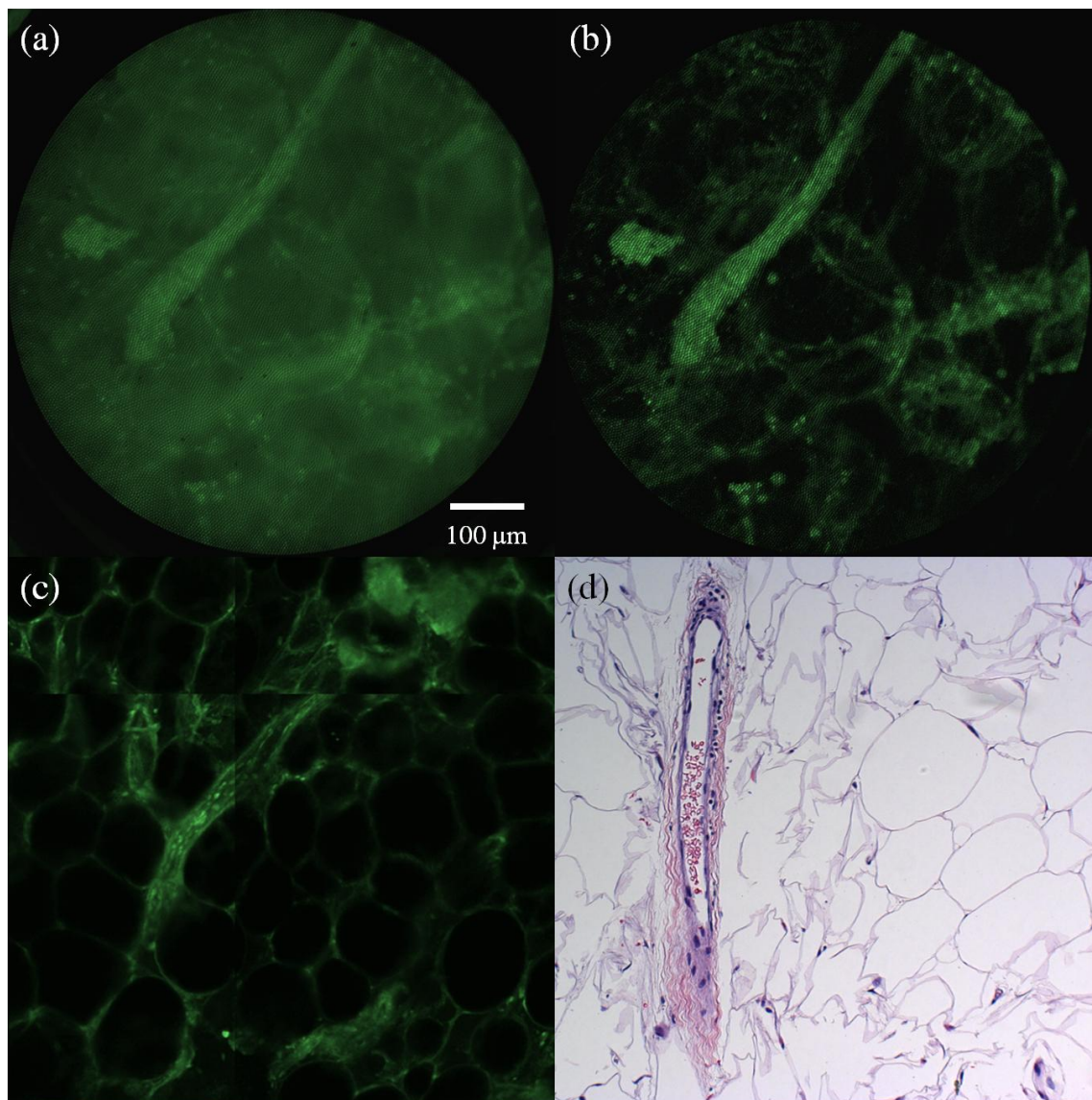

Figure 5.7. Normal, fatty breast tissue via (a) the conventional HRME, (b) the SI-HRME, (c) the Vivascope 2500, and (d) conventional histology. Confocal and histology images courtesy of Jessica Dobbs.

Perhaps most importantly, the SI-HRME must be able to identify cancerous tissue. An invasive tumor is shown in Figure 5.8. Again, the conventional HRME (Figure 5.8(a)) has low contrast compared to the other imaging modalities due to high levels of background light; this is expected because cancer has large, crowded nuclei which lead to high concentrations of fluorescent dye. Both benchtop confocal and SI-HRME eliminate most of the out of focus light, providing high contrast images and allowing better visualization of the subcellular architecture.

5.4. Discussion

The results demonstrate the improvement over the HRME for breast tissue images with proflavine when optical sectioning is performed, particularly with the SI-HRME. In the next chapter, this technique is used in conjunction with a custom, integrated objective at the distal tip of the fiber bundle to increase lateral resolution.

5.5. Acknowledgements

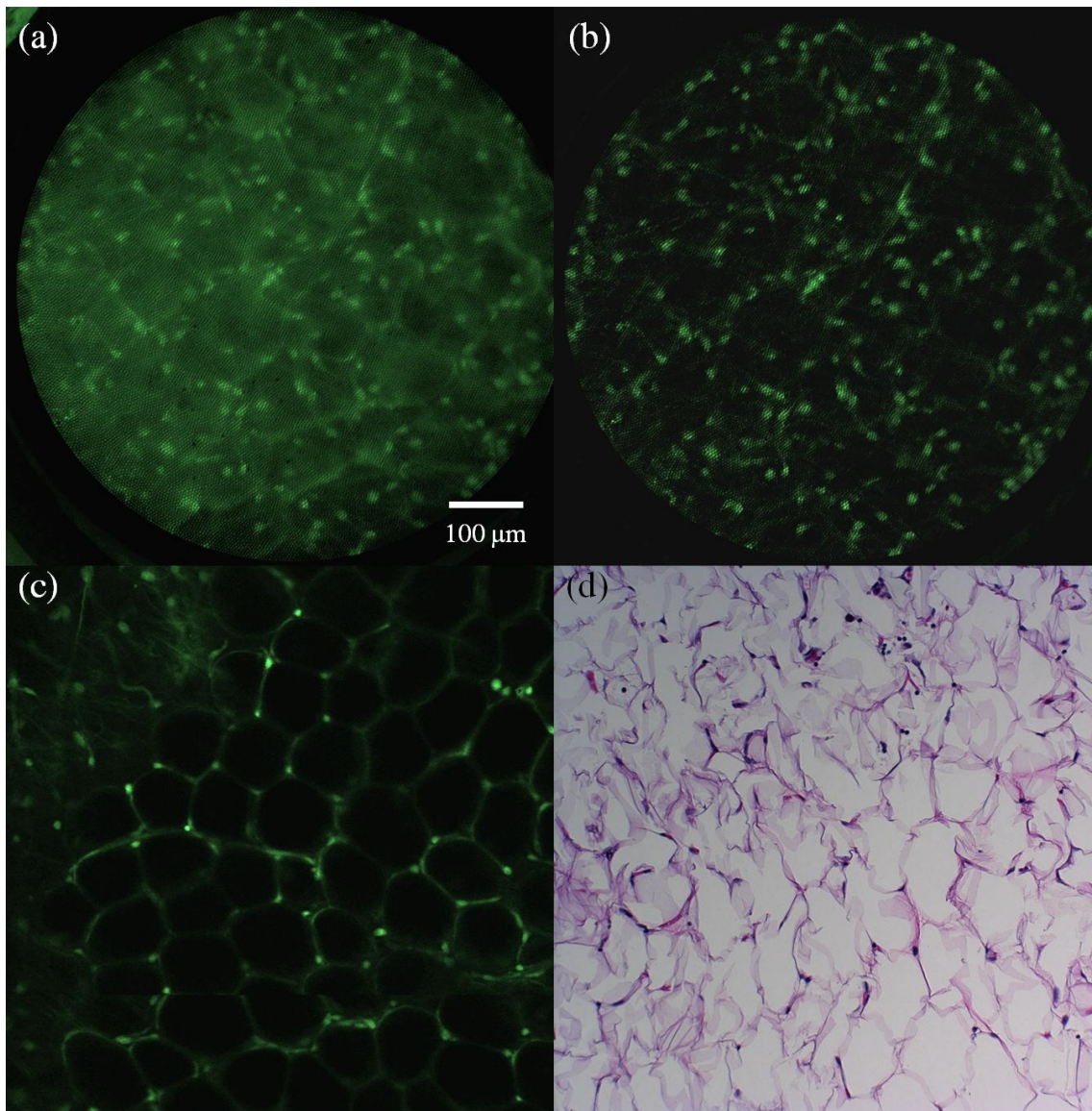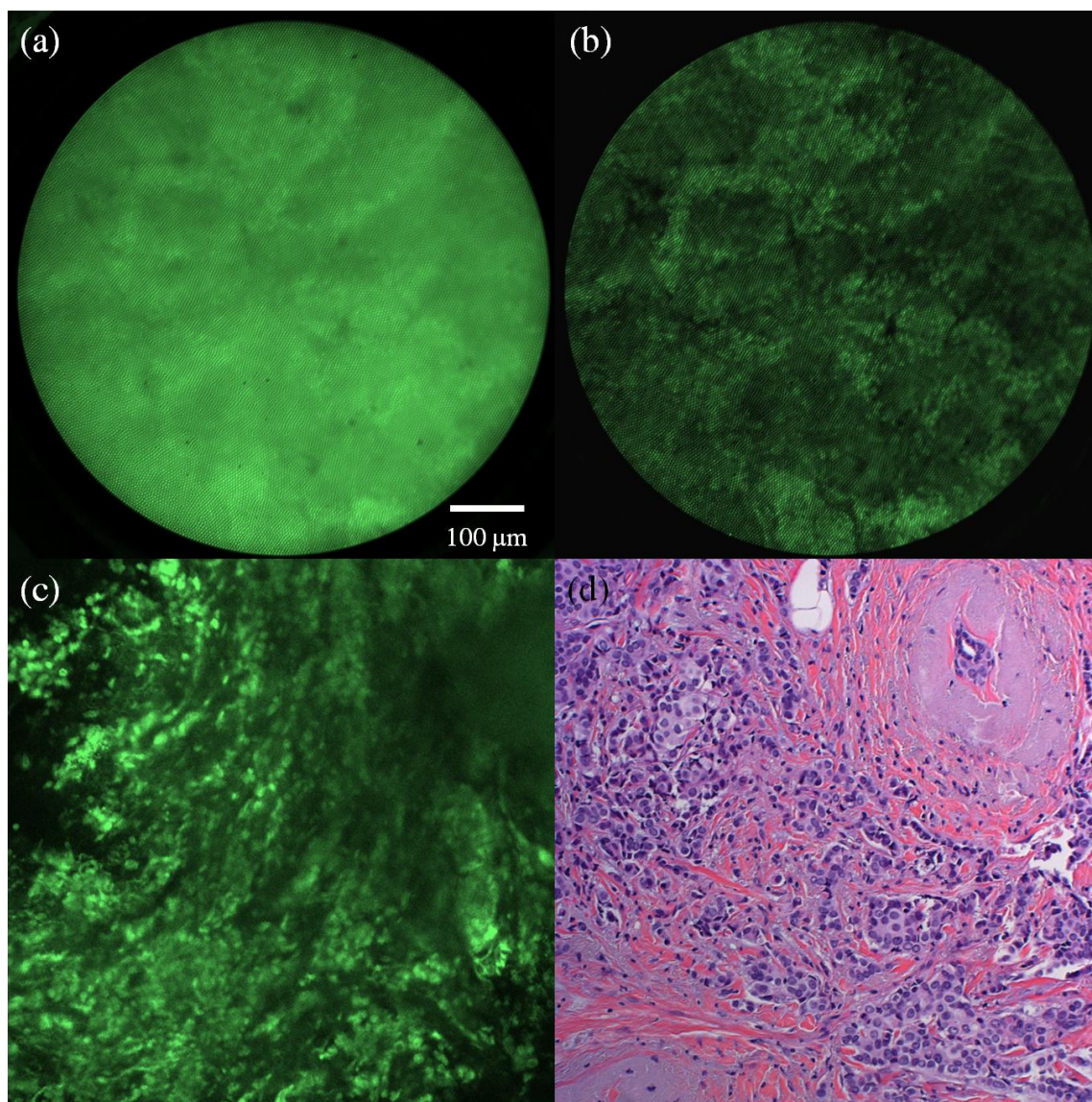Figure 5.8. Invasive tumor from a sample containing invasive ductal carcinoma via (a) the conventional HRME, (b) the SI-HRME, (c) the Vivascope 2500, and (d) conventional histology. Confocal and histology images courtesy of Jessica Dobbs.

Chapter 6

Endomicroscope with an integrated achromatic objective to perform optical biopsies of breast tissue

Using the technology developed Chapter 3 and Chapter 4, a new achromatic, ultra-slim objective was designed and fabricated. The OD of the plastic lenses and their built in alignment features is 2.1 mm, the same size as a large core biopsy needle. The NA0.55 objective has a 360 μm FOV and provides chromatic correction for both the excitation and emission wavelengths of proflavine (452 nm and 515 nm, respectively). The lateral resolution and chromatic focal shift were measured and *in vitro* images of breast carcinoma cells stained with proflavine were captured through the objective alone.

The objective was then integrated onto the distal tip of a fiber bundle connected to the SI-HRME described in Chapter 5. The achromatic objective magnifies the object onto the fiber bundle to increase lateral resolution while optical sectioning is achieved via structured illumination. The optical biopsy system resolves smaller features than the current HRME and rejects out of focus light of thick samples, improving image contrast. The system was evaluated on multiple fluorescent samples, including *ex vivo* mouse tissue stained with proflavine.

6.1. Background

Optical biopsies provide an alternative to conventional biopsies by providing microscopic images of *in vivo* tissue in real time. Optical biopsies do not cause tissue-removal-associated trauma to the patient such as that caused by core needle biopsies and incisional biopsies [7]. Also, unlike fine needle aspiration, optical biopsies allow the region of interest to be seen in its native environment, which improves the sensitivity and specificity of the diagnosis [5]. Using an optical biopsy to study suspicious tissue can augment the diagnosis of suspicious lesions by providing *in vivo* information and can reduce the total number of excisional biopsies performed.

This chapter presents an SI-HRME that utilizes structured illumination to perform optical sectioning, which reduces out of focus light, and that incorporates an achromatic, ultra-slim objective at the distal tip, improving resolution. This objective magnifies an image of the tissue onto the image guide, increasing sampling

and thus improving lateral resolution. Unlike GRIN lenses, our objective is achromatized within the visible spectrum and maintains high performance across the FOV.

6.2. Designing the SI-HRME and achromatic, ultra-slim objective

Building the optical biopsy system was divided into two aims: achieving optical sectioning via structured illumination with the HRME; and designing, fabricating, and characterizing an achromatic objective no wider than a biopsy needle. Once both components were ready, the achromatic objective was attached to the distal tip of the structured illumination HRME (SI-HRME) to characterize the performance of the integrated system and perform initial biological imaging.

6.2.1. Specifications for the SI-HRME and achromatic, ultra-slim objective

Figure 6.1 displays the design of the optical biopsy system; except for the addition of the integrated achromatic objective, it is identical to the system in Figure 5.1. The design specifications for the achromatic objective are listed in Table 6.1. The requirements are similar to those described in Chapter 3. The current objective has a larger NA and a wider FOV which was accomplished by relaxing the maximum clear aperture requirement.
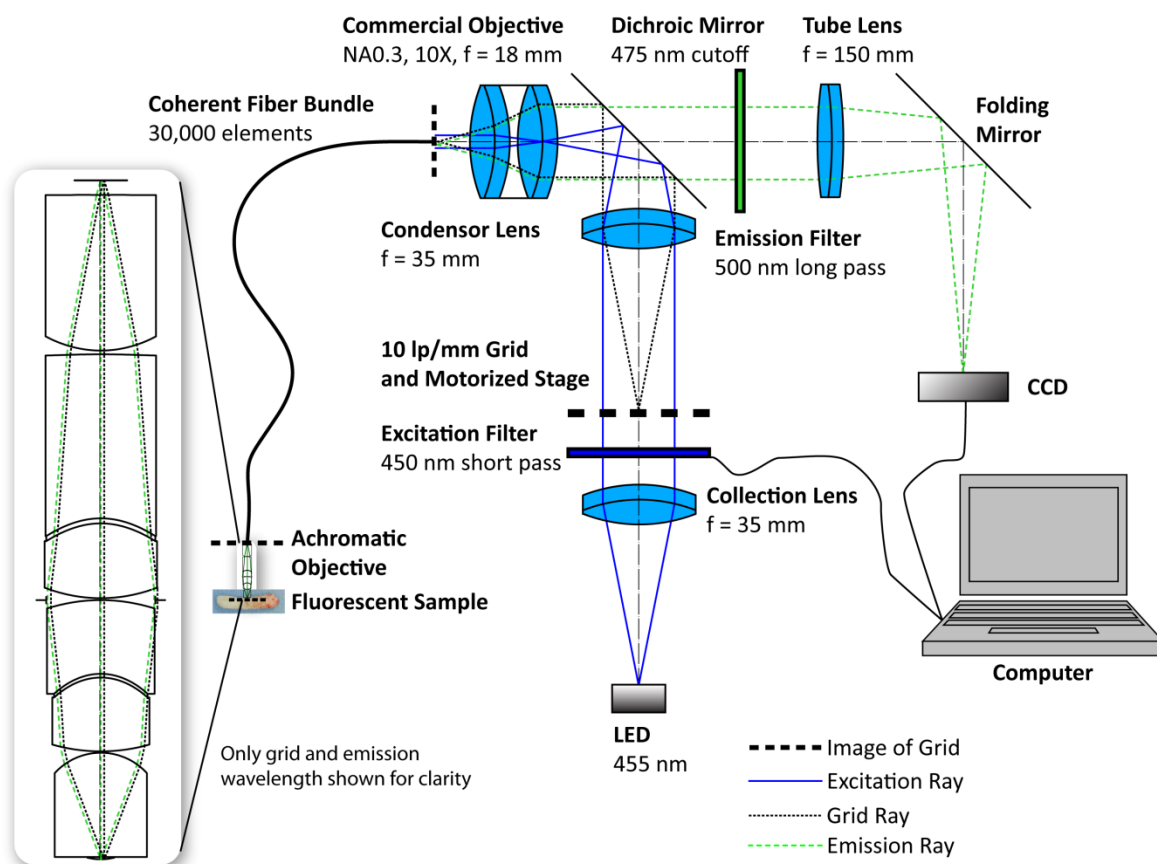
Figure 6.1. Structured illumination HRME design layout with the integrated achromatic objective.

Table 6.1. Design specifications of the NA0.55 achromatic, ultra-slim objective

Object Space NA[a]	0.55
Image Space NA	0.275
Field of View	360 μm
Clear Aperture	1.5 mm
Magnification	-2
Working Distance[a]	15 μm
Wavelength Range	452-623 nm

[a]Object space is intended for water immersion.

The object space NA0.55 means the objective will have a point spread function (PSF) size of 1.14 μm at the 515 nm emission peak of proflavine. In image space, the PSF size is 2.28 μm, which is still well beneath the 4 μm core to core spacing of the individual fibers in the fiber bundle. This sampling frequency, combined with the -2X magnification, means the lateral resolution of the optical biopsy system will be approximately 4 μm. A 360 μm FOV is matched onto the 720 μm active diameter of the image guide by the -2X magnification. The short 15 μm working distance allows the objective to image tissue in contact. A wavelength range from 452 nm to 623 nm allows the achromatic objective to work with proflavine, and potentially cresyl violet as well. Cresyl violet is a fluorescent dye which has excitation and emission peaks at 575 nm and 623 nm, respectively; in the future, it can provide complimentary information to proflavine, as it inherently targets the cytoplasm, outside of the nucleus.

An objective meeting the requirements in Table 6.1 was designed in Zemax. The layout of the design is displayed in Figure 6.2. The objective is composed of six plastic lenses. The reasons for using plastic have been thoroughly described elsewhere [79,101,106] and include low autofluorescence for the design wavelengths, high transmission, and ease of fabricating aspheres, simplifying the design process. Zeonex E48R and PMMA are both crown-like plastics while polystyrene behaves optically like a flint. Zeonex E48R also has very low water absorption, which is why it was selected to be in contact with tissue. Lenses 2 and 3 form an achromatic doublet of PMMA and polystyrene with the optical adhesive NOA61 acting as the cement; lenses 4 and 5 do the same.
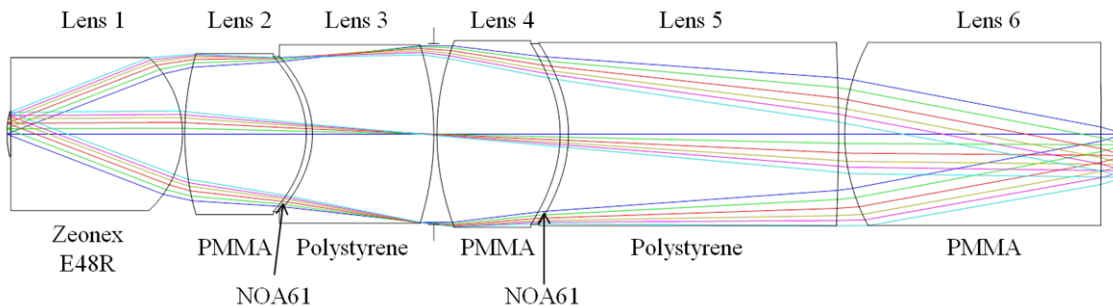
Figure 6.2. Achromatic, ultra-slim objective design.

6.2.1. Nominal and expected performance of the achromatic, ultra-slim objective

The nominal performance of the objective is shown in Figure 6.3. The MTF in Figure 6.3(a) shows that the objective maintains diffraction-limited performance across the FOV. It accomplishes this in part by assuming a curved object; this is permissible because the intended sample is breast tissue and the sag of the curved object is the approximate thickness of a layer of cells. The chromatic focal shift plotted in Figure 6.3(b) confirms that the objective is achromatic. Also, the 6.0 μm diffraction-limited range is larger than the 4.0 μm maximum chromatic focal shift.
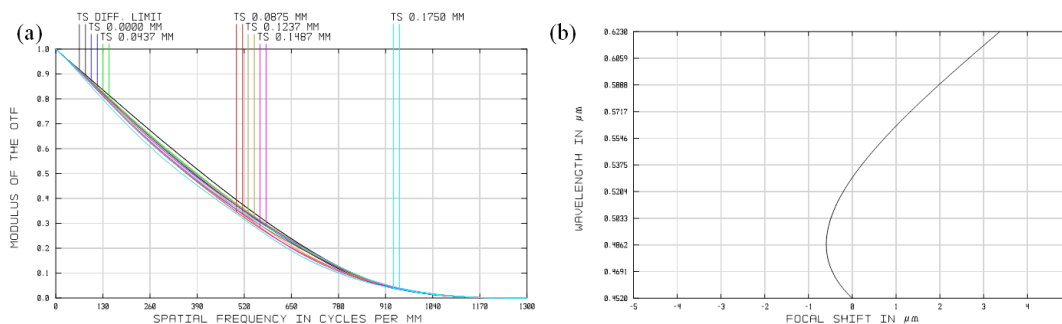
Figure 6.3. (a) Nominal MTF of the objective. (b) Nominal chromatic focal shift of the objective.

The design was thoroughly toleranced in Zemax. The tolerances listed in Table 6.2 were estimated based on in-house fabrication capabilities of an ultra-precision lathe. The lenses were formed via SPDT. For injection molding, typically used to mass produce plastic lenses, the tolerances are considered commercial or state-of-the-art [81].

Table 6.2. Tolerance values for the NA0.55 achromatic, ultra-slim objective

Tolerand	Value
Radius of curvature (%)	±1
Thickness (μm)	±20
Element decenter (μm)	±10
Element tilt (°)	±0.15
Doublet decenter (μm)	±15
Doublet tilt (°)	±0.2
Surface irregularity (fringes)	±1
Index (%)	±1
Abbe Number (%)	±1

6.3. Fabrication

Because the plastic lenses were fabricated via SPDT, the optical surfaces and alignment features were produced simultaneously, allowing tight manufacturing tolerances to be maintained [79,106]. A CAD model based on the optical design was made in SolidWorks (Dassault Systèmes SolidWorks Corp.) (Figure 6.4(a) and Figure 6.4(b)).

The circular ridges and V grooves visible at the edges of Figure 6.4(b) allow the lenses to be assembled with a zero alignment technique. The alignment features uniquely define the position of the lenses laterally and axially, allowing them to be stacked one atop the other and glued in place. To create the doublet lenses, a small drop of NOA61 is added to the concave optical surface before the two singlets are stacked. Once both lenses are in place, the adhesive is cured through UV exposure. The remaining lenses are stacked without adding adhesive. Once the alignment features are mated, the lenses are held in place and a small amount of cyanoacrylate is added to the outer edge of the alignment features and allowed to set. This procedure creates a strong, water-tight bond.

To integrate the objective and the fiber bundle, a custom "integrator" was also designed in SolidWorks and is shown mated with the achromatic objective in Figure 6.4(c). The integrator is a hollow, optomechanical part which was fabricated in plastic with a 3D printer (Pro Jet SD 3000, 3D Systems, Inc.) and has the same outer diameter as the achromatic objective. The inner diameter matches the diameter of the fiber bundle. A V groove, matching those in Figure 6.4(b), was cut into the distal face via SPDT, allowing the achromatic objective to be attached to the integrator using cyanoacrylate as described. To position the fiber bundle face at the image plane of the achromatic objective, the fiber bundle was translated along the optical axis while the achromatic objective imaged a resolution target; at the best focal position, the integrator was set in place with epoxy, creating an integrated imaging system.
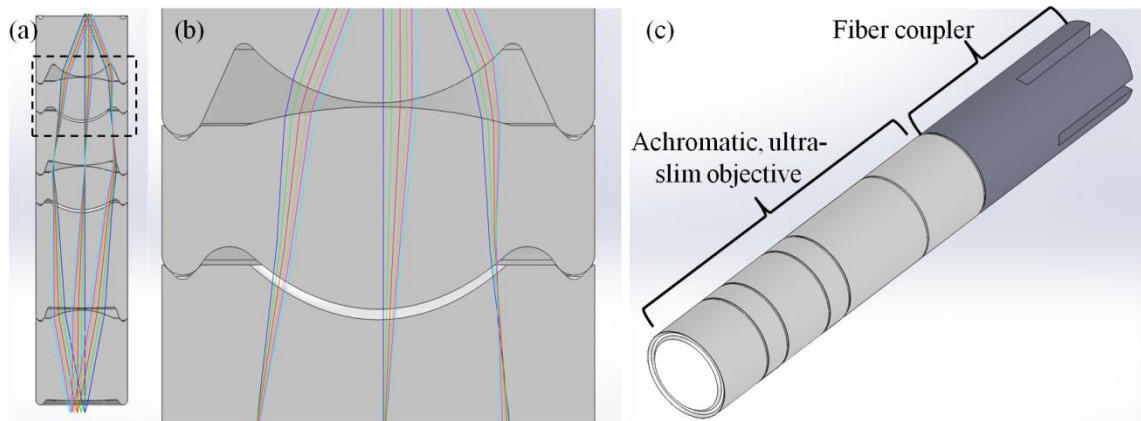
Figure 6.4. (a) SolidWorks cutaway of the achromatic objective with built-in alignment features. (b) Insert of (a). The alignment features define the position of the lenses. (c) SolidWorks model of the achromatic objective and the integrator used to attach the objective to fiber bundle.

6.3.1. Measuring the tilt and decenter of ultra-slim doublet lenses

Before building a complete objective, five sample doublets were made to validate the custom alignment features' abilities to create systems which behave within the given tolerances. Each doublet was fabricated as described above, except all of the optical surfaces were flat to facilitate measuring tilt and decenter. To measure the tilt, each doublet was placed on a microscope slide beneath a NewView 5020 white light interferometer (Zygo Corp.) after the tilt of the stage was reduced to less than 0.01° (Figure 6.5(a)). The tilt of each doublet was measured five times and averaged. The average tilt of the five doublets was 0.17° with a standard deviation of 0.07°.
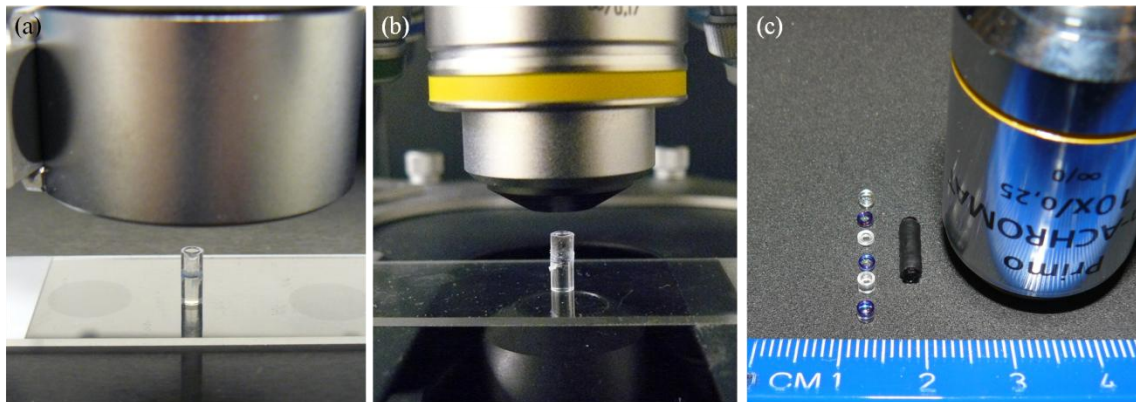
Figure 6.5. (a) Sample doublet undergoing tilt measurements with a Zygo white light interferometer. (b)Sample doublet undergoing decenter measurements with a Zeiss microscope. (c) Set of lenses ready for assembly and fully assembled achromatic objective, next to a commercial objective and ruler for scale.

To measure the decenter, each doublet was placed on a microscope slide beneath an Imager.Z1 upright microscope (Carl Zeiss) (Figure 6.5(b)). Images of the first and last surfaces were captured without adjusting the lateral position of the stage or the doublet itself. This process was repeated four more times, moving the doublet between pairs of images. The decenter between each doublet was measured in ImageJ by find the center of each surface and calculating the displacement between pairs.

The average decenter for the set of doublets was 9.6 μm with a standard deviation of 9.0 μm. When compared to the toleranced values for tilt and decenter, 0.2° and 15 μm (Table 6.2), the measured values indicate that some, though likely not all, of the objectives built will have diffraction-limited performance. These values will also allow further optical designs to be more accurately toleranced.

6.3.2. SI-HRME with integrated achromatic, ultra-slim objective

A complete set of individual lenses and an assembled achromatic objective are shown in Figure 6.5(c). The exterior has been painted black with permanent marker to prevent external light from entering the system. A layer of heat shrink tubing has been added to improve the objective's durability. To reduce stray light through the system, baffles were added within the objective by applying permanent marker up to the edges of the optical surfaces (the blue surfaces in Figure 6.5(c)). An integrated achromatic objective is shown in Figure 6.6(a). The fully assembled SI-HRME is shown in Figure 6.6(b) and matches the schematic in Figure 6.1.
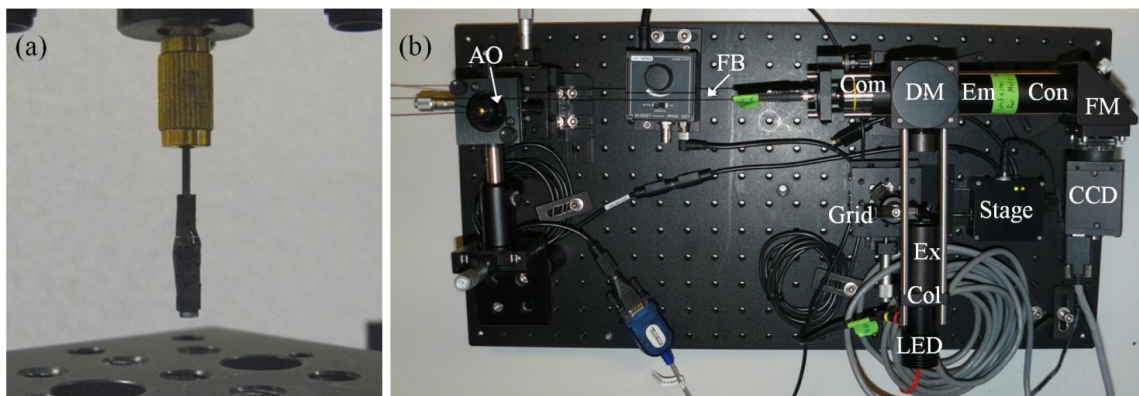
Figure 6.6. (a) Achromatic objective integrated to a fiber bundle. (b) Assembled SI-HRME. Col – collection lens; Ex – excitation filter; DM – dichroic mirror; Com – commercial objective, FB – fiber bundle; AO – achromatic objective; Em – emission filter; Con – condenser lens; FM – folding mirror.

6.4. Results

6.4.1. Achromatic, ultra-slim objective performance

The performance of the achromatic objective was characterized before incorporating it into the optical biopsy system. Images from the custom objective were relayed through an Imager.Z1 upright microscope (Carl Zeiss) as shown in Figure 6.7(a). A fluorescent 1951 USAF resolution target (38-256, Edmund Optics Inc.) was placed at the object plane of the custom objective while in water immersion and an image of the target was relayed with a 10X NA0.45 objective (Carl Zeiss). An example image showing good performance is displayed in Figure 6.7(b). There is some loss of resolution at the edge of the FOV; this is because the objective is designed for imaging a curved object and the target is flat. Adjusting the focal plane by a few microns brings the edge features into sharp focus.
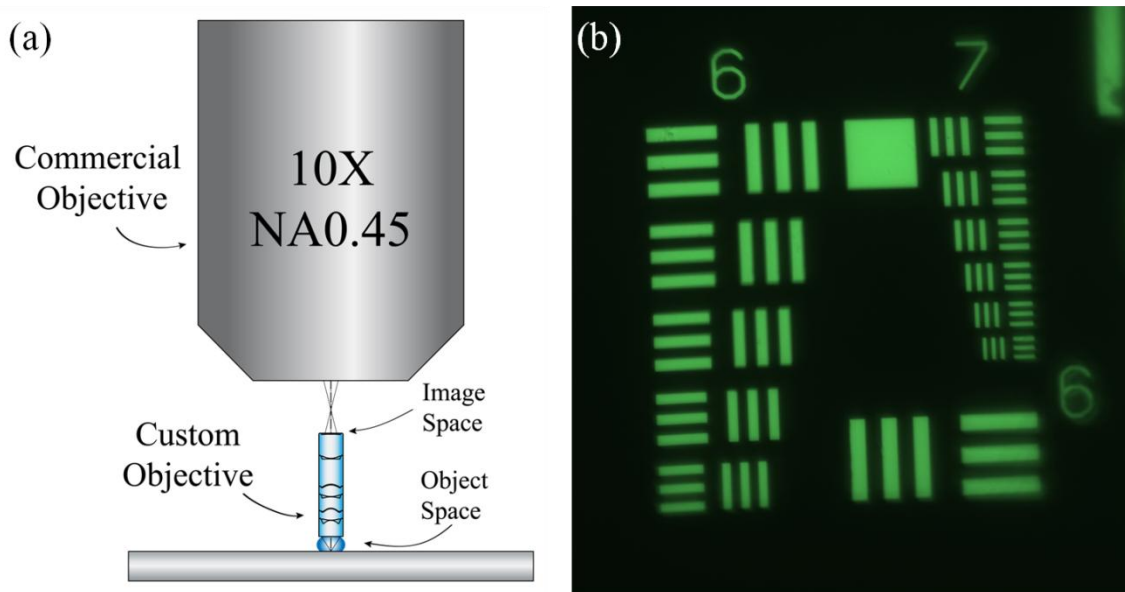
Figure 6.7. (a) Microscope objective relaying images from the custom achromatic objective. (b) Fluorescence image of a resolution target imaged through the achromatic objective.

To ensure that the achromatic, ultra-slim objective is in fact achromatized, the objective's chromatic focal shift was measured. A liquid crystal tunable filter generated narrowband light, starting at 450 nm. A resolution target was brought into focus and the objective's position was measured. This procedure was performed in 20 nm steps up to 630 nm, then repeated four times. The average chromatic focal shift is plotted below, along with the nominal chromatic focal shift (Figure 6.8). The measurements demonstrate that the objective is achromatic, though the chromatic focal shift range of 6.9 μm is slightly larger than the 6.0 μm diffraction-limited shift range. This analysis was compared to the a different custom, ultra-slim NA0.55 plastic objective that conforms to the specifications in Table 6.1 except that it is designed for only a single wavelength. Because the monochromatic objective has the same NA and magnification as the achromatic objective, the diffraction-limited shift range is also the same. The nominal chromatic focal shift for

the monochromatic objective is 96.7 µm, more than an order of magnitude greater than the diffraction-limited shift range. The excitation and emission peaks of proflavine are marked on the measured achromatic objective plot (X) and on the nominal monochromatic objective plot (+). Note that the peaks are within the diffraction-limited range for the achromatic objective and are well outside this range for the monochromatic objective.

Chromatic Focal Shifts
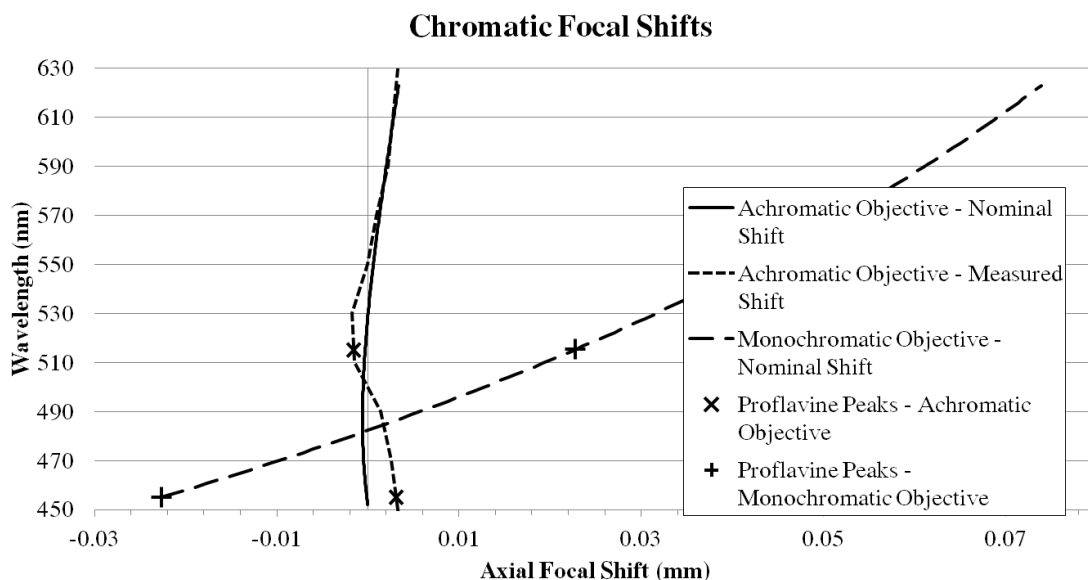
Figure 6.8. Chromatic focal shifts of an achromatic, ultra-slim objective and a monochromatic, ultra-slim objective.

Breast carcinoma cells from the 435S cell line were imaged with the achromatic objective as shown in Figure 6.7(a), as well as an NA0.65 objective (Carl Zeiss). The cells were seeded on a microscope slide and stained with a 0.05% proflavine solution for 5 minutes before washing with 1X PBS (Sigma-Aldrich Co.). Images of the cells are shown in Figure 6.9. The achromatic objective was able to successfully image the *in vitro* cells and resolve subcellular features including nuclei

and membranes. The quality of images from the commercial objective and the custom objective are comparable, despite the commercial objective having a higher NA than the custom objective.
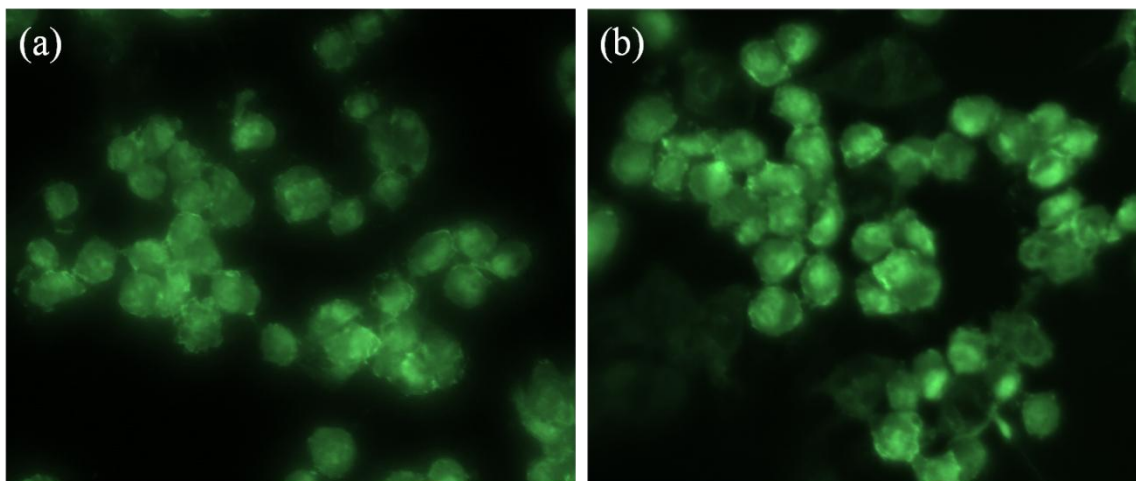
Figure 6.9. Breast carcinoma cells from the 435S cell line stained with proflavine imaged with (a) an NA0.65 objective and (b) the achromatic objective.

The lateral resolution limit of the endomicroscope was measured before and after integrating the achromatic objective (Figure 6.10). With only a bare fiber bundle, the smallest resolvable features on a resolution target are group 7, element 1 (Figure 6.10(a)), indicating a resolution limit of 7.8 μm. With the achromatic objective at the distal tip, all features on the target are resolvable (Figure 6.10(b)), indicating a resolution of at least 4.4 μm, which nearly matches the expected 4.0 μm resolution limit.
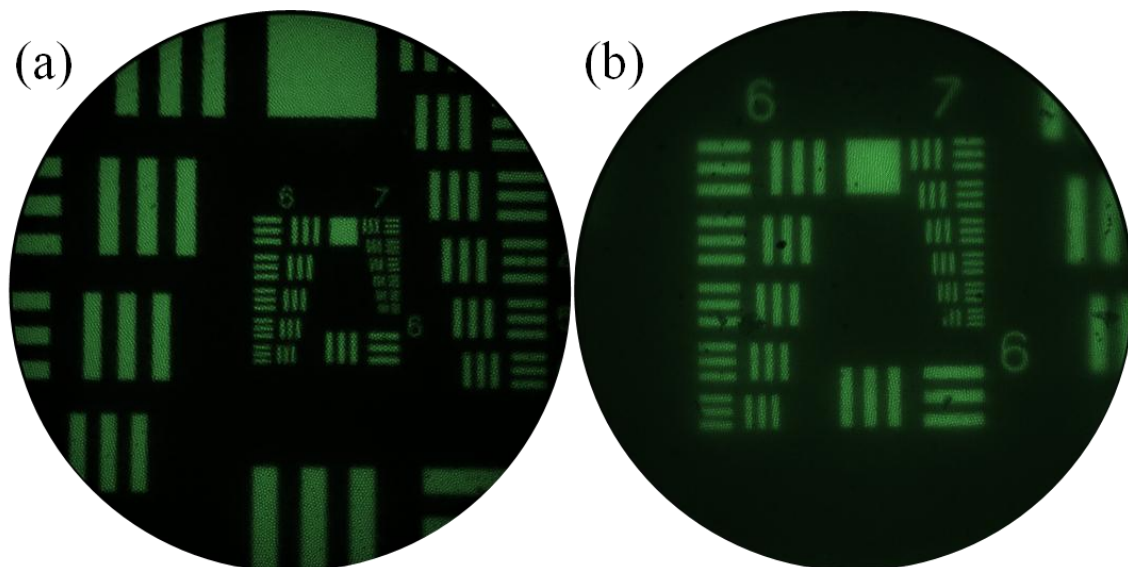
Figure 6.10. Fluorescence images of a 1951 USAF resolution target through the HRME (a) before integrating the achromatic objective to the distal tip of the fiber bundle and (b) after integrating the objective. The lateral resolution limit improves from 7.8 µm (group 7, element 1) to 4.4 µm (group 7, element 6).

6.4.2. Integrated SI-HRME performance

Optical sectioning was achieved via structured illumination through the optical biopsy system. Fluorescent lens paper was imaged both without and with structured illumination (Figure 6.11(a) and Figure 6.11(b)) as described in Section 5.2. When structured illumination is applied, the contrast is increased by reducing out of focus light. Also, individual fibers of the lens paper are easier to resolve with optical sectioning.
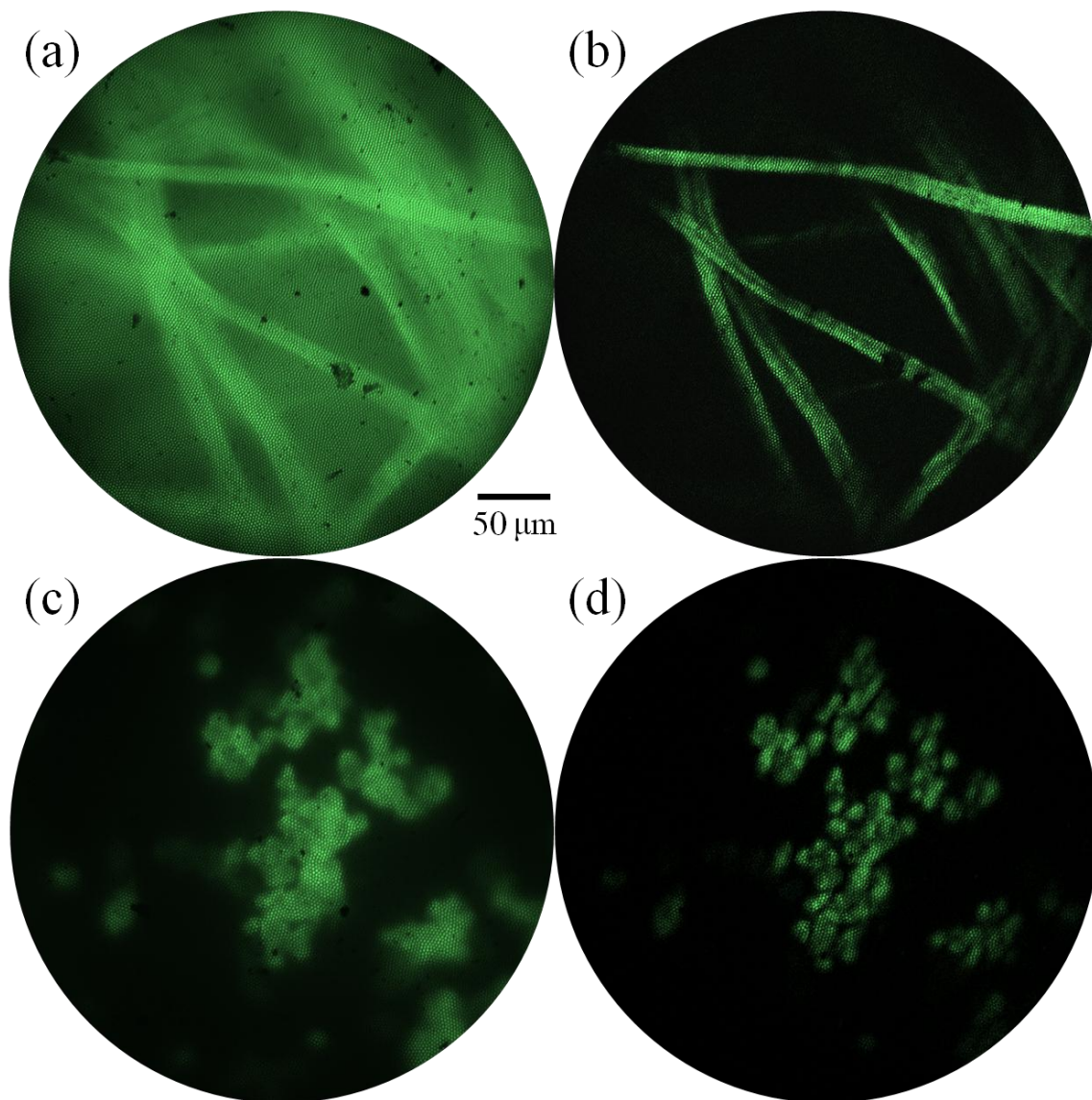
Figure 6.11. Images through the optical biopsy system. Fluorescent lens paper imaged (a) without and (b) with structured illumination. Breast carcinoma cells from the 435S cell line imaged (c) without and (d) with structured illumination.

Breast carcinoma cells prepared as described above were also imaged both without and with structured illumination (Figure 6.11(c) and Figure 6.11(d)). The optical biopsy system was able to successfully image the sample via optical sectioning through a custom achromatic, ultra-slim objective. In this case, there was only a moderate increase in contrast due to the cells already being a monolayer.

The optical biopsy system was evaluated using *ex vivo* mouse tissue. Samples from a normal mouse mammary gland and from a tumor were sliced, stained with proflavine as described in Section 5.3.1, and imaged with the integrated SI-HRME and with the Vivascope 2500 confocal microscope. Selected sites were matched and the results are shown in Figure 6.12. Note that there is greater contrast improvement for the tumor images, which are dense with nuclei, than for the relatively sparse normal tissue images.

6.5. Discussion

An optical biopsy system which uses structured illumination to achieve optical sectioning and which integrates a custom achromatic, ultra-slim objective was demonstrated. The achromatized NA0.55 objective has the same OD as a biopsy needle and magnifies the sample onto the fiber bundle, improving resolution. Structured illumination reduces out of focus light and improves the contrast of thick samples. The system was successfully demonstrated on a range of samples, including *ex vivo* breast tissue stained with proflavine. The SI-HRME can provide the basis to improve optical biopsies and may reduce the number of conventional biopsies performed in the future.

While the lenses with built in alignment features are the same OD as a core biopsy needle, adding the heat shrink to the achromatic objective for additional structural support causes the objective to be too wide. In the future, the optomechanical design can be modified to fit within a 14-gage (2.1 mm) hypodermic

needle, which has an inner diameter of 1.96 mm. This would improve the strength of

the integrated optical biopsy system and allow the probe to pierce tissue.
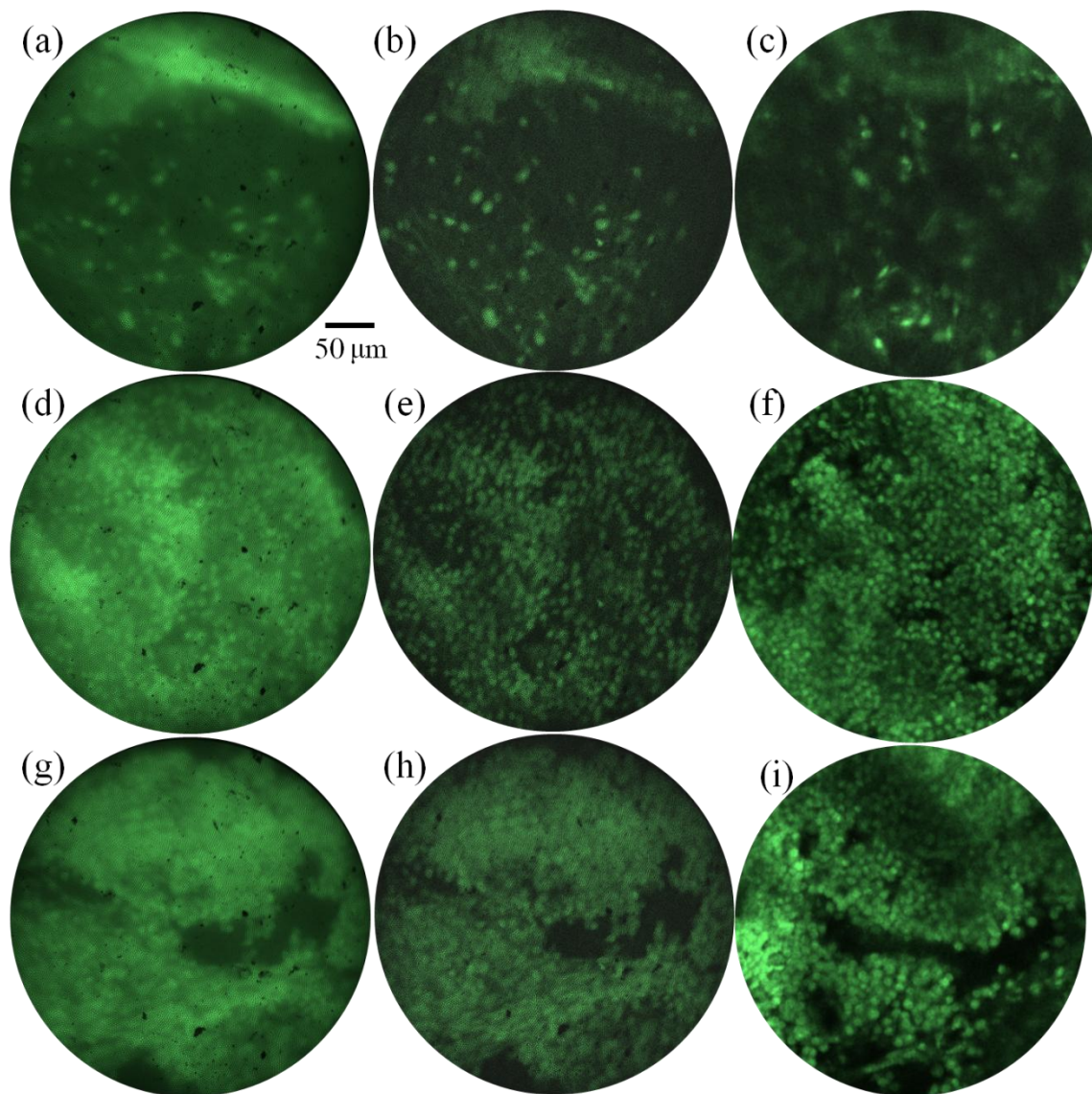
Figure 6.12. *Ex vivo* mouse tissue images through the optical biopsy system and a benchtop confocal microscope. Images (a-c) are from a normal mammary gland and images (d-i) are from a tumor. Images (a,d,g) are without structured illumination, images (b,e,h) are with structured illumination, and images (c,f,i) are via the confocal microscope. Confocal images courtesy of Jessica Dobbs.

6.6. Acknowledgements

<div align="right">

Chapter 7

</div>

<div align="right">

Conclusions

</div>

In summary, this thesis presented an optical biopsy system which utilizes structured illumination and an achromatic ultra-slim objective. The work described the development of endomicroscope objectives which utilize plastic lenses and their incorporation into an endomicroscope with optical section capabilities to help improve the diagnosis of breast cancer.

The ability of plastic lenses assembled with zero alignment techniques to form high performance optical systems was demonstrated. The lenses have high transmission rates, low autofluorescence, and are able to be formed into aspheres as easily as spheres, allowing simpler optical designs. Using either metal springs formed via DXRLE or alignment features cut directly into the plastic lenses, high fabrication tolerances can be maintained and allowed the creation of objectives which maintain diffraction-limited performance.

An NA0.4 ultra-slim objective was built and implemented for non-linear imaging. The system successfully imaged biological samples via second harmonic generation and two-photon fluorescence. However, this objective was monochromatic and could perform well for only one wavelength at a time. To improve the functionality of the miniature objectives, an achromatic design was tested in a prototype system. The achromatic objective successfully imaged two fluorophores (proflavine and cresyl violet) as they simultaneously stained breast carcinoma cells, which the monochromatic objective was unable to do. Once an all-plastic, achromatic objective was verified, a new, higher NA objective was designed, built, and tested.

In parallel, an endomicroscope capable of performing structured illumination was demonstrated. The SI-HRME system was able to improve the contrast of images of *ex vivo* breast resections compared to the conventional HRME. After this improvement, a custom, high NA achromatic objective was attached to the distal tip of the SI-HRME's fiber bundle, improving the lateral resolution of the system and allowing images which are one step closer to the gold standard.

In the future, the achromatic objective should be modified to fit within a 14-gage hypodermic needle (the OD needs to be reduced by at least an additional 150 μm), matching the size of a core biopsy needle. Further studies should be performed to confirm the SI-HRME's ability to diagnose cancer. Other system improvements should include a second excitation and emission pathway by using an additional LED, a new dichroic mirror, and new excitation and emission filters; this can allow

multiple dyes to be imaged simultaneously and permit digital staining to be performed. The optical biopsy system is a step forward for *in vivo* microscopy.

References

1. National Cancer Institute, "Breast Cancer Risk in American Women," http://www.cancer.gov/cancertopics/factsheet/detection/probability-breast-cancer.
2. A. Bombonati and D. C. Sgroi, "The molecular pathology of breast cancer progression," J. Pathol. **223**, 307–317 (2011).
3. K. Polyak, "Is breast tumor progression really linear?," Clin. Cancer Res. **14**, 339–341 (2008).
4. M. H. Torosian, "Clinical Classifications of Breast Cancer," in *Breast Cancer: A Guide to Detection and Multidisciplinary Therapy*, M. H. Torosian, ed., 1st ed. (Humana Press, 2002).
5. Roger Herdman and Larry Norton, Editors, Committee on New Approaches to Early Detection and Diagnosis of Breast Cancer, *Saving Women's Lives: Strategies for Improving Breast Cancer Detection and Diagnosis -- A Breast Cancer Research Foundation and Institute of Medicine Symposium* (The National Academies Press, 2005).
6. *Mammography and Beyond: Developing Technologies for the Early Detection of Breast Cancer* (n.d.).
7. M. H. Torosian, L. A. Newman, and F. C. Ames, eds., "Breast Biopsy Techniques," in *Breast Cancer: A Guide to Detection and Multidisciplinary Therapy*, 1st ed. (Humana Press, 2002).
8. M. Silverstein, "Where's the outrage?," J. Am. Coll. Surg. **208**, 78–79 (2009).
9. Y. Cui, E. A. Koop, P. J. van Diest, R. A. Kandel, and T. E. Rohan, "Nuclear morphometric features in benign breast tissue and risk of subsequent breast cancer," Breast Cancer Res. Treat. **104**, 103–107 (2007).
10. L. Mariuzzi, A. Mombello, G. Granchelli, V. Rucco, E. Tarocco, D. Frank, J. Davis, D. Thompson, H. Bartels, G. M. Mariuzzi, and P. H. Bartels, "Quantitative study of breast cancer progression: different pathways for various in situ cancers," Mod. Pathol. **15**, 18–25 (2002).
11. C. Kretschmer, A. Sterner-Kock, F. Siedentopf, W. Schoenegg, P. M. Schlag, and W. Kemmner, "Identification of early molecular markers for breast cancer," Mol. Cancer **10**, 15 (2011).
12. J. Bini, J. Spain, K. Nehal, V. Hazelwood, C. DiMarzio, and M. Rajadhyaksha, "Confocal mosaicing microscopy of human skin ex vivo: spectral analysis for digital staining to simulate histology-like appearance," J. Biomed. Opt. **16**, 076008 (2011).
13. D. S. Gareau, "Feasibility of digitally stained multimodal confocal mosaics to simulate histopathology," J. Biomed. Opt. **14**, 034050 (2009).
14. W. Göbel, D. Brucker, Y. Kienast, A. Johansson, G. Kniebühler, A. Rühm, S. Eigenbrod, S. Fischer, M. Goetz, F.-W. Kreth, A. Ehrhardt, H. Stepp, K.-M. Irion,

and J. Herms, "Optical needle endoscope for safe and precise stereotactically guided biopsy sampling in neurosurgery," Opt. Express **20**, 26117–26126 (2012).

15. W. A. Berg, I. N. Weinberg, D. Narayanan, M. E. Lobrano, E. Ross, L. Amodei, L. Tafra, L. P. Adler, J. Uddo, W. Stein 3rd, and E. A. Levine, "High-resolution fluorodeoxyglucose positron emission tomography with compression ("positron emission mammography") is highly accurate in depicting primary breast cancer," Breast J. **12**, 309–323 (2006).

16. W. Maï, C. T. Badea, C. T. Wheeler, L. W. Hedlund, and G. A. Johnson, "Effects of breathing and cardiac motion on spatial resolution in the microscopic imaging of rodents," Magn. Reson. Med. **53**, 858–865 (2005).

17. M. Koutalonis, H. Delis, G. Spyrou, L. Costaridou, G. Tzanakos, and G. Panayiotakis, "Monte Carlo studies on the influence of focal spot size and intensity distribution on spatial resolution in magnification mammography," Phys. Med. Biol. **53**, 1369–1384 (2008).

18. R. S. Jaiswal, J. Singh, and G. P. Adams, "High-resolution ultrasound biomicroscopy for monitoring ovarian structures in mice," Reprod. Biol. Endocrinol. **7**, 69 (2009).

19. B. W. Pogue, S. C. Davis, X. Song, B. A. Brooksby, H. Dehghani, and K. D. Paulsen, "Image analysis methods for diffuse optical tomography," J. Biomed. Opt. **11**, 33001 (2006).

20. T. J. Muldoon, M. C. Pierce, D. L. Nida, M. D. Williams, A. Gillenwater, and R. Richards-Kortum, "Subcellular-resolution molecular imaging within living tissue by fiber microendoscopy," Opt. Express **15**, 16413–16423 (2007).

21. K. J. Rosbach, D. Shin, T. J. Muldoon, M. A. Quraishi, L. P. Middleton, K. K. Hunt, F. Meric-Bernstam, T.-K. Yu, R. R. Richards-Kortum, and W. Yang, "High-resolution fiber optic microscopy with fluorescent contrast enhancement for the identification of axillary lymph node metastases in breast cancer: a pilot study," Biomed. Opt. Express **1**, 911–922 (2010).

22. W. M. White, M. Rajadhyaksha, S. González, R. L. Fabian, and R. R. Anderson, "Noninvasive imaging of human oral mucosa in vivo by confocal reflectance microscopy," Laryngoscope **109**, 1709–1717 (1999).

23. B. A. Flusberg, E. D. Cocker, W. Piyawattanametha, J. C. Jung, E. L. M. Cheung, and M. J. Schnitzer, "Fiber-optic fluorescence imaging," Nat. Methods **2**, 941–950 (2005).

24. L. Fu, A. Jain, C. Cranfield, H. Xie, and M. Gu, "Three-dimensional nonlinear optical endoscopy," J. Biomed. Opt. **12**, 040501 (2007).

25. W. Göbel, J. N. D. Kerr, A. Nimmerjahn, and F. Helmchen, "Miniaturized two-photon microscope based on a flexible coherent fiberbundle and a gradient-index lens objective," Opt. Lett. **29**, 2521–2523 (2004).

26. N. Bozinovic, C. Ventalon, T. Ford, and J. Mertz, "Fluorescence endomicroscopy with structured illumination," Opt. Express **16**, 8016–8025 (2008).

27. A. R. Tumlinson, B. Povazay, L. P. Hariri, J. McNally, A. Unterhuber, B. Hermann, H. Sattmann, W. Drexler, and J. K. Barton, "In vivo ultrahigh-

resolution optical coherence tomography of mouse colon with an achromatized endoscope," J. Biomed. Opt. **11**, 064003 (2006).

28. A. G. Podoleanu, "Optical coherence tomography," Br. J. Radiol. **78**, 976–988 (2005).
29. A. Mazhar, D. J. Cuccia, S. Gioux, A. J. Durkin, J. V. Frangioni, and B. J. Tromberg, "Structured illumination enhances resolution and contrast in thick tissue fluorescence imaging," J. Biomed. Opt. **15**, 010506 (2010).
30. A. Weigel, D. Schild, and A. Zeug, "Resolution in the ApoTome and the confocal laser scanning microscope: comparison," J. Biomed. Opt. **14**, 014022 (2009).
31. E. A. M. O'Flynn, A. R. M. Wilson, and M. J. Michell, "Image-guided breast biopsy: state-of-the-art," Clin. Radiol. **65**, 259–270 (2010).
32. D. Kambiz, "Breast Cancer Research: Offers a comprehensive examination of current practice in breast cancer treatment," http://www.breastresearch.com/sentinelneedle.html.
33. "Ultrasound-Guided Breast Biopsy," http://www.radiologyinfo.org/en/info.cfm?pg=breastbius.
34. A. L. Polglase, W. J. McLaren, S. A. Skinner, R. Kiesslich, M. F. Neurath, and P. M. Delaney, "A fluorescence confocal endomicroscope for in vivo microscopy of the upper- and the lower-GI tract," Gastrointest. Endosc. **62**, 686–695 (2005).
35. A. R. Rouse, A. Kano, J. A. Udovich, S. M. Kroto, and A. F. Gmitro, "Design and Demonstration of a Miniature Catheter for a Confocal Microendoscope," Appl. Opt. **43**, 5763–5771 (2004).
36. K. Dunbar and M. Canto, "Confocal endomicroscopy," Curr. Opin. Gastroen. **24**, 631–637 (2008).
37. D. C. Leiner and R. Prescott, "Correction of chromatic aberrations in GRIN endoscopes," Appl. Opt. **22**, 383–386 (1983).
38. J. C. Jung and M. J. Schnitzer, "Multiphoton endoscopy," Opt. Lett. **28**, 902–904 (2003).
39. P. Kim, M. Puoris'haag, D. Côté, C. P. Lin, and S. H. Yun, "In vivo confocal and multiphoton microendoscopy," J. Biomed. Opt. **13**, 010501 (2008).
40. M. T. Myaing, D. J. MacDonald, and X. Li, "Fiber-optic scanning two-photon fluorescence endoscope," Opt. Lett. **31**, 1076–1078 (2006).
41. T. H. Chia and M. J. Levene, "Microprisms for In Vivo Multilayer Cortical Imaging," J. Neurophysiol. **102**, 1310–1314 (2009).
42. GRINTECH, "GRIN Lens Systems for Medical Applications," http://www.grintech.de/grin-lens-systems-for-medical-applications.html.
43. Y. Zhao, H. Nakamura, and R. J. Gordon, "Development of a versatile two-photon endoscope for biological imaging," Biomed. Opt. Express **1**, 1159–1172 (2010).
44. Y. Wu and X. Li, "Combined influences of chromatic aberration and scattering in depth-resolved two-photon fluorescence endospectroscopy," Biomed. Opt. Express **1**, 1234–1243 (2010).

45. T. J. Muldoon, S. Anandasabapathy, D. Maru, and R. Richards-Kortum, "High-resolution imaging in Barrett's esophagus: a novel, low-cost endoscopic microscope," Gastrointest. Endosc. **68**, 737–744 (2008).

46. T. J. Muldoon, N. Thekkek, D. Roblyer, D. Maru, N. Harpaz, J. Potack, S. Anandasabapathy, and R. Richards-Kortum, "Evaluation of quantitative image analysis criteria for the high-resolution microendoscopic detection of neoplasia in Barrett's esophagus," J. Biomed. Opt. **15**, 026027 (2010).

47. S. M. Landau, C. Liang, R. T. Kester, T. S. Tkaczyk, and M. R. Descour, "Design and evaluation of an ultra-slim objective for in-vivo deep optical biopsy," Opt. Express **18**, 4758–4775 (2010).

48. T. Tot and L. Tabár, "The role of radiological-pathological correlation in diagnosing early breast cancer: the pathologist's perspective," Virchows Arch. **458**, 125–131 (2011).

49. R. T. Kester, T. Christenson, R. R. Kortum, and T. S. Tkaczyk, "Low cost, high performance, self-aligning miniature optical systems," Appl. Opt. **48**, 3375–3384 (2009).

50. M. D. Chidley, K. D. Carlson, R. R. Richards-Kortum, and M. R. Descour, "Design, assembly, and optical bench testing of a high-numerical-aperture miniature injection-molded objective for fiber-optic confocal reflectance microscopy," Appl. Opt. **45**, 2545–2554 (2006).

51. K. B. Sung, C. Liang, M. Descour, T. Collier, M. Follen, and R. Richards-Kortum, "Fiber-optic confocal reflectance microscope with miniature objective for in vivo imaging of human tissues," IEEE Trans. Biomed. Eng. **49**, 1168–1172 (2002).

52. E. Laemmel, M. Genet, G. Le Goualher, A. Perchant, J.-F. Le Gargasson, and E. Vicaut, "Fibered confocal fluorescence microscopy (Cell-viZio) facilitates extended imaging in the field of microcirculation. A comparison with intravital microscopy," J. Vasc. Res. **41**, 400–411 (2004).

53. A. Osdoit, M. Genet, A. Perchant, S. Loiseau, B. Abrat, and F. Lacombe, "In vivo fibered confocal reflectance imaging: totally non-invasive morphological cellular imaging brought to the endoscopist," in *Proc. SPIE 6082*, G. J. Tearney and T. D. Wang, eds. (2006), pp. 608208–608208–10.

54. D. Wang, B. V. Hunter, M. J. Cobb, and X. Li, "Super-Achromatic Rapid Scanning Microendoscope for Ultrahigh-Resolution OCT Imaging," IEEE J. Sel. Top. Quant. Electron. **13**, 1596–1601 (2007).

55. G. C. Birch, M. R. Descour, and T. S. Tkaczyk, "Hyperspectral Shack?Hartmann test," Appl. Opt. **49**, 5399–5406 (2010).

56. G. I. Greisukh, E. G. Ezhov, I. A. Levin, and S. A. Stepanov, "Design of achromatic and apochromatic plastic micro-objectives," Appl. Opt. **49**, 4379–4384 (2010).

57. M. A. A. Neil, R. Juskaitis, and T. Wilson, "Method of obtaining optical sectioning by using structured light in a conventional microscope," Opt. Lett. **22**, 1905–1907 (1997).

58. D. Karadaglić and T. Wilson, "Image formation in structured illumination wide-field fluorescence microscopy," Micron **39**, 808–818 (2008).

59. T. Tkaczyk, M. Rahman, V. Mack, K. Sokolov, J. Rogers, R. Richards-Kortum, and M. Descour, "High resolution, molecular-specific, reflectance imaging in optically dense tissue phantoms with structured-illumination," Opt. Express **12**, 3745–3758 (2004).

60. C. H. Wong, N. G. Chen, and C. J. R. Sheppard, "Study on potential of structured illumination microscopy utilizing digital micromirror device for endoscopy purpose," in *International Symposium on Biophotonics, Nanophotonics and Metamaterials, 2006. Metamaterials 2006* (2006), pp. 218 –221.

61. D. Karadaglić, R. Juskaitis, and T. Wilson, "Confocal endoscopy via structured illumination," Scanning **24**, 301–304 (2002).

62. S. Mukherjee, J. S. Wysock, C. K. Ng, M. Akhtar, S. Perner, M.-M. Lee, M. A. Rubin, F. R. Maxfield, W. W. Webb, and D. S. Scherr, "Human bladder cancer diagnosis using Multiphoton microscopy," in *Proceedings - Society of Photo-Optical Instrumentation Engineers* (2009), Vol. 7161.

63. M. Göppert-Mayer, "Über Elementarakte mit zwei Quantensprüngen," Annalen der Physik **401**, 273–294 (1931).

64. W. Denk, J. H. Strickler, and W. W. Webb, "Two-photon laser scanning fluorescence microscopy," Science **248**, 73–76 (1990).

65. P. C. Cheng and C. K. Sun, "Nonlinear (Harmonic Generation) Optical Microscopy," in *Handbook Of Biological Confocal Microscopy*, J. B. Pawley, ed. (Springer US, 2006), pp. 703–721.

66. L. Gao, L. Jin, P. Xue, J. Xu, Y. Wang, H. Ma, and D. Chen, "Reconstruction of complementary images in second harmonic generation microscopy," Opt. Express **14**, 4727–4735 (2006).

67. R. M. Williams, W. R. Zipfel, and W. W. Webb, "Multiphoton microscopy in biological research," Curr Opin Chem Biol **5**, 603–608 (2001).

68. F. Helmchen, M. S. Fee, D. W. Tank, and W. Denk, "A miniature head-mounted two-photon microscope. high-resolution brain imaging in freely moving animals," Neuron. **31**, 903–912 (2001).

69. D. Bird and M. Gu, "Two-photon fluorescence endoscopy with a micro-optic scanning head," Opt. Lett. **28**, 1552–1554 (2003).

70. L. Fu, A. Jain, H. Xie, C. Cranfield, and M. Gu, "Nonlinear optical endoscopy based on a double-clad photonic crystal fiber and a MEMS mirror," Opt. Express **14**, 1027–1032 (2006).

71. R. Le Harzic, M. Weinigel, I. Riemann, K. König, and B. Messerschmidt, "Nonlinear optical endoscope based on a compact two axes piezo scanner and a miniature objective lens," Opt. Express **16**, 20588–20596 (2008).

72. K. König, A. Ehlers, I. Riemann, S. Schenkl, R. Bückle, and M. Kaatz, "Clinical two-photon microendoscopy," Microsc. Res. Tech. **70**, 398–402 (2007).

73. S. Schenkl, A. Ehlers, R. L. Harzic, M. Stark, I. Riemann, B. Messerschmidt, M. Kaatz, and K. König, "Rigid and high NA multiphoton fluorescence GRIN-endoscopes," in *Novel Optical Instrumentation for Biomedical Applications III*, C. Depeursinge, ed., Proceedings of SPIE-OSA Biomedical Optics (Optical Society of America, 2007), Vol. 6631, p. 6631_28.

74. J. N. Rogart, J. Nagata, C. S. Loeser, R. D. Roorda, H. Aslanian, M. E. Robert, W. R. Zipfel, and M. H. Nathanson, "Multiphoton imaging can be used for microscopic examination of intact human gastrointestinal mucosa ex vivo," Clin. Gastroenterol. Hepatol. **6**, 95–101 (2008).

75. C. J. Engelbrecht, R. S. Johnston, E. J. Seibel, and F. Helmchen, "Ultra-compact fiber-optic two-photon microscope for functional fluorescence imaging in vivo," Opt. Express **16**, 5556–5564 (2008).

76. P. Singh, A. Chak, J. E. Willis, A. Rollins, and M. V. Sivak Jr, "In vivo optical coherence tomography imaging of the pancreatic and biliary ductal system," Gastrointest. Endosc. **62**, 970–974 (2005).

77. X. Li and W. Yu, "Deep Tissue Microscopic Imaging of the Kidney with a Gradient-Index Lens System," Opt. Commun. **281**, 1833–1840 (2008).

78. M. Mansuripur, *Classical Optics and Its Applications*, 2nd ed. (Cambridge University Press, 2009).

79. B. McCall, M. Pierce, E. A. Graviss, R. Richards-Kortum, and T. Tkaczyk, "Toward a low-cost compact array microscopy platform for detection of tuberculosis," Tuberc. **91 Suppl 1**, S54–60 (2011).

80. R. T. Kester, T. S. Tkaczyk, M. R. Descour, T. Christenson, and R. Richards-Kortum, "High numerical aperture microendoscope objective for a fiber confocal reflectance microscope," Opt. Express **15**, 2409–2420 (2007).

81. S. Bäumer, *Handbook of Plastic Optics* (John Wiley & Sons, 2011).

82. O. S. O. America, *Handbook of Optics, Vol. 2: Devices, Measurements, and Properties, Second Edition*, 2nd ed. (McGraw-Hill Professional, 1994).

83. M. B. Wabuyele, S. M. Ford, W. Stryjewski, J. Barrow, and S. A. Soper, "Single molecule detection of double-stranded DNA in poly(methylmethacrylate) and polycarbonate microfluidic devices," Electrophoresis **22**, 3939–3948 (2001).

84. Y. Konishi, T. Sawaguchi, K. Kubomura, and K. Minami, "High Performance Cyclo Olefin Polymer ZEONEX," in *Proc. SPIE 5872*, T. D. Goodman, ed. (2005), pp. 587203–587203–8.

85. K. Obuchi, M. Komatsu, and K. Minami, "High performance optical materials cyclo olefin polymer ZEONEX," in *Proc. SPIE 6671*, J. H. Burge, O. W. Faehnle, and R. Williamson, eds. (2007), p. 66711I–66711I–9.

86. M. D. Ries, E. Young, L. Al-Marashi, P. Goldstein, A. Hetherington, T. Petrie, and L. Pruitt, "In vivo behavior of acrylic bone cement in total hip arthroplasty," Biomaterials **27**, 256–261 (2006).

87. M. Petrtyl, Z. Bastl, Z. Krulis, H. Hulejova, M. Polanska, J. Lisal, J. Danesova, and P. Cerny, "Cycloolefin-Copolymer/Polyethylene (COC/PE) Blend Assists with the Creation of New Articular Cartilage," Macromolecular Symposia **294**, 120–132 (2010).

88. V. Tangpasuthadol, S. M. Pendharkar, R. C. Peterson, and J. Kohn, "Hydrolytic degradation of tyrosine-derived polycarbonates, a class of new biomaterials. Part II: 3-yr study of polymeric devices," Biomaterials **21**, 2379–2387 (2000).

89. L. Tabet, C. Bussy, A. Setyan, A. Simon-Deckers, M. J. Rossi, J. Boczkowski, and S. Lanone, "Coating carbon nanotubes with a polystyrene-based polymer protects against pulmonary toxicity," Part Fibre Toxicol **8**, 3 (2011).

90. J. C. Diels and W. R. Pro, *Ultrashort Laser Pulse Phenomena: Fundamentals, Techniques, and Applications on a Femtosecond Time Scale* (Acad. Press, 2006).

91. R. F. Shi, C. Koeppen, G. Jiang, J. Wang, and A. F. Garito, "Origin of high bandwidth performance of graded-index plastic optical fibers," Appl. Phys. Lett. **71**, 3625 –3627 (1997).

92. S. N. Kasarova, N. G. Sultanova, C. D. Ivanov, and I. D. Nikolov, "Analysis of the dispersion of optical plastic materials," Opt. Mater. **29**, 1481–1490 (2007).

93. W. R. Zipfel, R. M. Williams, and W. W. Webb, "Nonlinear magic: multiphoton microscopy in the biosciences," Nat. Biotechnol. **21**, 1369–1377 (2003).

94. K. Sokolov, J. Aaron, B. Hsu, D. Nida, A. Gillenwater, M. Follen, C. MacAulay, K. Adler-Storthz, B. Korgel, M. Descour, R. Pasqualini, W. Arap, W. Lam, and R. Richards-Kortum, "Optical systems for in vivo molecular imaging of cancer," Technol. Cancer Res. Treat. **2**, 491–504 (2003).

95. A. P. Tzannes and J. M. Mooney, "Measurement of the modulation transfer function of infrared cameras," Opt. Eng. **34**, 1808–1817 (1995).

96. ISO 12233:2000, "Photography -- Electronic still-picture cameras -- Resolution measurements," http://www.iso.org/iso/home/store/catalogue_tc/catalogue_detail.htm?csnumber=33715.

97. J. Jung, H. Park, J. Park, and H. Kim, "Accuracy of preoperative ultrasound and ultrasound-guided fine needle aspiration cytology for axillary staging in breast cancer," ANZ J. Surg. **80**, 271–275 (2010).

98. S. Taneja, A. Jena, K. Kumar, and A. Mehta, "Technical Note: MRI-guided breast biopsy - our preliminary experience," Indian J. Radiol. Imaging **20**, 218–220 (2010).

99. J. E. Kalinyak, K. Schilling, W. A. Berg, D. Narayanan, J. P. Mayberry, R. Rai, E. B. Dupree, D. K. Shusterman, M. A. Gittleman, W. Luo, and C. G. Matthews, "PET-guided breast biopsy," Breast J. **17**, 143–151 (2011).

100. Y. Wu, J. Xi, M. J. Cobb, and X. Li, "Scanning fiber-optic nonlinear endomicroscopy with miniature aspherical compound lens and multimode fiber collector," Opt. Lett. **34**, 953–955 (2009).

101. M. Kyrish, U. Utzinger, M. R. Descour, B. K. Baggett, and T. S. Tkaczyk, "Ultra-slim plastic endomicroscope objective for non-linear microscopy," Opt. Express **19**, 7603 (2011).

102. T. S. Tkaczyk, J. D. Rogers, M. Rahman, T. C. Christenson, S. Gaalema, E. L. Dereniak, R. Richards-Kortum, and M. R. Descour, "Multi-modal miniature microscope: 4M Device for bio-imaging applications - an overview of the system," in *Proc. SPIE 5959* (2005), p. 59590N–59590N.

103. M. C. Pierce, R. A. Schwarz, V. S. Bhattar, S. Mondrik, M. D. Williams, J. J. Lee, R. Richards-Kortum, and A. M. Gillenwater, "Accuracy of in vivo multimodal

optical imaging for detection of oral neoplasia," Cancer Prev. Res. **5**, 801–809 (2012).

104. M. H. Lee, K. Buterbaugh, R. Richards-Kortum, and S. Anandasabapathy, "Advanced endoscopic imaging for Barrett's Esophagus: current options and future directions," Curr. Gastroenterol. Rep. **14**, 216–225 (2012).

105. M. C. Pierce, Y. Guan, M. K. Quinn, X. Zhang, W.-H. Zhang, Y.-L. Qiao, P. Castle, and R. Richards-Kortum, "A pilot study of low-cost, high-resolution microendoscopy as a tool for identifying women with cervical precancer," Cancer Prev. Res. **5**, 1273–1279 (2012).

106. M. Kyrish and T. S. Tkaczyk, "Achromatized endomicroscope objective for optical biopsy," Biomed. Opt. Express **4**, 287 (2013).